CHALMERS
UNIVERSITY OF TECHNOLOGY

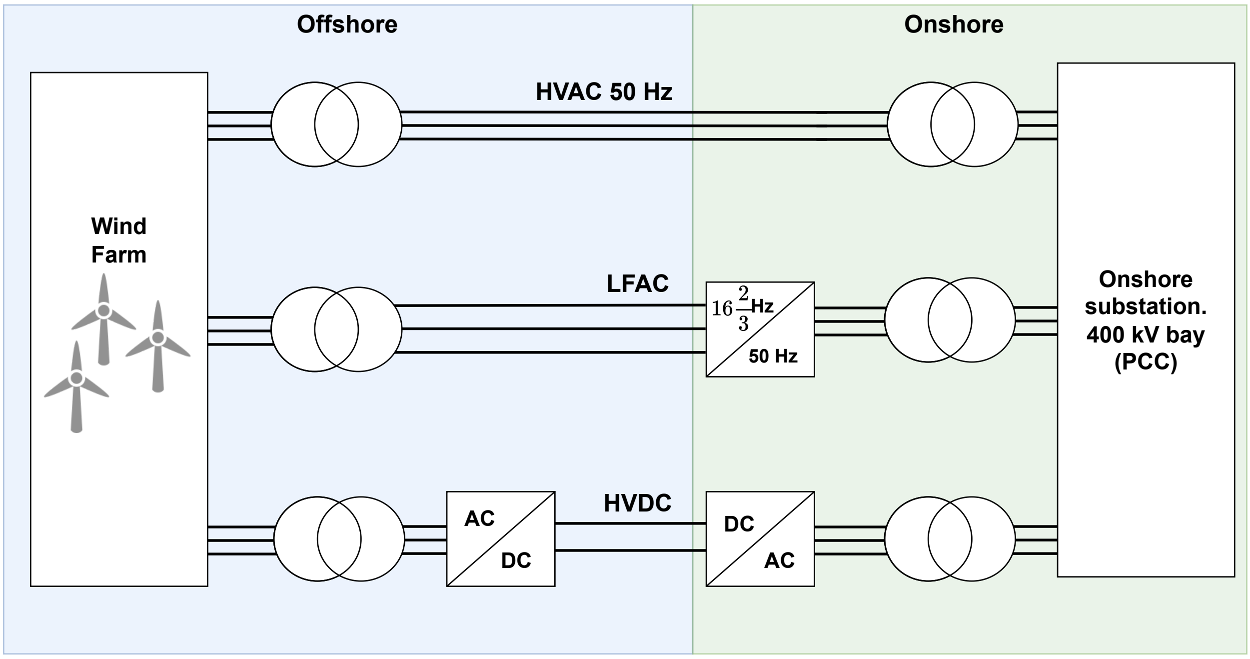

Offshore Wind Transmission Systems - Power Grid Integration

Techno-economic analysis of HVAC, HVDC, and LFAC

Master's thesis in Sustainable Electric Power Engineering and Electromobility

Albin Andersson & Olle Johansson

DEPARTMENT OF ELECTRICAL ENGINEERING

CHALMERS UNIVERSITY OF TECHNOLOGY
Gothenburg, Sweden 2024
www.chalmers.se

MASTER'S THESIS 2024

Offshore Wind Transmission Systems - Power Grid Integration

Techno-economic analysis of HVAC, HVDC, and LFAC

Albin Andersson
Olle Johansson

CHALMERS
UNIVERSITY OF TECHNOLOGY

Department of Electrical Engineering
Division of Electric Power Engineering
Chalmers University of Technology
Gothenburg, Sweden 2024

Offshore Wind Transmission Systems - Power Grid Integration
Techno-economic analysis of HVAC, HVDC, and LFAC
Albin Andersson & Olle Johansson

Supervisor: Tarik Dervišić, Hitachi Energy Power Consulting Sweden
Examiner: Massimo Bongiorno, Department of Electrical Engineering

Master's thesis report 2024
Department of Electrical Engineering
Chalmers University of Technology
SE-412 96 Gothenburg
Sweden
Telephone +46 31 772 1000

Cover: An overview of the studied transmission system topologies

Typeset in LaTeX
Gothenburg, Sweden 2024

Offshore Wind Transmission Systems - Power Grid Integration
Techno-economic analysis of HVAC, HVDC, and LFAC
Albin Andersson & Olle Johansson
Department of Electrical Engineering
Chalmers University of Technology

Abstract

Offshore wind has turned into one of the most promising sources of renewable energy and the offshore wind industry is a rapidly growing business at this moment in time. This paper compares technical and economic aspects of the export systems associated with transmitting active power by offshore wind farms using High Voltage Alternating current (HVAC), High Voltage Direct Current (HVDC), and Low-Frequency Alternating Current (LFAC).

This study investigated offshore wind farms with installed active power ranging from 300 MW to 1400 MW located 20 km to 200 km from shore. For each configuration, 120 models were dimensioned and implemented in PowerFactory such that load-flow analysis could be performed. Each model in PowerFactory corresponds to a certain power level and distance. The load-flow studies resulted in the ratings of the main equipment for each system, later being used as the input data for the economic evaluation. As the ratings of the components were set, Capital Expenditures (CAPEX) and Levelized Cost of Electricity (LCOE) analysis were performed to evaluate the techno-economic distance for each configuration.

The Key Performace Indicator (KPI) LCOE concluded that HVAC was the suitable topology for distances from 0 km up to 140 - 160 km. A steady decline in break-even distance can be found as the active power increases. HVAC cables became the driving force of the CAPEX and Operational Expenditures (OPEX) the further away from shore the wind farm is located. HVDC required a large initial investment for the platform and converters, but considerably cheaper cables make it suitable for long-distance transmission. The break-even distance for HVDC was found at roughly 150 km. Furthermore, the optimal techno-economic range for LFAC was confined to low-power, long-distance applications. Its break-even point was found at distances over 160 km, and an installed active power ranging from 300 - 500 MW. Lastly, a sensitivity analysis was performed at the cost of the SFC (Static Frequency Converter). If the cost was reduced, the break-even point between LFAC and HVAC would remain the same while it would gain some distance from the HVDC case. As the cost was increased, the business case for LFAC according to the LCOE analysis vanished.

Keywords: Offshore Wind, Transmission System, Export System, HVAC, HVDC, LFAC, Power Grid Integration, LCOE, SFC, STATCOM

Acknowledgements

We want to thank everyone at Hitachi Energy Power Consulting Sweden who has helped us during the Master thesis. A special thanks to our supervisor Tarik Dervišić for your help with the PowerFactory simulations and everything we have learnt from you. We also want to thank our examiner Massimo Bongiorno for insightful discussions regarding offshore wind integration.

Albin Andersson & Olle Johansson, Gothenburg, 2024

List of Acronyms

Below is the list of acronyms that have been used throughout this thesis listed in alphabetical order:

AEP	Annual Electricity Produced
BNetzA	Bundesnetzagentur
BtB	Back-to-Back
CAPEX	Capital Expenditures
CSC	Current Source Converter
DFIG	Doubly Fed Induction Generator
E-STATCOM	Enhanced Static Synchronous Compensator
ENTSO-E	European Network of Transmission System Operators
FC-TCR	Fixed Capacitor - Thyristor-controlled reactor
FEPA	Federation of European Producers of Abrasives
FSR	Fixed Shunt Reactor
GTO	Gate Turn-off Tyristor
HVAC	High Voltage Alternating Current
HVDC	High Voltage Direct Current
IGBT	Insulated Gate Bipolar Transistor
KPI	Key Performance Indicator
LCC	Line Commutated Converter
LCOE	Levelized Cost of Electricity
LFAC	Low Frequency Alternating Current
M^3C	Modular Multilevel Matrix Converter
MMC	Modular Multilevel Converter
MVDC	Medium Voltage Direct Current
NPV	Net Present Value
OLTC	On Load Tap Changer
OnSS	Onshore Substation
OPEX	Operational Expenditures
OSS	Offshore Substation
PCC	Point of Common Coupling
PMSG	Permanent Magnet Synchronous Generator

p.u.	Per Unit
PWM	Pulse Width Modulation
SFC	Static Frequency Converter
STATCOM	Static Synchronous Compensator
SR	Shunt Reactor
SVC	Static VAR Compensator
SvK	Svenska Kraftnät
TCR	Thyristor Controlled Reactor
TCSC	Thyristor Controlled Series Compensation
TSC	Thyristor Switched Capacitor
TSO	Transmission System Operator
UN	United Nations
VSC	Voltage Source Converter
WTG	Wind Turbine Generator

Contents

List of Figures

List of Tables

1

Introduction

Electricity plays a vital role in a well-functioning society. Almost everything in today's society ranging from homes to industries, and hospitals requires electricity to function and the importance of having access to electricity cannot be understated. As the world becomes increasingly more interconnected and more reliant on digital technologies, the electricity demand will continue to increase. In 2022, the total global consumption of electricity was 25 530 TWh, an increase of roughly 2% compared to the previous year. Historically, the annual increased use of electricity has been 2.8% which indicates that the supply of electricity has to increase to meet the increasing demand [1].

Wind power is an old technology that has been used to aid farmers for centuries, but at the end of the 19^{th} century Charles Brush implemented the first wind turbine that produced electricity in Ohio, United States. The innovation continued and in Denmark, Pour La Cour managed to build over 100 wind turbines generating $20 - 35$ kW each. Post World War II, experiments were carried out throughout the world that proved that wind power had a potential for large-scale production [2].

During the oil crisis with its shortages of oil in the 1970s, and also later on the anti-nuclear movements, sparked an interest in alternative ways to generate power to reduce the dependency on oil for countries all over the world. As environmental awareness increased, countries such as Denmark sought to replace or at least diversify their means of power generation. One way was to replace conventional power plants powered by fossil-based fuels such as oil, coal, and gas to reduce their carbon footprint but also to diversify their portfolio by integrating renewable sources such as wind power. As these conventional power plants are phased out, new types of generation have to replace the conventional ones which is a challenging task in itself, especially with the required increase of supplied electricity [3].

Wind farms then started to form and by 2016 the onshore capacity worldwide had reached 494 GW. As larger and larger onshore wind farms were built in combination with the increased resistance among residents partly against the visual impacts, suitable space for these sites started to vanish [4]. The open sea also provides higher and more even wind speeds causing less fatigue on the wind turbines. In addition, since the installations are offshore, height restrictions are less of a problem leading to even higher wind speeds [5]. Hence the focus was shifted to the ocean and its potential of housing offshore wind farms. However, the development of offshore wind started earlier. The first offshore wind farm, Vindeby in Denmark, was commissioned in 1991. The wind farm consisted of 11 turbines with a combined capacity of roughly 5 MW [6]. The expansion early on was slow, by the end of 2009 there was only 2000 MW of installed capacity offshore. The commissioning increased rapidly in the 2010s. By 2022 close to 60 GW of capacity was installed offshore, which is an increase of 30 times in the last 13 years. There was also 12.4 GW under construction with the largest wind farm yet being built in the Netherlands with a capacity of 1.5 GW [7]. Such large wind farms utilize the big leap in technology when it comes to wind turbines. The most powerful one installed by 2023 is installed offshore in China with a capacity of 16 MW. The company Mingyang also unveiled an offshore wind turbine capable of producing 22 MW expected to be commissioned in 2025 [8].

The first transmission technology used to connect offshore wind farms was High Voltage Alternating Current (HVAC) with a transmission frequency of 50 or 60 Hz depending on the location. The major benefit of using HVAC was its simple integration into the rest of the power grid since HVAC is the most common technology used to transmit power onshore. Especially since the wind turbines in this configuration generate power at 50/60 Hz at tens of kilovolts. Hence, HVAC is often the technology of choice for shorter transmission distances as it is a non-complex and relatively cheap solution. To connect the offshore wind farms by HVAC, each wind turbine is commonly connected to the switchgear housed on an offshore platform. The voltage is then transformed up at the offshore platform where the subsea transmission cable then transmits the power back to shore where it is connected to the power grid. However, HVAC has a major drawback. HVAC utilizes alternating current in which reactive currents will be generated due to the high capacitance of the subsea cable. As the cable has a certain current rating, a consequence is that less active power can be transferred the more reactive current that is carried. Thus, as the transmission distance increases HVAC becomes a costly solution due to all the compensation needed to counteract the reactive power [9].

To combat the problems related to longer transmission distances using HVAC, a new technology was proposed, namely Voltage Source Converter High Voltage Direct Current (VSC-HVDC). The major benefit of VSC-HVDC is that it utilizes direct current. Since there is no frequency component of the transmission current, there will be no reactive current produced by the capacitance of the subsea cable. Hence the transmissible distance of VSC-HVDC becomes technically unlimited. Another benefit of VSC-HVDC is that the converter stations have independent control of voltage and current. The converter station onshore can therefore provide grid support to the power grid by controlling the active and reactive power injected by shifting the complex quantities. For VSC-HVDC an offshore platform is needed since the wind turbines still generate power at AC. Hence, there must be a converter station placed on an offshore platform that converts AC into DC so that the power then can be transmitted with DC back onto shore where another converter station converts the DC back into AC. These converter stations are complex and expensive, which results in VSC-HVDC often being too costly at short to medium distances [9].

Lastly, a third technology has been proposed to integrate offshore wind power, Low-

Frequency Alternating Current (LFAC). Historically, LFAC transmission systems are commonly seen in power systems for the railway due to the distances, as the frequency is directly proportional to the charging capacitance of the cable. Therefore, a lower frequency will minimize the effects of the charging capacitance which effectively reduces the electrical distance. The result is that the reactive current flowing through the conductor can be greatly reduced depending on the chosen transmission frequency. If there is less reactive current passing through the cable, it allows for more active current to pass through the cable which results in an increased active power transfer capacity. Since there still is an alternating current, transformers can still be used which greatly reduces the complexity of the system. As for the LFAC system, the wind turbines can provide power at the lower frequencies, thus removing the need of a converter at the offshore platform. However, since the voltage from the wind turbines currently is lower than the transmission voltage, there must be a step-up transformer located at the offshore platform that transforms the voltage to the transmission voltage of the subsea cable. When the power reaches shore, the frequency is lower compared to the rest of the power system. Therefore a Static Frequency Converter (SFC) is needed to convert the frequency back to the land-based transmission system frequency which typically is 50 or 60 Hz [10].

1.1 Aim

The aim is to investigate three different transmission technologies for offshore wind to find the optimal techno-economical range at certain distances and power levels. The configurations to be studied are HVAC, HVDC, and LFAC for offshore wind farms. The study aims to initially evaluate techno-economic aspects by steady-state analysis such that a reliable system can be suggested that meets the relevant grid code requirements. Then economic key performance indicators will be introduced to finalize the techno-economical analysis. The final aim, by using standardized models and the key performance indicators, is to find the suitable topology for a given distance and power level.

1.2 Scope

The configurations will be modeled downstream from the Point of Common Coupling (PCC). The PCC is the first meshed point of the onshore grid, and the voltage is assumed to be 400 kV at a substation located close to the shoreline. The reactive power exchange at the PCC is regulated by a Static Synchronous Compensator (STATCOM) for HVAC, an SFC for LFAC, and an onshore converter for HVDC. At the PCC, the reactive power exchange for all cases is controlled to unity power factor, which is the only grid code considered. The SFC is assumed to have sufficient reactive capabilities to comply with the grid code requirement. The wind farm will be modeled as an equivalent generator and Inter-Array Cables (IACs) will not be considered.

Load-flow analysis will be performed for the three different configurations, no dynamic studies will be considered. To be allowed to connect to the Swedish Transmission System Operators (TSO), Svenska Kraftnät (SvK), 400 kV grid, a minimum installed capacity of 300 MW is required. There is also an upper limit of 1400 MW per bay in the substation since that is the dimensioning fault in the Nordic synchronized grid [11]. Hence, it was chosen that the power levels to be studied are between $300 - 1400MW$. The alter the power levels, the installed active power of an equivalent generator was changed. Regarding the distances, the distances are to be varied from 0 to 200 km in steps of 20 km.

The wind turbines are assumed to operate at a nominal voltage of 66 kV. For HVAC, typical transmission frequencies are either 50 or 60 Hz. In this study, the transmission frequency is assumed to be 50 Hz. Regarding LFAC, the transmission frequency of the subsea cable is assumed to be $16\frac{2}{3}$ Hz. Therefore the wind turbines are also assumed to be generating at $16\frac{2}{3}$ Hz for the LFAC case and 50 Hz for HVAC/HVDC. The HVDC configuration will be constructed as a symmetrical monopole and is assumed to operate at a nominal voltage of ±320 kV for an active power greater than 500 MW, and ±150 kV for an active power less than 500 MW. Regarding HVAC, for power levels less than or equal to 800 MW, the voltage is 220 kV. For power levels greater than 800 MW, 275 kV is used. The LFAC systems operate at the same transmission voltages as for HVAC.

Levelized Cost of Electricity (LCOE) and Net Present Value (NPV) will be utilized to evaluate which configuration is suitable given an installed active power capacity and a distance. Capital Expenditures (CAPEX) and Operational Expenditures (OPEX) associated with each export system will be gathered from the literature review. These costs will be merged to include everything relevant to the export system, hence costs associated with the wind turbines and inter-array cables will not be included in the economic evaluation.

1.3 Specification of the issue being investigated

- What are the major differences between the three topologies in order to meet the relevant grid code requirements?
- How does the break-even point between the three topologies change with respect to power level and distance?
- Are there any useful cases where LFAC could be used instead of HVAC or HVDC and vice versa?

1.4 Ethics and sustainability

Electric power engineers play a crucial role when it comes to developing electrical systems and technologies that directly impact society, hence several ethical and societal aspects need to be considered. This chapter will discuss the impacts that offshore wind farm has on society with three different aspects in mind: societal, ethical, and ecological.

1.4.1 Societal impact

United Nations (UN) formed 17 sustainable development goals in 2015 to pursue by 2030 with the intent of increasing the living standard and reducing the effect that climate change has on Earth. One of the goals (goal 7) is to "Ensure access to affordable, reliable, sustainable and modern energy for all", an ambitious goal that requires less dependency on conventional power plants such as coal and gas [12]. Increasing the number of offshore wind facilities certainly contributes when it comes to achieving this specific goal, it is the cheapest energy source per produced kWh and carbon-neutral once construction has finished. More offshore wind facilities will reduce the cost of electricity for residents and industries without increasing the effects of climate change, so certainly an important topic from a societal perspective.

Offshore wind facilities have risen in popularity lately due to their effectiveness in supplying carbon-neutral electricity. However, the potential visual impacts of offshore wind facilities have emerged as a major concern among residents of society. Small offshore wind facilities (25-48 turbines) localized close to land such as at distances less than 16 km have a large impact on the visual aspects of coastlines. Large offshore wind facilities (greater than 100 turbines) can easily be visible up to distances of 35 km. Once reaching distances above 50 km large wind farms can only be seen after looking at it closely for an extended time resulting in a low assessment of potential visual impact [13].

1.4.2 Ethical impact

Construction of offshore wind facilities is a challenging task especially as wind farms are being constructed further from shore in tougher weather and sea conditions. The offshore industry opposes significantly higher health and safety challenges compared to onshore wind, namely due to injury risks related to remote worksites. Understanding the safety challenges is important for the offshore industry to ensure further sustainable growth without significant risks of accidents to occur. Legislation of detailed risk assessment before construction and maintenance is important from an ethical point of view such that construction can take place without any major risks of harming the workforce or the environment [14].

1.4.3 Ecological impact

Data provided by the Federation of European Producers of Abrasives (FEPA) suggests that the natural dynamics and features of the seabed are largely unaffected by the development of offshore wind farms. However, disturbances are unavoidable during the construction phase which leads to increased turbidity from suspended sediment particles. Siltation within the concrete base benefits the settlements of polychaetes, leading to soft sediment communities surrounding the turbines. Creations of soft sediment communities are perceived as positive, where studies suggest that it leads to increased complexity of the habitat which increases the species richness and biomass [15]. However, exposure to turbidity for a long period during construction can negatively impact certain marine mammals that lay their egg on the seabed such as Atlantic wolffish or Batoidea. High sediment particle exposure of 10 mg/l will quickly cover the eggs, reducing the mammal's ability to reproduce [16]. Increased noise levels underwater are apparent for offshore wind farms and studies show that fish can suffer from permanent hearing loss that impacts their behavior resulting in increased stress levels. As of today, there are no regulations in place when it comes to noise levels once wind farm construction has finished. However, regulations are in place regarding piling the seabed, where underwater acoustics levels have to be below 204 dB re 1µPa for adult fishes [17].

Bird species are affected in numerous ways by wind farms once construction has finished. They are namely impacted in two different ways: collisions occurring with either the rotating blades or the supporting tower, and further traveling distances for especially migratory birds. How many collisions occur is highly dependent on where the wind farm is constructed, where an avoidance rate of 98% is commonly used when estimating the number of collisions that occur with the windmill. For the Poseidon project, it was estimated that roughly 6.3 collisions would occur for Corvidae annually and 13.6 collisions for Common wood pigeons. Offshore wind farms will act as an obstacle for especially migratory birds once construction has finished leading to a further traveling distance for these species. It is estimated that offshore wind farms increase the traveling distance for migratory birds by up to 1 km, sometimes even more [16]. These aspects are important to note and consider when selecting where construction of an offshore wind farm should take place.

2

Methodology

This chapter explains the methodology and in what order the project will be executed to conduct the study.

2.1 Literature review

Firstly, the physical structures and the modeling of offshore wind farms were studied. Especially the different types of generator technologies and their operating voltages such that an accurate equivalent representation of the wind turbines could be modeled in this study. Then, the three export system topologies were studied such that accurate representations could be implemented. Firstly, HVDC was studied. There were a lot of decisions to be made for HVDC regarding cables, converter topologies, and their nominal voltage levels that affected the outcome of the study. Other projects and research papers were studied such that applicable parameters were chosen. For LFAC, the type of converter used for the change of frequency had to be chosen. Therefore available converter types were studied such that an applicable topology was chosen. Since LFAC utilizes a lower transmission frequency than the traditional 50/60 Hz, the impact of operating at a reduced frequency was studied since it affects the choice and dimensioning of components such as cables and transformers. The last studied export system was HVAC. Since HVAC utilizes an alternating current, the effects of charging currents were studied. Since charging currents will be present when alternating current is used, the impact of reactive power compensation became an important topic to maximize the utilization of the export system. Finally, how the export systems are integrated into the grid infrastructure onshore was studied, namely the grid code requirements that must be fulfilled. The previously mentioned literature review was conducted by a review of other research papers, textbooks, and past lectures given by professors at Chalmers University of Technology.

2.2 System modeling

The electrical modeling was performed in a power system analysis tool called PowerFactory. The system was modeled downstream of the PCC, the point onshore where the wind farm is connected to the rest of the power grid. The PCC is the first meshed point of the grid that the offshore wind farm is connected to. Hence the models contained all components from the PCC out to the wind turbines themselves. To ease the simulation, an equivalent model of all generating units, transformers, converters, and reactive power compensators was implemented instead of altering the number of parallel units in between each case regarding the power level. Also, the inter-array cables were not modeled to remove further uncertainties. The initial part of the modeling consisted of parametrization and dimensioning of the components for each case. As the power level and distance were altered, the parameters had to be changed between each simulation case.

2.3 Load-flow analysis

As the models were completed, load-flow analysis was performed for each topology. In the simulations, both the transmission distance and the power level were altered. As the minimum required power input is 300 MW, and the dimensioning fault in the Swedish grid is 1400 MW, 1400 MW must thereby not be exceeded per bay in the substation to ensure stability in the case of a fault [11]. Hence the transmittable power was chosen to be varied from 300 MW up to 1400 MW for each of the three cases. Regarding the simulations, the power level was altered in steps of 100 MW to provide sufficient data enough that accurate interpolation is possible. As for the distances, the distances were varied from 0 to 200 km in steps of 20 km.

2.4 Post processing

As the results of the load-flow analysis performed in PowerFactory resulted in numbers and lists, visualization, and data processing were needed to present understandable and easily comprehensible results. For the post-processing of the data, the software Matlab and Python were used. The output files from PowerFactory were imported into the post-processing software to visualize the results.

2.5 Key performance indicators

Several Key Performance Indicators (KPI) were taken into account when evaluating each configuration's effectiveness from an economic point of view, one of them being the Levelized Cost of Electricity (LCOE). LCOE is defined as the price the generated electricity should be sold at for the system to break even at the end of its lifetime. It considers factors such as investment costs, running costs, lifetime, discount rate, and electricity produced in a year. LCOE is an effective indicator of the cost-effectiveness of the system since calculations can be made without assumptions regarding the uncertainty of future electricity prices. LCOE can determine whether an investment is advantageous or not. If the LCOE is lower than the price at which electricity can be sold, then the investment is disadvantageous. Comparing LCOE prices for each configuration will determine which investment is most advantageous [18].

Another KPI of interest was Net Present Value (NPV). NPV is defined as the capital cost associated with the installation subtracted from the present value of the installation. The present value will be given by annual energy production multiplied by the estimated price of electricity, thus NPV will include the revenue impact of the transmission system which LCOE does not consider. But NPV as a metric is dependent on assumptions associated with electricity price, hence it will be included as a complement to LCOE [19].

3

Literature review and theoretical background

This chapter presents the theory regarding power system components and techniques used to implement offshore wind.

3.1 Power system equations

Most of the world's electric power supply systems are widely interconnected, and these interconnections enable an effective transmission network where power plants can cooperate in supplying diverse loads with electric power. Transmission interconnections enable taking advantage of the availability of generation sources to supply electric power to the loads at minimum cost with the required reliability. Having a non-interconnected grid would require more local generation units to serve the load with the same reliability, hence increasing the electricity cost. Finding the optimum balance between generation and transmission for an interconnected network is a difficult task that requires advanced methods of analysis for system planners, especially as the transmission network grows larger. Evaluating investments such as parallel transmission lines and increased power for generation units is important from a system enhancement perspective. Building parallel transmission lines is useful when it comes to increasing transmission capability, especially in places where the transmission capability is the limiting factor (bottlenecks) [20]. This section will focus on the fundamental equations and transformations used in power system analysis.

3.1.1 Power flow fundamentals

Understanding power flow on a transmission line is essential when it comes to power system analysis. Consider a simple AC transmission system as shown in Figure 3.1a, where locations 1 and 2 could be any substation connected by a transmission line. Substations may have loads, generators, or simply be an interconnecting point of the system. However, in Figure 3.1a the buses are assumed to be stiff buses. E_1 and E_2 are the magnitudes of the bus voltages, δ is the angle difference between the two buses, and the line is assumed to have the inductive impedance X_L for a lossless line. The driving voltage drop in the line is given by the phasor difference E_L between the two voltage phasors E_1 and E_2 as shown in Figure 3.1b.

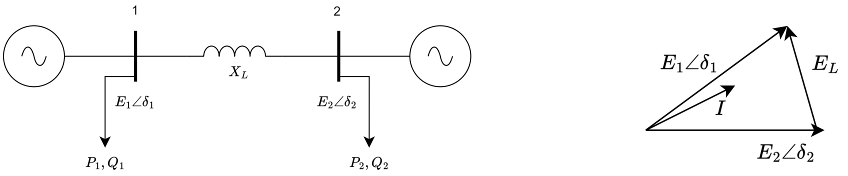

(a) AC power flow two-machine system.

(b) Phasor diagram of bus voltages and line driving voltage.

Figure 3.1: AC power flow for a two-machine system, and its corresponding phasor diagram.

The line current magnitude is given as the voltage drop divided by the impedance, hence the current will lag the driving voltage E_L by 90°. Splitting the current into its active (I_P) and reactive (I_Q) components enables calculations for the active and reactive power. The equations for the apparent, active, and reactive current at point 1 are shown in Equation (3.1).

$$\bar{I} = \frac{\bar{E}_L}{\bar{X}_L} \qquad I_{P_1} = \frac{E_2 \cdot sin(\delta)}{X_L} \qquad I_{Q_1} = \frac{E_1 - E_2 \cdot cos(\delta)}{X_L} \tag{3.1}$$

The active and reactive power at point 1 is then calculated by simply multiplying the bus voltage E_1 with the obtained active and reactive current. Formulas for the active and reactive power at point 1 are shown in Equation (3.2).

$$P_1 = \frac{E_1 \cdot E_2 \cdot sin(\delta)}{X_L} \qquad Q_1 = \frac{E_1(E_1 - E_2 \cdot cos(\delta))}{X_L} \tag{3.2}$$

Equivalent equations can be obtained for point 2 by simply swapping the bus voltages E_1 and E_2 around. Naturally, the equations for the active power will remain the same at both ends but the reactive power will have swapped bus voltages in the numerator. The equations obtained above provide the fundamental points regarding the possibilities of power flow control. Control of the line impedance X_L with for example a thyristor-controlled series capacitor (TCSC) can provide effective control of the current. When the angle is small which often is the case, control of X_L or the angle provides effective control of the active power. For small angles, controlling one or the other line voltage can provide effective control of the reactive power flow through the interconnections [20].

3.2 Power system components, and concepts

This subchapter introduces some of the important components and concepts encountered in offshore wind export systems.

3.2.1 Grid code requirements

Increased installed capacity of wind power will greatly impact the electricity system's steady-state and dynamic properties where previously wind power plants were allowed to be disconnected during system disturbances. However, with increased penetration of wind power, disconnection of wind farms during disturbances can worsen the disturbance and thereby prevent a recovery to normal operation conditions again. Therefore TSOs have implemented certain grid code requirements for wind power plants when it comes to the steady-state and dynamic conditions. Wind power plants must have voltage and frequency regulation under steady-state conditions with the ability to stay connected during voltage dips to provide reactive power to fulfill the recovery requirements of voltage dips to help the system recover back to normal operating conditions [21].

Steady-state grid code requirements regulate the power factor, voltage operating range, frequency operating range, and voltage quality. The steady-state grid code conditions for wind power plants are often specified at the PCC. Reactive power and power factor requirements concern the reactive power capability at the PCC under specified voltage ranges. These requirements differ between countries, some have more demanding requirements than others. For example, Ireland has a power factor requirement of 0.95 lagging to 0.95 leading when the active power output is between $12 - 100\%$ of the installed capacity. This means that the wind power plant is required to have a reactive power capability range of -33% to $+33\%$ of the rated active power. Other countries such as Denmark, have reactive power and voltage requirements that are dependent on the size of the wind farm, while Germany has reactive power requirements that are solely dependent on the voltage at the PCC [21].

3.2.2 Wind turbine generators

Regarding the conversion from mechanical rotating energy into electrical energy, there are currently four alternatives to choose from where one operates at a fixed speed and three at variable speeds. The variable speed variants are beneficial since production at maximum power over larger variations in wind speed is possible.

3.2.2.1 Grid connected induction generators

The directly grid-connected induction generators can be split up into two versions, one with fixed rotor resistance and one with variable rotor resistance. The version with the fixed rotor resistance variant can be found in Figure 3.2. The turbine blades are connected to a shaft that is connected to a gearbox which in turn is connected to an induction generator. Since it utilizes an induction machine, the operational speed of the machine will be close to the frequency of the system it is connected to. The reactive power is commonly compensated by shunt-connected capacitors [21].

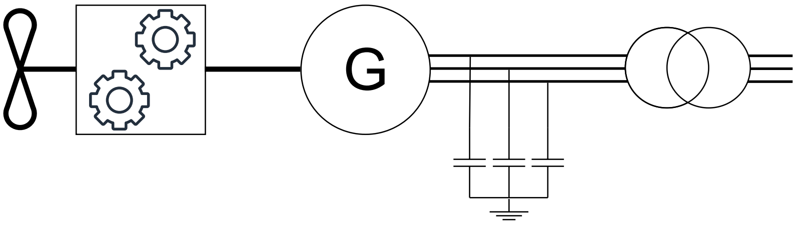

Figure 3.2: Overview of a fixed rotor resistance induction generator.

The next variant is the variable rotor resistance induction generator as seen in Figure 3.3. It is a derivative of the fixed rotor resistance induction generator. The key difference is that the rotor resistance is variable which to some extent enables control of the slip of the induction machine [21].

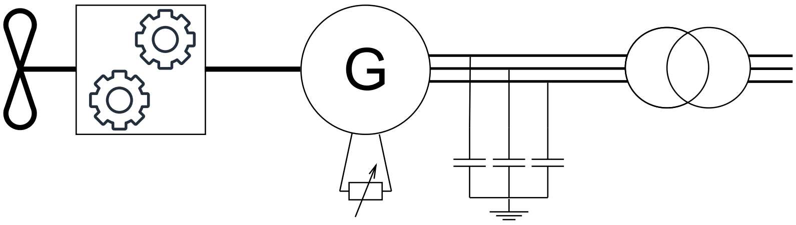

Figure 3.3: Overview of a variable rotor resistance induction generator.

3.2.2.2 Double-fed induction generators

The next topology is the Double-fed Induction Generator (DFIG) as seen in Figure 3.4. As can be seen in the Figure, the stator windings are connected to the grid side, and the rotor windings are connected to the back-to-back VSC converter. The operational principle is that the converter connected to the grid should control the DC-link voltage while the converter connected to the generator controls the apparent power of the generator. An operation point for the desired speed of the machine is set, and if then the slip is negative, the rotor feeds power to the grid. If the slip instead is positive, the generator draws power from the grid. These converters allow for a greater operational area compared to the fixed- and variable rotor resistance but are still to some extent restricted [21].

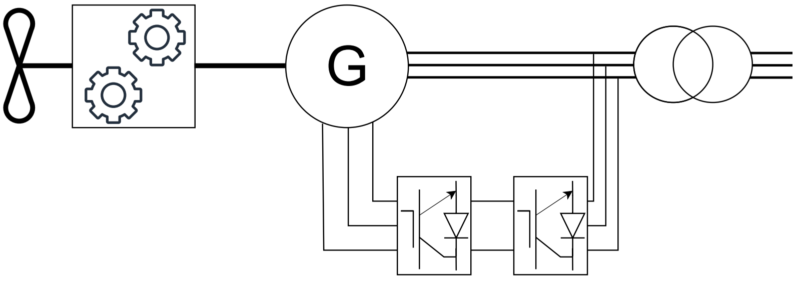

Figure 3.4: Overview of a double-fed induction generator.

3.2.2.3 Full power converter

The last generator topology is the full power converter seen in Figure 3.5. The full power converter can either be equipped with an induction machine or a synchronous machine where a permanent magnet synchronous machine (PMSM) is commonly used due to it being self-excited. For this topology, a VSC back-to-back converter is used to convert power from the generator at its current speed to the frequency of the connected grid, thus allowing for an even larger operational area. The full power converter variant is preferred for offshore applications due to the lower maintenance required compared to the DFIG [21].

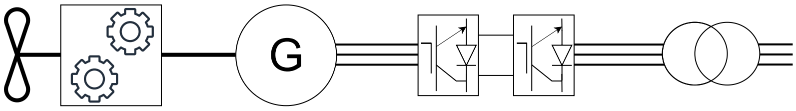

Figure 3.5: Overview of a full power converter.

3.2.2.4 Wind turbines for low-frequency applications

For LFAC applications, two generator technologies are primarily named. The first proposed WTG type is the DFIG. By using a DFIG for low-frequency applications, the size of the gearbox could be reduced since the gear ratio is reduced. If applied to a $16\,\frac{2}{3}$ Hz system, the ratio of the gearbox can be reduced to a third of its nominal size. Since the gearbox is located in the nacelle, the size of the tower could also be reduced due to the lower weight up in the nacelle if the larger transformer is placed at the bottom of the tower. Therefore the LFAC wind turbine with a DFIG could be cheaper compared to a 50 Hz DFIG wind turbine [22]. However, according to [23], the generator size would need to drastically increase which most likely deprives the saved size of the gearbox. Therefore the goal of the LFAC turbines is to minimize the size of the generator. Hence, when it comes to the full power converter, it is suggested that a PMSM would be used since the PMSM is often directly connected to the turbine without a gearbox. It stated that the generator and the converter would take up the same space as for the 50 Hz version, but the converter would need some reconfiguration. The only component that will increase in size for a full power converter solution is therefore the transformer [23].

3.2.3 Offshore platforms

Offshore platforms are used to reduce electrical losses by increasing the voltage before exporting the active power to shore. There are different ways to construct the substructure of an offshore platform. Most substructures deployed to date are jacket structures, which is a submerged steel structure fixed to the seabed by suction anchors. Floating substructures have emerged in recent times, which utilize mooring chains cemented to the seabed to provide stability and buoyancy for the offshore substation. The electrical systems on an offshore platform contain HV switchgear, transformers, converters (if HVDC), passive/active reactive power compensation, earthing systems, and monitoring systems. An offshore platform also contains facilities for accommodation needed for the service and maintenance of the substation. These components namely consist of cranes, helidecks, winches, and control rooms to ease the maintenance process.

The topside of an HVAC platform is typically mounted 25 m above sea level with an area of roughly 800 m^2. An HVAC platform normally weighs between 1200-3000 tonnes and a 1 GW wind farm is likely to have two or three substations. However, an HVDC platform would only have one platform for a 1 GW wind farm to house all the equipment. An HVDC platform also needs to house the converter which an HVAC platform does not need, which increases the weight and cost of the HVDC platform. An HVDC platform normally weighs 12000-18000 tonnes for a 1 GW wind farm [24].

3.2.4 Parameters of installed, or wind farms under construction

In the last two decades, a lot of wind farms have been installed offshore. Since this thesis is conducted from a Swedish point of view data from European offshore wind farms was gathered. Table 3.1 presents some offshore wind projects with their installed capacity, distance onshore and offshore, export system, and the voltage level used. The data is then applied to a scatter plot seen in Figure 3.6 which indicates the relation between installed capacity and distance for the export system used.

Table 3.1: Offshore wind farm projects.

Project	Capacity [MW]	Distance offshore [km]	Distance onshore [km]	Configuration	Voltage level
BorWin1	400	125	75	HVDC	±150
BorWin2	800	125	75	HVDC	±300
Borssele 1 & 2	752	24	0	HVAC	220
DolWin 3	900	75	90	HVDC	±320
Doggerbank A	1200	131	19	HVDC	±320
Doggerbank B	1200	131	19	HVDC	±320
Doggerbank C	1200	196	7	HVDC	±320
East Anglia ONE	714	43	25	HVAC	220
HelWin2	690	85	45	HVDC	±320
Hornsea Project 1	1218	120	40	HVAC	220
Hornsea Project 2	1386	130	39	HVAC	220
Kriegers Flak	605	15	32	HVAC	220
Moray East	950	22	30	HVAC	220
Race Bank	573	32	12	HVAC	220
Seagreen	1075	27	15	HVAC	220
Sofia Offshore wind	1400	220	9	HVDC	±320
Triton Knoll	857	33	52	HVAC	220

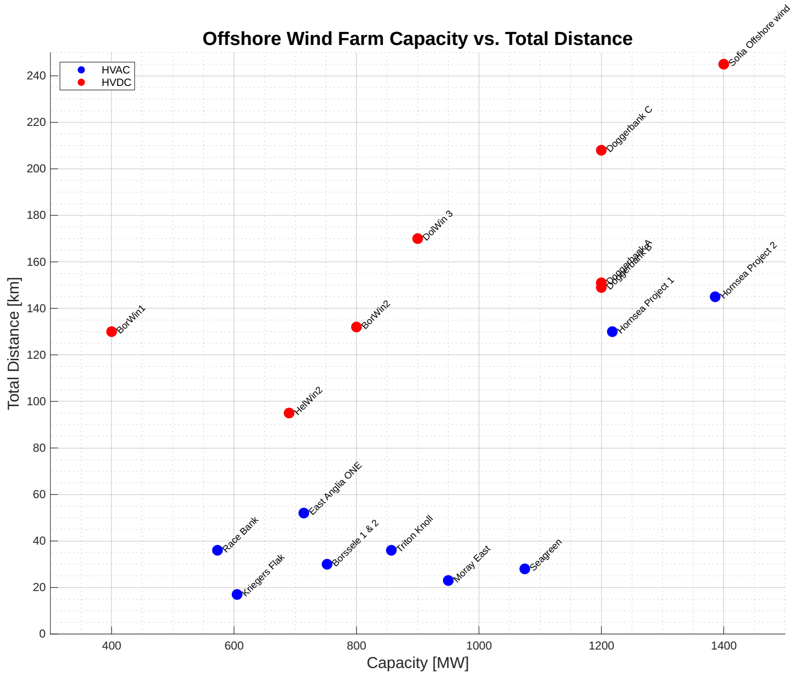

Figure 3.6: A plot presenting the capacity vs. distance for offshore wind projects.

3.3 Transmission system topologies

To bring the power from the offshore wind farm onto the transmission system onshore, there are a few offshore transmission systems that can be chosen. This study researches three options, HVAC, LFAC, and HVDC. The three topologies are presented in this subchapter and an overview of the studied system is found in Figure 3.7.

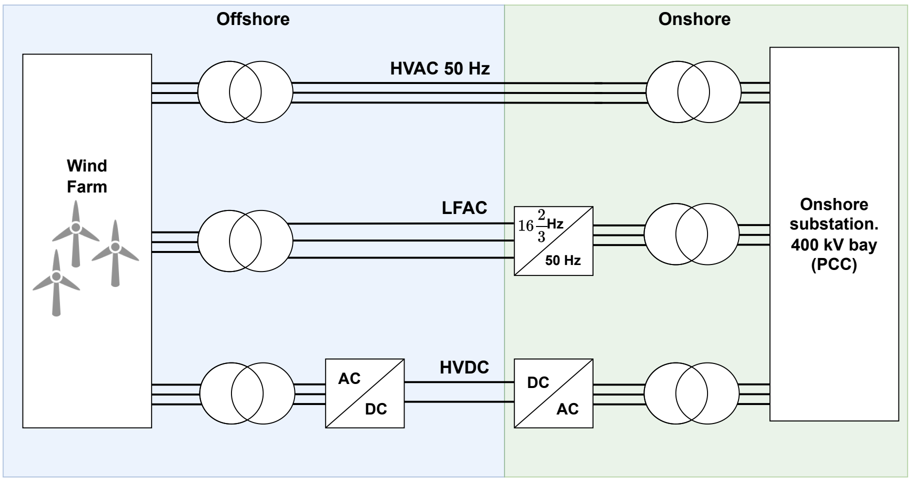

Figure 3.7: An overview of the studied transmission system topologies.

3.3.1 HVAC

In the early 1880s, DC was used to power lights but due to the high losses at low voltages the transmission distances were highly limited. Then two major inventions gave rise to the AC system. Firstly the transformer was invented by William Stanley in 1885, which enabled an easy way to step up the voltage for transmission and thereafter step it down for the end consumers. The second invention that revolutionized the electricity system was the induction machine by Nikola Tesla in 1888 such that the AC voltage could be used to drive the machine. Since then countries all over the world adopted the AC system for the transmission of power due to the ease of transformation and the ease of use with the induction machine for the end consumer. The AC system kept evolving into common transmission voltages between 220 - 750 kV today. Additionally, a system in the Soviet Union managed to commission an 1150 kV system between today's Siberia and Kazakhstan. Today's systems typically consist of a meshed transmission system to transfer the bulk power in or between countries. The voltage is then stepped down into a radially connected sub-transmission grid to transmit power from a connection point at the transmission grid into cities or large industries. The voltage is then stepped down again to the distribution grid where most consumers such as houses and smaller industries are connected. Typically the system is a three-phase system where each phase is shifted 120° from one another. Motors and other three-phase loads can be connected to the three-phase supply. For single-phase loads, the loads are usually spread out evenly between the phases to minimize the unbalance of the system such that the neutral conductor carries as little current as possible [25].

3.3.1.1 Transformers

Transformers are an essential part of the electric grid, and their main purpose is to change voltage levels to enable efficient transmission and distribution of electric energy. The transformer can step up the voltage for long-range transmission and step down the voltage for local distribution, hence minimizing energy losses and ensuring a reliable power supply. It is an effective way of adjusting the voltage level depending on the application without any major losses in the conversion. A transformer accomplishes this change in voltage through a process of electromagnetic induction. When running an alternating current through a conductor, a moving magnetic field is created around the conductor. When a second conductor is placed within the moving magnetic field, the moving flux lines within the magnetic field will induce a current in the second conductor. Electromagnetic induction is used to increase or decrease the voltage between the two conductors. This is achieved by wrapping two conductors into coils around an iron core with different numbers of turns compared to one another. When the coil with more turns is energized, a current will be induced in the coil with fewer turns at a lower voltage than present in the first coil [26].

Understanding how a transformer functions can be explained by looking into how an ideal transformer functions. An ideal transformer is lossless meaning that the windings have no resistance and the magnetic circuit has no reluctance, an illustration of an ideal transformer is shown in Figure 3.8. A transformer normally consists of two windings that are galvanically isolated from each other. The two coils are wound around the same iron core resulting in them being magnetically coupled to each other. The number of turns of the primary and secondary winding are noted N_1 and N_2 in Figure 3.8.

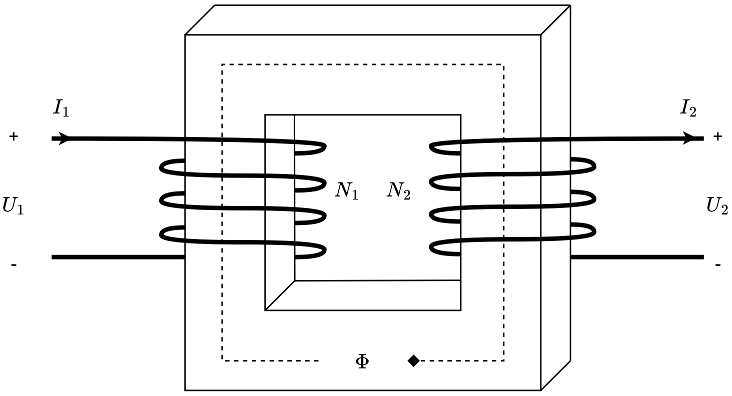

Figure 3.8: Schematic diagram of the ideal iron-core transformer.

Since the windings have no resistance in an ideal transformer it might seem that the current through the windings will be infinite when a voltage is applied. However, the current through the winding will generate a magnetic field and induce a voltage in the winding which counteracts the current. The magnetic field will limit the current from becoming infinite, meaning that the induced voltage from the magnetic field will be of equal magnitude to the applied voltage. The relation between the magnetic flux and the voltage at the primary winding is shown in Equation (3.3a). Since an ideal transformer is lossless (no reluctance or resistance) the magnetic flux generated in the secondary winding will be equal to the flux in the primary winding as shown in Equation (3.3b).

$$U_1 = N_1 \frac{d\Phi}{dt} \tag{3.3a}$$

$$U_2 = N_2 \frac{d\Phi}{dt} \tag{3.3b}$$

Combining Equations (3.3a) and (3.3b) results in Equation (3.4)

$$U_2 = U_1 \frac{N_2}{N_1} \tag{3.4}$$

which showcases the fundamental relation between the voltage on the secondary side as a function of the voltage on the primary side.

The ideal transformer neglects several linear aspects of a real transformer which includes unavoidable losses and inefficiencies. Firstly, the windings in a real transformer have a resistance (R_1) which will lead to joule losses across the windings. Secondly, the magnetic circuit in a real transformer has reluctance meaning that some of the flux will escape out of the core. This leakage flux (Φ_σ) will not contribute to the transformed voltage on the secondary side, generating a need for magnetization current (I_0) to increase the magnetic field. The losses associated with the core consist of hysteresis losses caused by nonlinear magnetic effects in the transformer core and eddy currents caused by joule heating in the core. These losses are modeled as a shunt resistance where R_{Fe} is heating losses associated with the iron core connected in parallel with a magnetization reactance X_m.

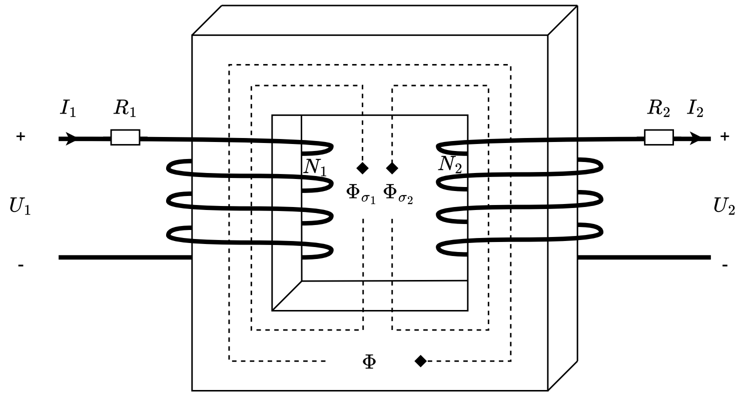

Figure 3.9: Schematic diagram of the iron-core transformer with resistance and flux leakage.

The design of a transformer is dependent on several parameters. According to basic electromagnetic theory on transformers the electromotive force can be calculated according to Equation (3.5)

$$E_{rms} = \frac{2\pi f N B A}{\sqrt{2}} = 4.44 f N B A \tag{3.5}$$

where f is the rated frequency, N is the number of winding turns, B is the magnetic flux density and A is the area of the core. For an LFAC system, the frequency is reduced by $\frac{1}{3}$, which means that the other parameters have to increase by a factor of 3 to maintain the same electromotive force. Based on the fact that magnetic flux density remains the same with the variation of frequency, the only way of maintaining the required voltage is to increase the number of turns or increase the thickness of the core. According to [27], increasing the thickness of the core and keeping the number of windings unchanged increases the width and height of the transformer by a factor of 1.4. This increases the weight of the transformer by a factor of 3. However, keeping the same core diameter and increasing the number of turns gives a lighter design, approximately twice the weight of a 50 Hz transformer. It is evident that a reduced frequency leads to a heavier transformer, hence impacting the required size of the offshore platform.

3.3.2 HVDC

The history of HVDC started with the invention of mercury arc rectifiers in the 1930s. In 1941 the first HVDC link was ordered to supply Berlin with 60 MW, but due to World War II it was never operational. Some years later, in 1944 Uno Lamm had developed a test system in Ludvika that was capable of transmitting 2000 kW at a voltage level of 60 kV. In 1954 the first commercial HVDC system was operational with a rating of 20 MW supplying the island of Gotland from the Swedish mainland at a voltage of 100 kV. Thyristors were later developed and put into service at the Gotland link increasing the transmission capacity by 50 % at a voltage level of 150 kV in 1970. Since then the technology has matured due to some of its characteristic features. HVDC has long transmission capabilities due to lower losses at long distances mainly related to the absence of reactive components that exist in AC systems. Since it converts AC to DC and then DC back to AC, it is also capable of interconnecting non-synchronous systems. The HVDC links can also be used to improve the stability of the AC system [28]. Therefore a lot more HVDC links have been installed and in December 2019 an HVDC link spanning over 3300 km with a capacity of 12 GW at 1100 kV was completed [29].

3.3.2.1 Line-commutated current-source converter HVDC

As HVDC was developed and commercially available in the 1950s and onward, the three-phase converter technology used was the Current Source Converter (CSC) based on mercury-arc valves, and during the 1970s the thyristor valve was commercialized [30]. The characteristical difference between a CSC and a VSC is that for a CSC, the DC-current always flows in a single direction whilst for a VSC the DC voltage always has the same polarity. So for a power reversal to take place in a CSC, the DC voltage has to be reversed. An illustration visualizing the CSC's operational principles is presented in Figure 3.10.

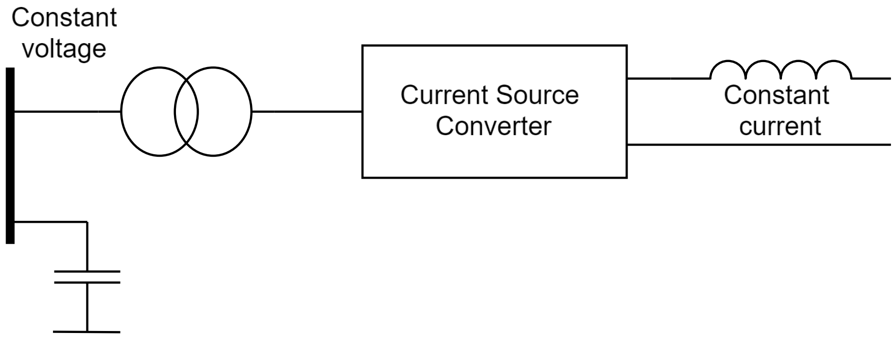

Figure 3.10: Operational principles of a LCC.

Since a CSC is a thyristor-based technology, the only possible control is the firing angle. A thyristor can be controlled to start conducting when the voltage from the anode to the cathode of the thyristor is positive, and a firing pulse is given. Considering a three-phase half-wave rectifier as seen in Figure 3.11, the output voltage can be controlled by varying the firing angle α.

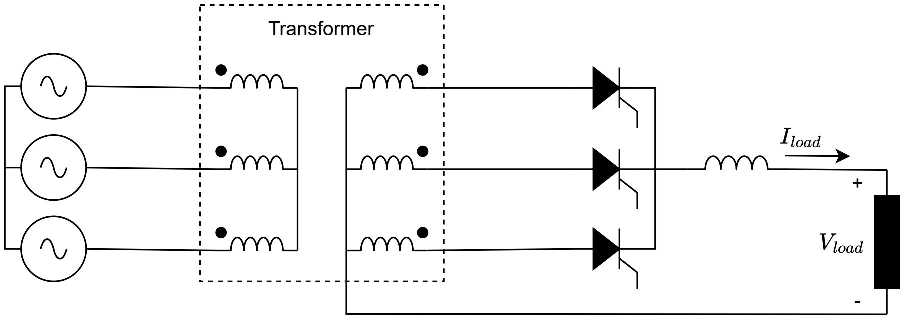

Figure 3.11: Schematic diagram of a half-wave three-phase converter.

In a three-phase rectifier operation, α is measured from the point where the supplied voltages from the three phases cross over each other since at that point the thyristor becomes forward-biased. As seen in Figure 3.12, the voltage of phase A is greater than the voltage of phase C from 0° until 180°. Therefore the theoretical range to fire the gate pulse for the delay is when the thyristor is forward biased, hence when α is between 0° until 180°. However, due to commutation problems α is slightly reduced.

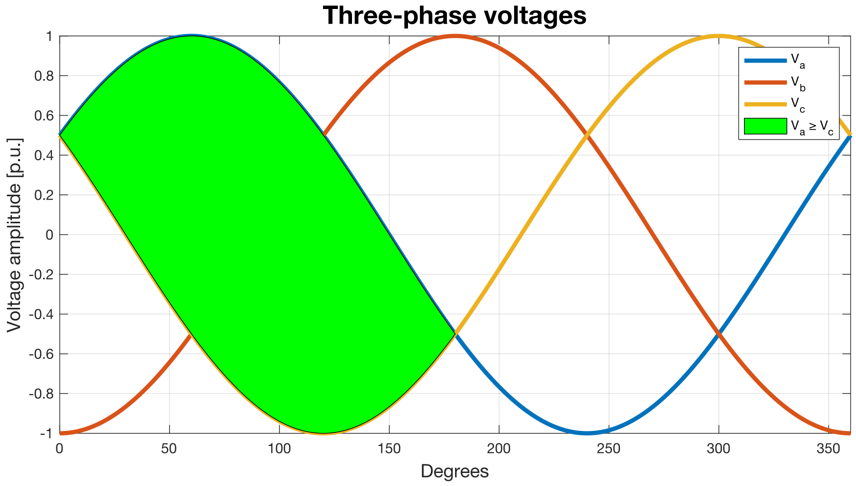

Figure 3.12: One period of normalized three-phase voltages where the area of $V_a \geq V_c$ is shaded.

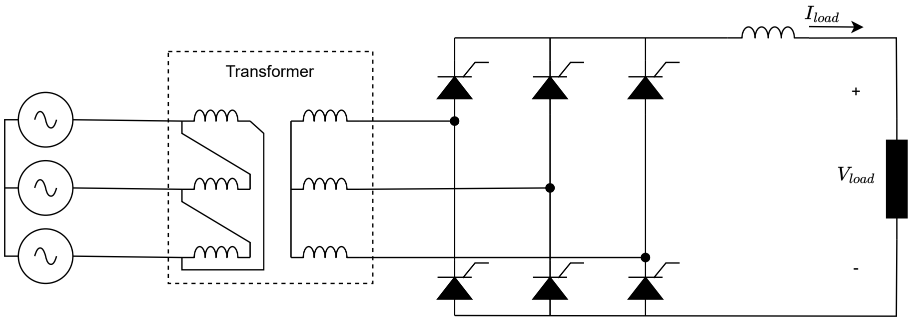

Figure 3.13: Schematic diagram of a full-wave three-phase converter.

To increase the average DC-output voltage, more thyristors are added such that two groups of three-phase half-wave rectifiers are used which compose a so-called three-phase full-wave converter as seen in Figure 3.13. The three thyristors on top will produce a positive voltage compared to the neutral, and the group of three at the bottom will generate a negative voltage compared to the neutral. Therefore twice the DC voltage will be generated with the full-wave rectifier compared to the half-wave. Since both the negative and the positive periods are utilized, no DC component will be present in the transformer windings. This technique is widely used because a special transformer is not needed and it works as a six-pulse rectifier. Furthermore, since the converter utilizes the full sinusoidal waveform, it can operate both as a rectifier and an inverter by controlling the firing angle of each thyristor. Therefore the converter will theoretically operate as a rectifier if α is less than 90° and an inverter if α is greater than 90°. However, due to the non-instantaneous commutation, an overlap period is needed.

Because of the low switching frequency, low-order harmonics will be present. If the phases are balanced third multiple harmonics will be trapped in the Δ-side of the transformer but positive sequence multiples, $6n + 1$, while the negative sequence multiples, $6n - 1$, will not. One solution to reduce the impact of harmonics is to use shunt-connected filters that are tuned to eliminate specific undesired orders of harmonics. If a six-pulse converter is used, then the filters would be tuned to eliminate the 6n±1 harmonics. There are converter solutions as well, where a typical converter solution for LCC-HVDC is the 12-pulse converter. The power transformer of the 12-pulse converter has two branches, one Y/Y branch, and one Y/Δ branch. Each of these branches is then connected to a full-wave converter as seen in Figure 3.14. The 12-pulse converter allows odd multiples of 6n±1 to cancel each other out if the transformer ratios are chosen correctly. Hence the 12-pulse converter only contains harmonics of the order 12n±1 which reduces the size of filters since the harmonic content is pushed up in the frequency spectra [31].

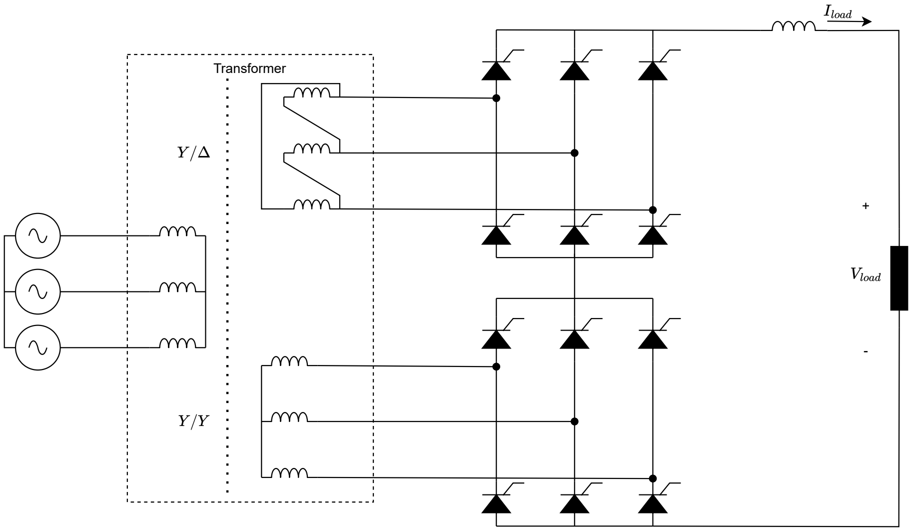

Figure 3.14: Schematic diagram of a 12-pulse converter.

3.3.2.2 Voltage source converter HVDC

In the 1990s self-commutating switches such as the Gate Turn-Off thyristor (GTO) and the IGBT became commercially available, and the operational principles are presented in Figure 3.15. The major difference between self-commutating switches and line-commutating switches is that the self-commutating switches can be controlled to both start and stop conducting. Since the switches can be controlled to stop conducting, multiple switching events per switch per period are possible compared to the line-commutated switches where only one switching event per period is possible. Since the thyristor commutates at the current natural zero-crossing, it is reliant on an AC source. As the VSC commutation can be fully controlled, it can operate independently of an AC source. Therefore a benefit is the independent control of voltage and current, the result is that active and reactive power can be fully controlled independently of one another. Since the VSC can be operated with frequencies in the kHz range, the harmonic content is pushed up in the spectra. The result is that the size of filters can be drastically reduced because of the higher-order harmonics [30], [28].

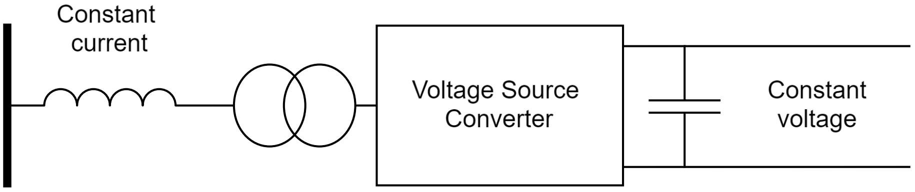

Figure 3.15: Operational principles of a VSC.

A common modulation technique is Pulse Width Modulation (PWM). In PWM, commonly a sinusoidal modulating wave with the frequency f_1 equal to the desired power system frequency is compared to a triangular wave with its frequency equal to the converter switching frequency f_{sw}. The purpose of the comparison is to determine when the IGBTs should conduct or not. If the magnitude of the sinusoidal modulation wave is $\hat{V}_{mod}$, and the magnitude of the triangular wave is $\hat{V}_{tri}$, then the amplitude modulation index m_a, and the frequency modulation index m_f can be determined as in Equation (3.6)

$$\begin{aligned} m_a &= \frac{\hat{V}_{mod}}{\hat{V}_{tri}} \\ m_f &= \frac{f_{sw}}{f_1}. \end{aligned} \tag{3.6}$$

In a half-bridge single phase VSC is considered, see Figure 3.16, where the output voltage V_{out} is the voltage between terminals A and 0. The switch to be turned on is determined by comparing the reference and the carrier waves. The first event that results in $V_{out} = \frac{U_{dc}}{2}$, is when T1 is turned on, and T1 will conduct when $V_{mod} > V_{tri}$. The other event that results in $V_{out} = -\frac{U_{dc}}{2}$, is when T2 is turned on, and T2 will conduct when $V_{mod} < V_{tri}$. Depending on the relation between the sinusoidal and the triangular wave the output voltage will vary between either positive or negative

$\frac{U_{dc}}{2}$ as seen in Figure 3.17a where the gate signal is presented. Hence it is important to keep $m_a \leq 1$, otherwise, the amplitude of the sinusoidal wave is greater than the triangular. If $m_a > 1$, $V_{mod} > V_{tri}$ will be satisfied for longer than desired which results in overmodulation as seen in Figure 3.17b. Overmodulation decreases the switching frequency which brings the harmonics further down in the frequency spectra [32].

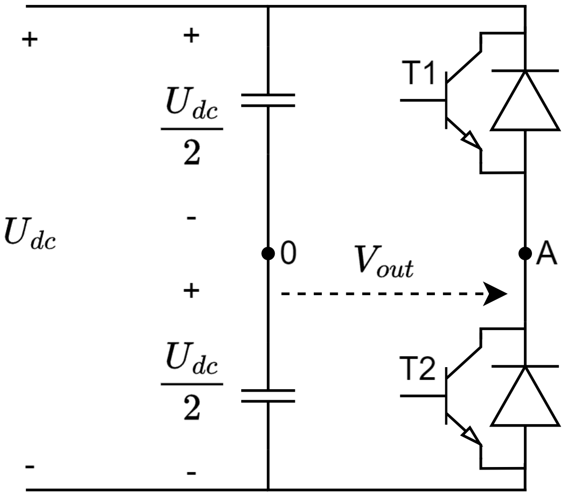

Figure 3.16: Diagram of a single-phase half-bridge VSC.

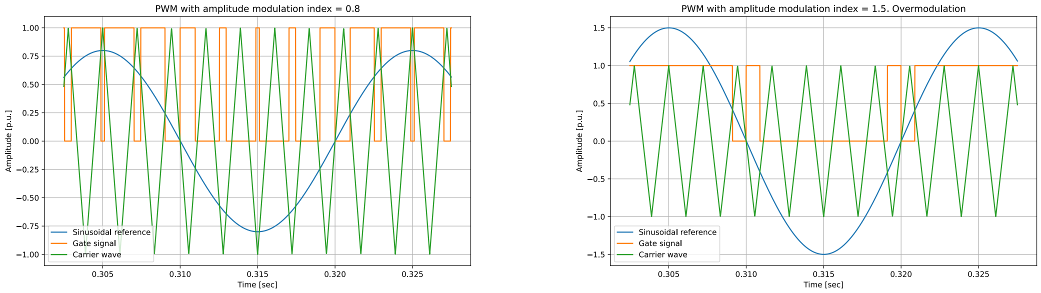

(a) $m_a = 0.8$.

(b) Overmodulation. $m_a = 1.5$.

Figure 3.17: PWM output depending on the amplitude modulation index.

If a three-phase full-bridge converter is considered as seen in Figure 3.18. Three sinusoidal modulating waveforms shifted 120° from each other can be used that are compared to one triangular carrier wave. This reproduces three phase shifted voltages between the terminals V_a, V_b, and V_c to the neutral point N [32].

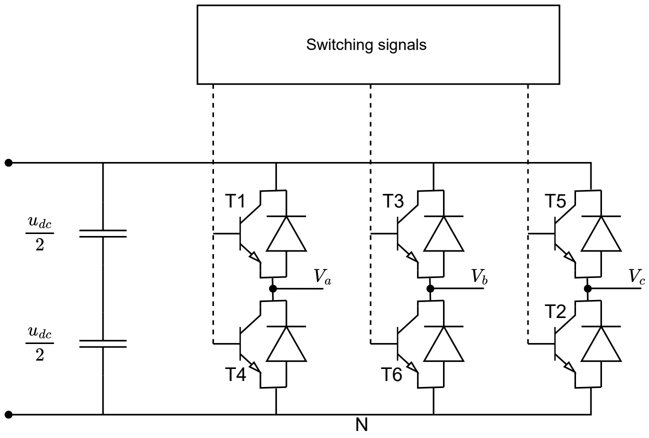

Figure 3.18: Diagram of a three-phase full-bridge VSC.

3.3.2.3 Multilevel- and modular multilevel converters

The previously mentioned VSC converters are two-level converters meaning that the output voltage is switched between the polarities of the DC supply. By installing more DC-link capacitors, more output voltage levels can be achieved since the blocking capability is determined by the DC-link capacitor instead of the DC-supply voltage. Due to there being more semiconductors in a multilevel converter that does not have to be switched at the same time, the frequency of the output voltage can be increased without increasing the switching frequency of a single semiconductor. Hence pushing the harmonics upwards in the spectrum. Also, since there are more voltage levels, the amplitude of the harmonics will be reduced due to the reduced change in voltage level between the switching events for the output voltage. If more levels are added, a closer voltage level to the desired sinusoidal waveform can be obtained. Hence the outputted voltage appears more sinusoidal for each voltage level added [33].

The simpler versions of multilevel converters such as the diode clamped converter, and flying capacitor converter are suitable for low- to medium-voltage applications. However, when it comes to high-voltage applications their circuits and their control become too complex. Hence the Cascaded Multilevel Converter and the Modular Multilevel Converter (MMC) were developed. The Cascaded Multilevel Converter introduced semiconductor submodules that can be series connected to achieve more intermediate voltage levels. Each submodule consists of either a half-bridge or a full-bridge connected in parallel with a capacitor. Therefore the output of each half bridge submodule can either be zero or the capacitor voltage. Since the full bridge has four switches its submodule can provide four switching states. A series connection of these submodules is called a string where the half-bridge has $N + 1$ levels, and the full bridge has $2N + 1$ stages [33].

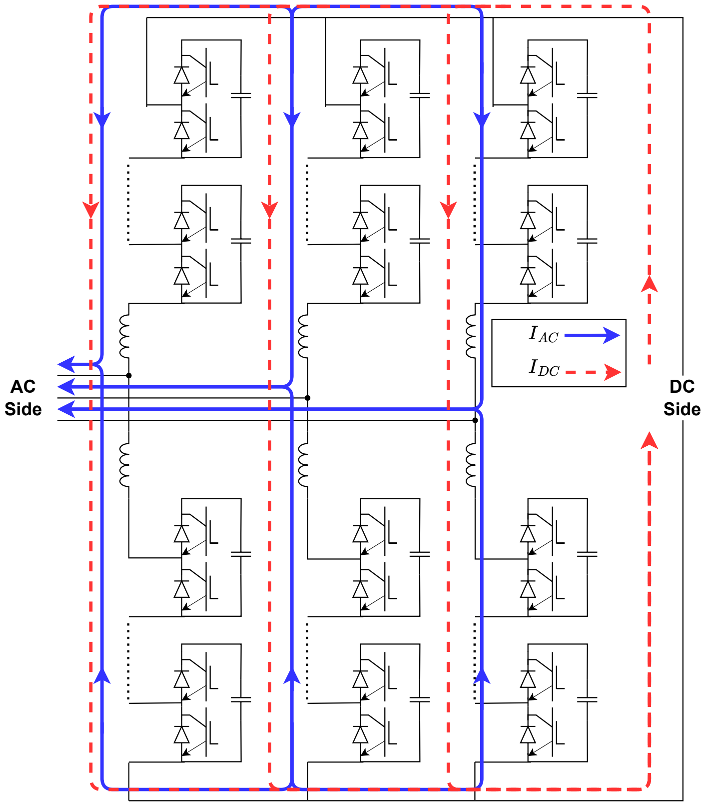

Figure 3.19: MMC design and its current paths for HVDC applications.

As for the MMC, instead of the valves for a two-level converter, the MMC uses strings of submodules. The MMC differs from the Cascaded Multilevel Converter majorly in one way, which is that for the Cascaded Multilevel Converter, each submodule needs an isolated feed from a transformer and is thereby not classified as fully modular. Typically the MMC is built with three phase-legs like the two-level converter but with two submodule strings for each phase with a midpoint connection in between as seen in Figure 3.19. One string from the positive DC-polarity, and one from the negative DC-polarity. These strings contain a certain number of submodules which corresponds to the number of levels the converter can operate at. The AC terminals are then formed at those midpoint connections for each phase-leg. For other applications that require another amount of phases, the number of phase legs of the MMC can be altered. The operational principle is to switch on a certain number of submodules such that the combined voltage of the phase-legs reaches the desired voltage level. As each string consists of a high number of submodules, a very sinusoidal output can be achieved by turning on or off one submodule at a time. Another benefit of the great number of submodules is a very high switching frequency which raises the harmonics high up into the spectra. If the DC-side current is constant the MMC will provide a constant voltage on the DC-side, and if the MMC provides symmetric AC voltage the AC-side current will be symmetric. As seen in Figure 3.19, the DC-side current will be distributed evenly among the three phase-legs and so does the currents on the AC-side. If the AC side currents are distributed symmetrically, the currents in the three phases will be canceled at the converters DC side. Hence no AC harmonics will be injected to the DC side [33].

3.3.2.4 Grid-following vs grid-forming converters

There are two different operational principles for a converter, it can either be grid following or grid forming. The grid-following converter acts like a current source. To inject a certain power into the connection point, the converter varies the active- and reactive current it provides. However, in case of a disturbance in the connected grid, it requires an additional voltage source for the voltage and frequency set points. Therefore the grid-following converter is not suitable for handling disturbances in the grid since it synchronizes via a phase-locked loop (PLL). The next converter type is the grid-forming converter which acts like a voltage source. Some grid-forming strategies do not rely on the PLL to synchronize with the grid and therefore instead act like a synchronous machine. Hence the grid forming converter can vary its injected power and is therefore a suitable solution during disturbances or island operation [34].

3.3.2.5 HVDC link configurations

Monopolar

There are several methods used to connect point-to-point configurations of HVDC. The first and simplest configuration is the monopolar link, an example of an LCC-based point-to-point HVDC connection is seen in Figure 3.20. There are two different types of monopolar links available and the commonality is that both types use a single converter in each station. The first one is the asymmetrical monopole. For the asymmetrical monopole, the neutral is grounded and the return either flows through a ground return or a conductor [35]. The operational principle of an asymmetrical monopolar link is that there is one pole and one return path [28]. In VSC-HVDC, commonly the return current goes through a conductor. As there is only one pole, the applied voltage can either be positive or negative. However, if a negative voltage is used, the effects of corona can be heavily mitigated. Hence a negative polarity is commonly used for the monopolar configurations [30]. The second type is the symmetrical monopole. The difference from the asymmetrical monopole is that the symmetrical monopole is grounded in between the positive and negative poles [35].

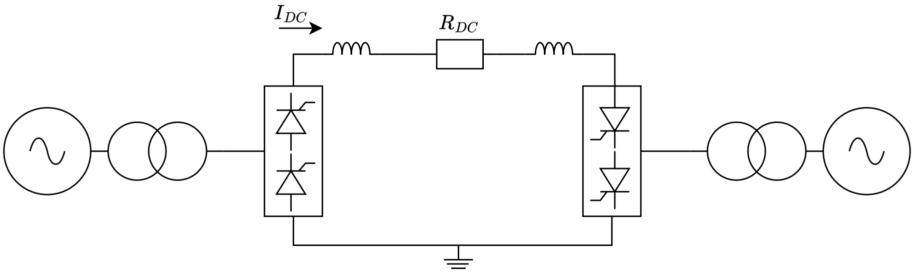

Figure 3.20: Line diagram of a point-to-point LCC based asymmetric monopolar HVDC configuration.

Bipolar

Another configuration of point-to-point HVDC link is the bipolar link, an example of a VSC-based point-to-point HVDC connection is seen in Figure 3.21. As its name states, the bipolar link has two poles, one with negative voltage, and one with positive voltage. The neutral points between the positive and the negative poles are grounded. During steady-state operation, the current is split among the two poles, and therefore at steady-state operation, no current will flow through the return path. A benefit of the bipolar link is that in case of a failure at one of the poles, the other pole can still be operated as a monopolar link using the ground return [28].

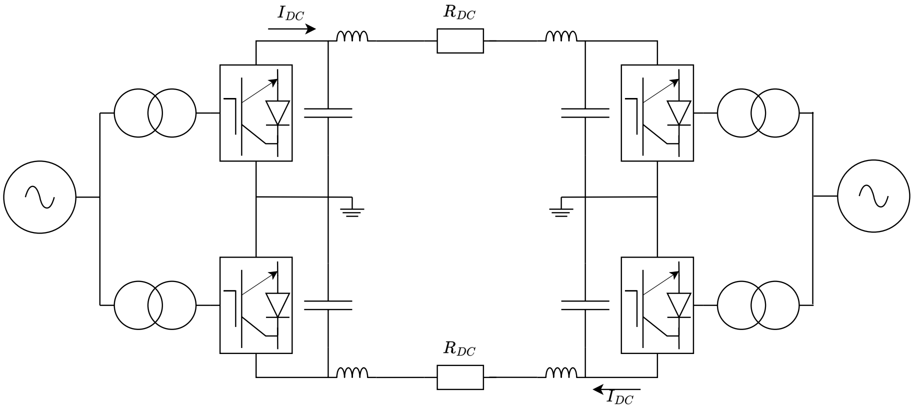

Figure 3.21: Line diagram of a point-to-point VSC based bipolar HVDC configuration.

Homopolar

Another configuration is the homopolar. For a homopolar link, there are two poles at the same polarity, usually negative polarity due to corona discharges, with a ground- or conductor return. As the two poles have the same polarity, insulation distances can be reduced due to the reduced voltage gradient which lowers the investment cost. As in a bipolar link, the return current is canceled out due to the opposite polarities. However, a ground return is required for a homopolar link to carry the return current, hence a bipolar link is often preferred over a homopolar link [31].

3.3.3 LFAC

LFAC is a commonly used frequency used within the railway network. The railway power supply has a frequency of 16 $\frac{2}{3}$ Hz whereas the frequency for public electricity supply is 50 Hz. Using the frequency 16 $\frac{2}{3}$ Hz within the railway network dates back to the 20th century as the earliest electric motors for trains required this frequency to function. European countries (including Switzerland) commonly agreed after various trials to adhere to the frequency of 16 $\frac{2}{3}$ and it is still in use today. The railway network is powered by the public grid which has to be converted to 16 $\frac{2}{3}$ Hz. The voltage must also be stepped down to a suitable voltage level required voltage level by locomotives [36].

3.3.4 LFAC specification

For an AC transmission system, the transmitted active power is expressed in Equation (3.2). Under the assumption of a fixed angle δ, and fixed sending and receiving voltage, then the only way of improving the transmission capability is to reduce the impedance of the cable. The cable is reactance-dominated, meaning that the reactance of the cable is much larger than the resistance. The reactance of the cable, X, can expressed as Equation (3.7)

$$X = 2\pi f L \tag{3.7}$$

where X is the cables reactance, f is the power frequency and L is the total inductance of the cable. This equation visualizes the main concept of LFAC, a reduced frequency increases the transmitted power proportionally. Another fundamental concept of an LFAC configuration is its ability to improve voltage stability given the same amount of reactive power transmission. The relation between voltage drop and reactive power is expressed in Equation (3.8)

$$\Delta V\% = \frac{QX}{V^2} \cdot 100 \tag{3.8}$$

where ΔV is the voltage drop over the cable, V is the nominal voltage and Q is the reactive power flow of the cable. Since the reactance of the cable is reduced due to the lower grid frequency, the voltage drop across the cable is also reduced proportionally [37].

3.3.4.1 Frequency converters

To convert the export systems grid frequency of $16\frac{2}{3}$ Hz into the grid frequency of 50 Hz a frequency converter is needed. There are multiple converters that are capable of this such as a back-to-back VSC, or an AC-DC-AC converter. There are also AC-AC converters such as the cycloconverter, and Modular Multi-level Matrix Converter (MMMxC or M^3C). The cycloconverter as seen in Figure 3.22 is a common converter type used in railway systems to step down the grid frequency.

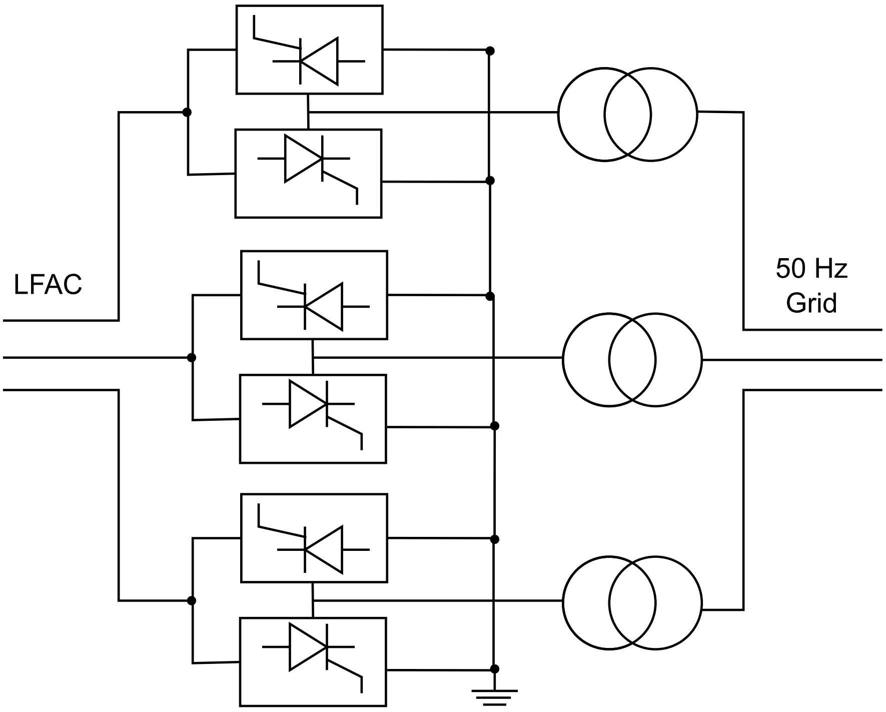

Figure 3.22: Circuit diagram of a cycloconverter.

The cycloconverter is a thyristor-based converter where each phase connected through a single-phase transformer is connected to a 12-pulse converter, one positive 6-pulse, and one negative 6-pulse converter. Hence the cycloconverter is typically a 36-pulse converter where the output is controlled by varying the firing angle of the thyristors. When a cycloconverter is used to step down the frequency, the ratios of the two frequencies typically have to be below 0.7 due to power quality constraints. The harmonics of the cycloconverter are dependent on the ratio between the two frequencies, for some ratios the order of the harmonic content can be below the order of the output frequency, these are called sub-harmonics. Also, inter-harmonics will be present which occurs when the output frequency is higher than the input frequency. In the case of LFAC, the ratio is 3 which results in harmonic content at multiples of the output frequency. Therefore as harmonics are present at low order, it becomes complex to filter out the harmonics from the desired waveform which results in large filters [23].

To combat the issues of the low order harmonics and its related problems, a matrix converter, as seen in Figure 3.23a, can be used. As observed, a DC-link is not present because bi-directional switches are used which results in direct AC-AC conversion and an increased efficiency compared to when a DC step is present. However, for the standard matrix converter, the voltage is limited which has been proposed to be solved by using the M^{3}C as seen in Figure 3.23b. For the M^{3}C, the switches are replaced by submodules containing full-bridges made up of four IGBTs and one capacitor just like the MMC. Hence a combination of the matrix converter and the MMC achieves high-order harmonics with a highly sinusoidal output. However, due

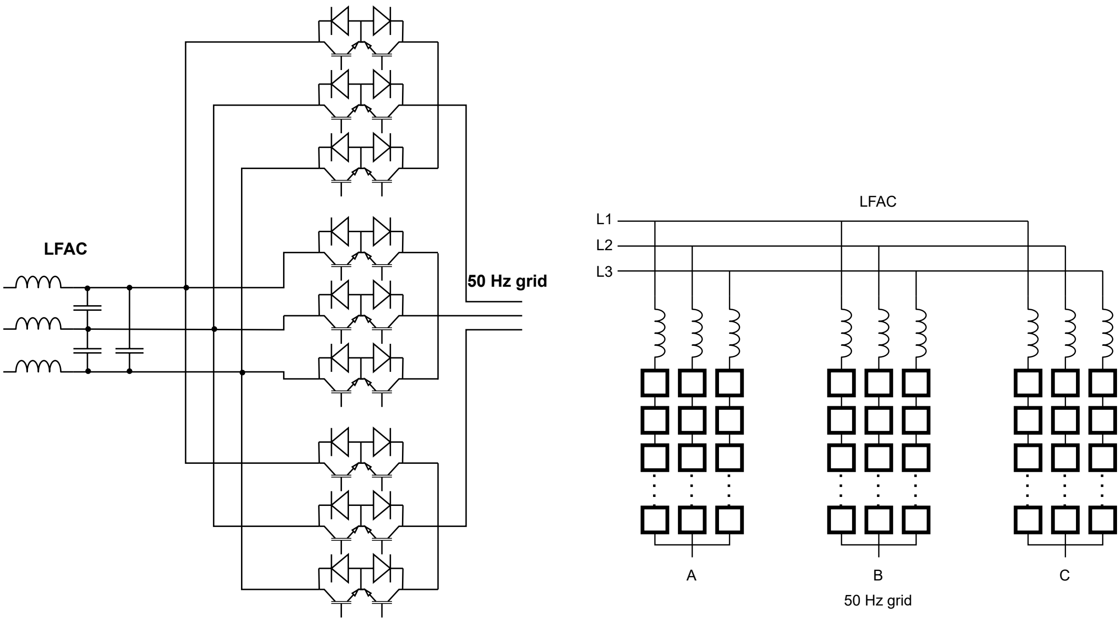

(a) Matrix converter

(b) M^{3}C

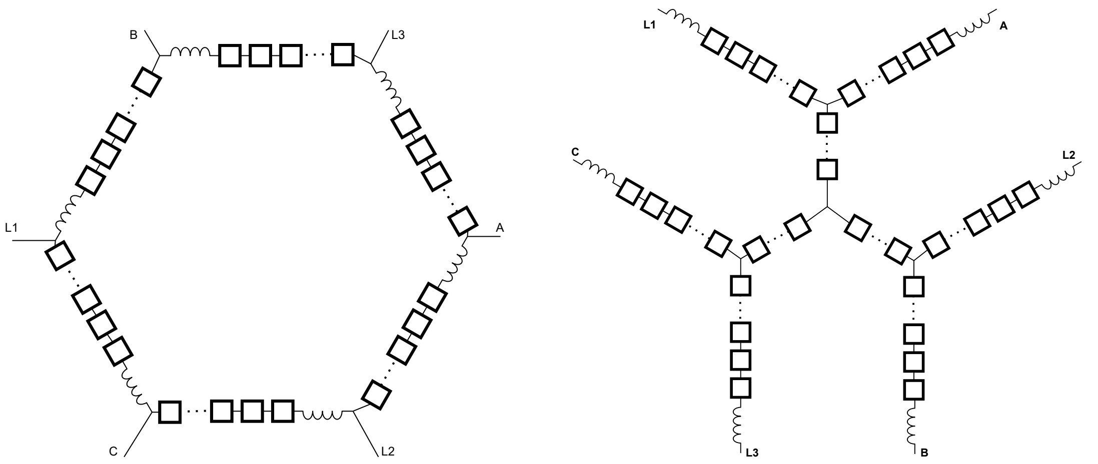

(c) Hexverter

(d) YMMC

Figure 3.23: Schematic diagram of matrix- and multi-level matrix converters [38].

to the great number of switching devices, the complexity is increased. Due to the benefits of using an M^{3}C such as high order harmonics, highly sinusoidal output, and grid forming capabilities, it has been suggested as a solution for integrating offshore wind by utilizing a low-frequency export network with the M^{3}C placed onshore. Future converter topologies have also been proposed, namely the Hexverter that uses six arms which is fewer compared to the back-to-back VSC and M^{3}C. Another proposed converter topology to solve the problem of circulating currents which results in losses is the Y-connected YMMC converter. The collective name for all these frequency matrix converters in this report is Static Frequency Converters (SFC). The hexverter can be found in Figure 3.23c and the YMMC converter in Figure 3.23d [23], [38].

3.3.5 Reactive power compensation

To alter the impedance characteristic and thereby the response of the system to different operational scenarios, compensators are used. This sub-chapter presents different solutions for passive and active shunt and series-connected compensators widely used in power systems.

3.3.5.1 Passive shunt compensation

The first types of shunt compensators are the passive shunt compensators. Passive shunt compensators are either reactors or capacitors connected in shunt with the system. The purpose of the shunt-connected components is to permanently alter the impedance characteristics of the system for power factor correction. The shunt reactors are typically installed in capacitive systems to limit the capacitive effects. In systems where the Ferranti effect is suspected to cause problems, shunt reactors can be installed to limit the effects of line charging and thereby preventing the receiving end voltage from violating the voltage limits. Vice versa, the passive shunt-connected capacitors are mainly used to boost the voltage by producing reactive power. The shunt-connected capacitors are widely used in distribution systems for power correction since most installed loads are of an inductive nature. Although the shunt capacitors have one major drawback, as the voltage decreases, the produced VArs decrease as well since it scales with the voltage squared. Hence, when the most reactive support is needed, the shunt-connected capacitors produce less reactive power [39].

3.3.5.2 Thyristor controlled reactor

The first controllable shunt compensator is the Thyristor Controlled Reactor (TCR). It is commonly implemented with a reactor in series with two thyristors connected in anti-parallel, this can be seen in the single-phase diagram of the TCR presented in Figure 3.24.

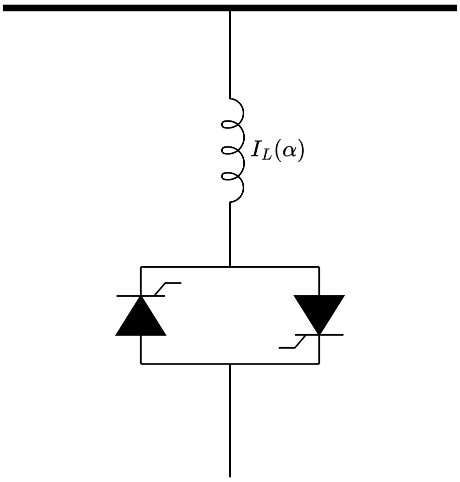

Figure 3.24: Schematic diagram of a single-phase TCR.

By connecting the thyristors and the inductor this way, the current passing through the reactor is easily controlled by controlling the firing angle (α) of the thyristors. If the current lags 90° behind the voltage (sinus reference), and α is equal to 0°, the thyristor will start to conduct at the voltage maximum amplitude. According to the equation of an inductor, the current will increase until the voltage reaches its natural zero-crossing, then the current will decrease until the thyristor stops conducting at the current's natural zero-crossing. If a firing angle is introduced, the thyristor will start its conduction later but the current will still reach its maximum at the voltage natural zero-crossing. Hence the amplitude of the current will be reduced if the firing angle is increased. So by altering α, the current through the inductor can be controlled, which in turn affects the reactance seen by the circuit. The current can be calculated as in Equation (3.9)

$$I_L(\alpha) = \frac{V}{\omega L}\Big(1 - \frac{2}{\pi}\alpha - \frac{1}{\pi}sin(2\alpha)\Big) \tag{3.9}$$

where L is the inductance of the reactor, $I_L(\alpha)$ is the controlled reactor current, V is the AC voltage, ω is the angular frequency, and α is the firing angle in radians. Hence, if the firing angle is equal to 0°, the inductor is fully inserted. If α is equal to 90°, the point where the voltage reaches its natural zero-crossing, the thyristor won't conduct hence the inductor is fully taken out [20].

3.3.5.3 Thyristor switched capacitor

The next shunt compensator is the Thyristor-Switched Capacitor (TSC) shown in Figure 3.25. Like the TCR, the TSC is a shunt device, but instead of an inductor, a capacitor is connected in series with the thyristors. An inductor is also connected in series to limit the surge current passing through the components in case of abnormal operating conditions. Due to $\frac{di}{dt}$, to have transient free switching, control of α to vary the reactance is not possible. Hence the TSC can either be fully on and thereby provide reactive power to the circuit, or it can be turned off [20]. Hence a TSC is not controllable, just switchable.

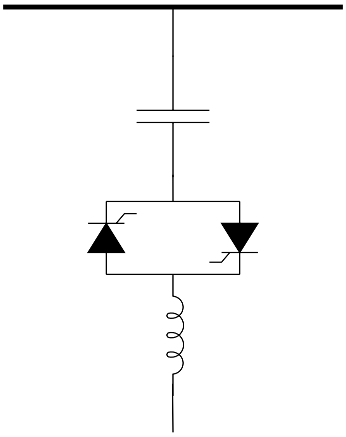

Figure 3.25: Schematic diagram of a single-phase TSC.

3.3.5.4 Static VAR compensator

To control the reactive output of the TSC it can be combined with the TCR into one shunt device called the Static Var Compensator (SVC). SVC is a collective name for various configurations of shunt-connected inductors and capacitors. One example would be the TCR-TSC that is found in Figure 3.26. By combining the controllable TCR and the switchable TSC, the combined reactance can be controlled and thereby also the reactive power consumed or produced. If the TSC is on, and the firing angle α of the TCR is equal to 90° the SVC will produce its maximum VAR output. Vice versa, if the TSC is off and the firing angle α of the TCR is equal to 0° the SVC will consume its maximum VAR capability. By altering if the TSC is on or off, and the firing angle, the SVC can produce or consume any VAR amount in between the previously stated limits. Therefore it is also possible to have multiple TSC branches connected while the TCRs reactive capacity can be equal to the reactive capacity of one TSC stage, that is a so-called nTSC-TCR. So if two equal TSC branches are turned on, the controllable TCR could then vary the reactive power output of the SVC between the two capacitive stages. However, since the TCR will have to absorb some amount of reactive power from the TSC, a current will go from the TSC to the TCR resulting in non-contributing losses. If one compares it to an SVC with a fixed capacitor (FC) stage (non-switchable), since the capacitor stage is constantly on, there will be losses at zero reactive power contribution which is not the case when a switched capacitor is used [20].

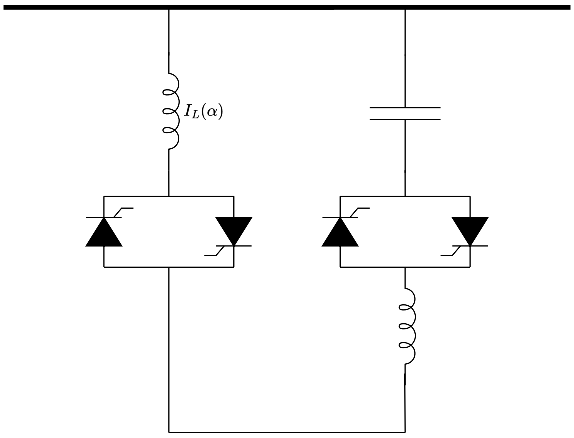

Figure 3.26: Single-phase diagram of a TCR-TSC.

3.3.5.5 Static synchronous compensator

The next shunt device is the Static Synchronous Compensator (STATCOM). For the TCR and the TSC, inductors and capacitors were used as reactive energy storage to control the produced or absorbed reactive power. But for a STATCOM there are no such components to store the reactive energy, instead the currents are circulated between the AC systems phases. A diagram of the STATCOM can be found in Figure 3.27.

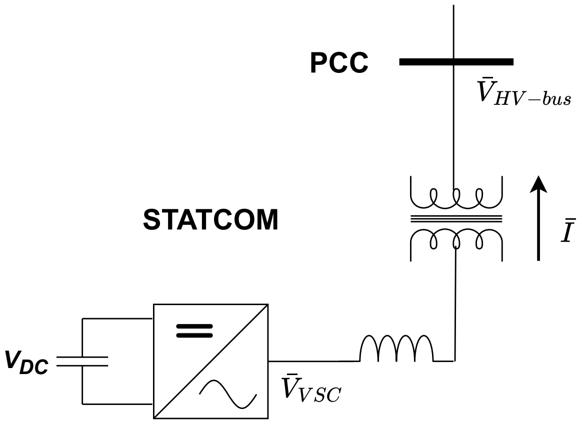

Figure 3.27: Single-phase diagram of a STATCOM.

The operating principle of a STATCOM is that by using a VSC, the complex voltages and currents can be controlled to obtain either leading or lagging VAR production. At the DC side of the VSC, a DC capacitor is connected to the VSC to enable the operation of the VSC since the VSC itself has no means of providing the power. To keep the DC-capacitor charged, a small active current is drawn by lagging the STATCOMs output slightly. On the AC side after the VSC, a smoothening inductor is installed to remove high-order harmonics and to enable the voltage difference [32]. The complex quantities can simply be controlled to either produce or consume reactive power just like a synchronous machine can be over- or under-excited to regulate VAR production. If a synchronous machine is considered with its internal voltage E, connected to a bus with voltage V over X, then the exchanged reactive power Q could be calculated as in Equation (3.10)

$$\begin{aligned} I &= \frac{V-E}{X} \\ Q &= \frac{1-\frac{E}{V}}{X}V^2. \end{aligned} \tag{3.10}$$

Therefore by controlling the amplitude of E and V, the injected or absorbed reactive power can be controlled. If for the synchronous machine $E > V$, the machine is over-excited. The result of the machine being over-excited is that the current leads the voltage, hence the synchronous machine is seen as a capacitance by the rest of the system. If instead $E < V$, the current instead lags the voltage and the machine is seen as an inductor by the rest of the system.

By letting the VSC of the STATCOM mimic the behavior of the synchronous machine, the same results can be accomplished, although with a power electronic solution instead [20]. Since the STATCOM has no energy storage, only VAR control is possible. Therefore, if the circuit losses of the STATCOM are neglected, only reactive power is exchanged with the PCC by producing a current either leading or lagging by 90° compared to the voltage at the PCC. In Table 3.2, the operating modes are presented [32].

Table 3.2: Operating modes of STATCOM depending on complex voltage quantities [32].

Complex voltage component	Operating mode
$V_{HV-bus} > V_{VSC}$	Absorb VAR
$V_{HV-bus} < V_{VSC}$	Produce VAR
$-\delta$	Absorb Watt
$+\delta$	Produce Watt. Only possible with energy storage.

3.3.5.6 Enhanced STATCOM

The Enhanced STATCOM (E-STATCOM) is a shunt-connected device that is a combination of a conventional STATCOM with added energy storage. The major difference between STATCOM and the E-STATCOM is that due to the added energy storage, the E-STATCOM is able to produce and absorb both reactive and active power as seen in Table 3.2. Therefore the E-STATCOM can aid the connected system with voltage control, unbalances, faults, oscillation dampening, and frequency regulation. The energy storage can consist of battery cells, supercapacitors, fuel cells, or combinations of them. The amount and duration of the active power support is therefore limited by the size of the installed energy storage [40].

3.3.5.7 Series compensation

As previously stated, shunt compensation is effective to regulate the voltage along a line, or at the load of a two-bus system. It is also possible to regulate the transmitted active power but it is highly ineffective. A more effective method to increase the transmitted power is to use series compensation. To increase the active power transmitted by ΔP, the required reactive power relation between series and shunt compensation is as seen in Equation (3.11)

$$\frac{\Delta Q_{Series}}{\Delta Q_{Shunt}} = tan^2(\frac{\delta}{2}). \tag{3.11}$$

The equation for the transmitted active power from one bus to another is described in Equation (3.12)

$$P = \frac{V_1 V_2}{X_{eq}} sin(\delta), \tag{3.12}$$

a viable option is to change the equivalent reactance of the line. If an inductive overhead line is considered, a solution to reduce the equivalent reactance is to install a capacitor in series along the line since the equivalent reactance is $X_{eq} = X_L - X_C$. Therefore, if the equivalent reactance is reduced the active power will increase since the reactance is in the denominator of the formula. Another benefit of series compensation is that the transient stability margin is increased. If X_{eq} is reduced while the voltages V_1 and V_2, and the transmission angle δ are unchanged, the amplitude of the electrical active power will be increased in Figure 3.28. Therefore, since more active power can be transferred at the same transmission angle, the margin of the decelerating area is increased compared to the case without series compensation as seen in Figure 3.28 [20].

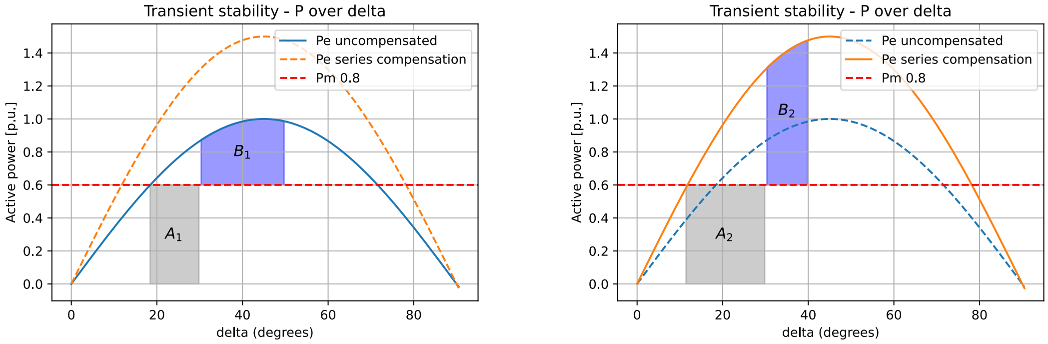

(a) $P-\delta$ curve - Uncompensated line ***(b)*** $P-\delta$ curve - Series compensated line

Figure 3.28: Comparison of transient stability related to series compensation.

The previously mentioned method of series compensation is a passive method meaning that the reactance of the line cannot be altered. A similar method to the shunt-connected SVC (FC-TCR) can also be applied as series compensation. Instead, a TCR in parallel with an FC is connected in series with the line as seen in Figure 3.29, which is called Thyristor-Controlled Series Compensation (TCSC). For a TCSC the equivalent reactance of the TCSC can be varied both in the inductive and the capacitive region such that the equivalent reactance of the line can be altered. This is achieved by changing the firing angle α of the thyristors in the inductor branch. However, all values of α are not possible due to resonance in the TCSC between the inductive and capacitive branch [20].

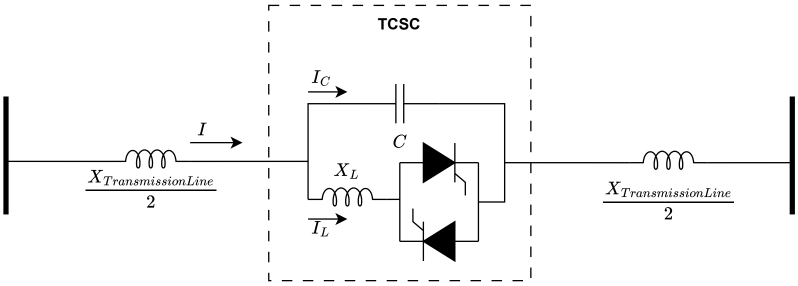

Figure 3.29: Single-phase diagram of a TCSC.

4

Economical overview

This chapter showcases the fundamental equations used when evaluating the three configurations from an economical point of view.

4.1 Net Present Value - NPV

A metric of interest is Net Present Value (NPV) which captures the revenue impacts of the installed energy source. The NPV of a renewable energy project is calculated by using Equation (4.1)

$$NPV = \sum_{i=1}^{N} \frac{(AR - AC)}{(1+r)^t} - CC \tag{4.1}$$

where CC is the capital cost (investment) of the system in \$, AR is the annual revenue of the system in \$, AC is the annual cost of the system in \$, r is the discount rate, and n is the expected lifetime of the installed technology. The annual revenue of the system is given by the price at which electricity can be sold at multiplied by the produced electricity. The annual cost of the system includes the cost of operating and maintaining the installed system. An NPV with a greater value than 0 represents a profitable investment. Despite the fact that NPV is an effective metric for capturing the profitability of an investment, it cannot rank and compare the configurations. Configurations with higher initial investment costs have a higher NPV but they might not necessarily have the best return on investment, hence why other metrics have been developed to enable ranking of the investment options [41].

4.2 Levelized Cost of Electricity - LCOE

The next metric is the Levelized Cost of Electricity (LCOE) which is defined as the cost at which electricity should be sold at for the investment to break-even at the end of its lifetime. LCOE is an effective indicator of the cost-effectiveness of the system since calculations can be made without assumptions regarding the uncertainty of future electricity prices. Comparing LCOE prices for each configuration will determine which investment is most advantageous. LCOE is mathematically defined by Equation (4.2)

$$LCOE = \frac{CAPEX + OPEX_i}{AEP_i} \tag{4.2}$$

where $CAPEX$ is the cost in \$ to build the entire offshore windfarm, $OPEX_i$ is the cost in \$ of operating the windfarm in the year i, and AEP_i is the annual electricity produced in MWh in the year i [41]. The annual electricity produced is calculated using Equation (4.3)

$$AEP = CF \cdot P_{PCC} \cdot t \tag{4.3}$$

where CF is the capacity factor (a ratio between annual electricity production and maximum annual energy capability), P_{PCC} is the active power flow in the point of common coupling, and t is the number of hours in a year. $CAPEX$ is assumed to be paid upfront for all the configurations which includes the cost of all the electrical components, platforms, transportation, and installation. The $OPEX$ cost is assumed to be paid annually, which means that the discount rate has to be considered when calculating the costs of operation and maintenance. Hence the OPEX and the AEP are based on their NPV at a given time. The finalized formula for determining the LCOE for each configuration is showcased in Equation (4.4)

$$LCOE = \frac{CAPEX + \sum_{i=0}^{N} \frac{OPEX_i}{(1+r)^i}}{\sum_{i=0}^{N} \frac{AEP_i}{(1+r)^i}} \tag{4.4}$$

where r is the discount rate in % and N represents the economic life of the wind farm [42]. Obtaining the point where the LCOE intersects between two configurations will determine the break-even distance with respect to the specific active power level studied. The configuration with the lowest LCOE is the most suitable configuration given a specific distance and installed active power level.

5

Electrical modeling

The electrical modeling consisted of parameterization of the components, and the methodology behind the modeling is showcased in this chapter. For the three export system topologies, some components shared parameters. As transformers are usually custom-made products where the parameters can vary substantially depending on the required specifications and on-site conditions. However, in this study, the same parameters were used for all transformer models, as presented in Table 5.1.

Table 5.1: Transformer parameters used for load-flow simulations [43].

Resistance [p.u]	Reactance [p.u]	No-load losses [kW/MVA]
0.005	0.15	0.04

In PowerFactory the wind turbines were modeled as an equivalent generator. For all topologies, the generators operate at 66 kV. The only difference is that for LFAC, the generator operates at $16\frac{2}{3}$ Hz, while it operates at 50 Hz for HVAC and HVDC.

All components, as well as the subsea cable, were rated to be less than 100 % loading at full generation conditions of the wind farm for all distances and power levels. The operating temperature of the cables was set to 90°C since the resistance of the cables increases with the operating temperature. The rating also involved that the voltage limits of under/over 0.95 - 1.05 p.u were not violated. As all models were implemented for all configurations, distances, and power levels, load-flow studies were performed. The following sections present the topology-specific modeling and parameterization.

5.1 HVDC models

The HVDC models were developed as symmetrical monopoles where two different DC-link voltages were used depending on the active power capability of the offshore wind farm. A DC-link voltage of ±150 kV was used for a wind farm with an installed active power ranging from 300 - 500 MW, while ±320 kV was used for a wind farm with an installed active power ranging from 500 - 1400 MW. Depending on the power level, the converter bus voltage was set to either 187.5 or 400 kV [44]. An overview of the two HVDC models is presented in Figures 5.1 and 5.2.

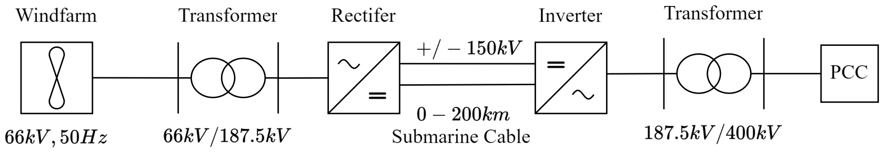

Figure 5.1: HVDC model for an installed active power ranging from 300 MW to 500 MW.

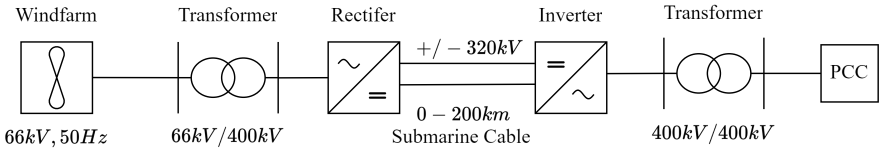

Figure 5.2: HVDC model for an installed active power ranging from 500 MW to 1400 MW.

The HVDC converters were modeled as PWM converters of the half-bridge MMC type with an efficiency of 99.3% each. The equipped station controller is the main difference between the rectifier and the inverter. The former uses *Vac-phi* control mode which controls the offshore AC voltage to 1 p.u and the phase angle to 0° at the AC node, whereas the latter was equipped with *Vdc-Q* control mode to control the DC voltage to 1 p.u and maintain zero reactive power exchange at the PCC. The parameters for HVDC submarine copper cables in moderate climate concerning closed laying are presented in Table 5.2.

Table 5.2: Parameters for HVDC submarine copper cables in moderate climate [45].

Area [mm^2]	**Ampacity [A]**	**Resistance at 20°C [Ω/km]**
400	765	0.0439
500	883	0.0351
630	1023	0.0278
800	1175	0.0219
1000	1335	0.0175
1200	1458	0.0146
1400	1594	0.0125
1600	1720	0.0110
1800	1830	0.0097
2000	1953	0.0088
2200	2062	0.0079
2400	2170	0.0073
2600	2275	0.0067
2800	2373	0.0063
3000	2473	0.0058

The ratio of the transformer is 1:1 for an active power capability ranging from 500-1400 MW to provide galvanic isolation between the grid and the DC system. An overview of the complete HVDC model in PowerFactory is showcased in Figure 5.3.

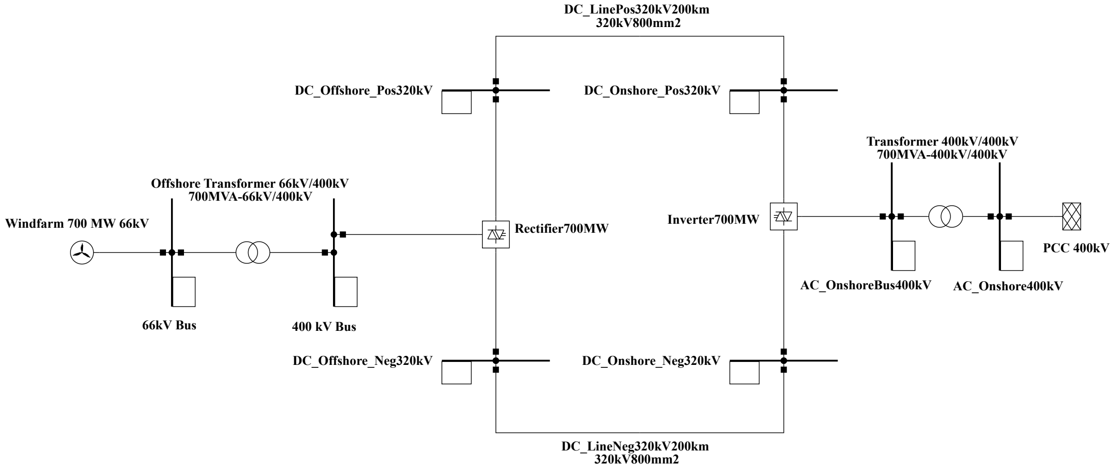

Figure 5.3: Overview of the symmetric monopole, 700 MW, 200 km HVDC model in PowerFactory.

5.2 HVAC models

The HVAC model was constructed for AC transmission with a transmission frequency of 50 Hz. At power levels less than or equal to 800 MW, a transmission voltage of 220 kV was used, while 275 kV was used for power levels above 800 MW. An overview of the two HVAC models is presented in Figures 5.4 and 5.5.

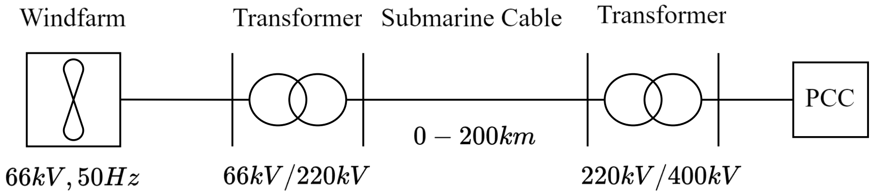

Figure 5.4: HVAC model for an installed active power ranging from 300 MW to 800 MW.

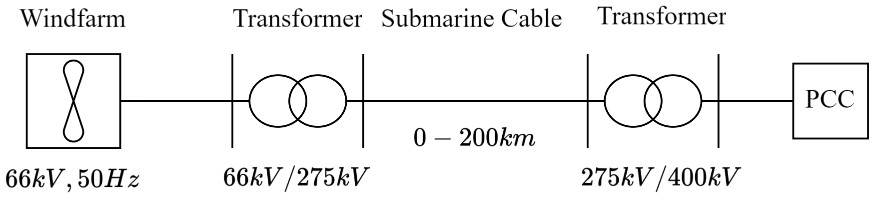

Figure 5.5: HVAC model for an installed active power ranging from 800 MW to 1400 MW.

HVAC subsea copper cables are used for the power transmission and their parameters are showcased in Table 5.3.

Table 5.3: Parameters for HVAC submarine copper cables in moderate climate.

Voltage $[kV]$	**Area** $[mm^2]$	**Ampacity** $[A]$	**Resistance at 20°C** $[\Omega/km]$	**Inductance** $[mH/km]$	**Capacitance** $[\mu F/km]$
220	500	732	0.0489	0.43	0.14
220	630	808	0.0391	0.41	0.17
220	800	879	0.0319	0.41	0.17
220	1000	942	0.0270	0.39	0.19
220	1200	1055	0.0221	0.38	0.21
220	1400	1110	0.0189	0.37	0.22
220	1600	1155	0.0166	0.36	0.23
220	2000	1220	0.0132	0.35	0.24
275	500	732	0.0489	0.43	0.14
275	630	808	0.0391	0.42	0.16
275	800	879	0.0319	0.41	0.17
275	1000	942	0.0270	0.40	0.18
275	1200	1055	0.0221	0.38	0.20
275	1400	1110	0.0189	0.37	0.21
275	1600	1155	0.0166	0.37	0.22
275	2000	1220	0.0132	0.36	0.23

Since data for 275 kV cables was not widely available, the ampacity and the cable parameters were assumed to be the same for corresponding areas between the 220 kV and 275 kV cables. An onshore step-up transformer with an on-load tap-changer (OLTC) equipped is then used to increase the voltage to 400 kV at the PCC. A STATCOM was connected to the low-voltage side of the onshore transformer which controls the reactive power exchange at PCC to zero.

As shunt reactors cost less per MVAr than STATCOMs, shunt reactors were used to minimize the size of the STATCOM between its most capacitive and inductive stages, full- and no production respectively. In this case, the STATCOMs size is minimized when the absolute value of its capacitive and inductive range are equal. A shunt reactor was first placed onshore for short distances since a shunt reactor placed onshore costs less than a shunt reactor placed at the offshore platform. The quality factor of the shunt reactors, the relation between reactance and resistance which affects the losses of the reactor, was set to 300 [46]. As the distance increased, the need for offshore compensation increased in order to maintain an acceptable voltage profile along the line due to the presence of the charging current. Once the voltage range of 0.95-1.05 p.u could not be maintained, only then was a shunt reactor installed at the offshore platform. As the distance increased further, midpoint compensation was required in order to maintain an acceptable voltage profile along the export cable. The voltage level was controlled by controlling the reactive power which is a local phenomenon, hence the voltage level is also a local phenomenon. To simplify and standardize the modeling process, these shunt reactors were kept equal in their MVAr size and changed in steps of 5 MVAr until the size of the STATCOM was minimized. A grid code requirement of $cos(\varphi) = 0.95$ states that a third of the installed active power must be available as reactive support at the PCC. To take height for the impact of the dynamic studies and thereby give a more accurate STATCOM rating, the STATCOM size is set to 40% of the installed active power added to the required STATCOM rating to compensate the export system [44]. The complete HVAC model in PowerFactory is showcased in Figure 5.6 and a flowchart behind the dimensioning of the shunt reactors is shown in Figure 5.7.

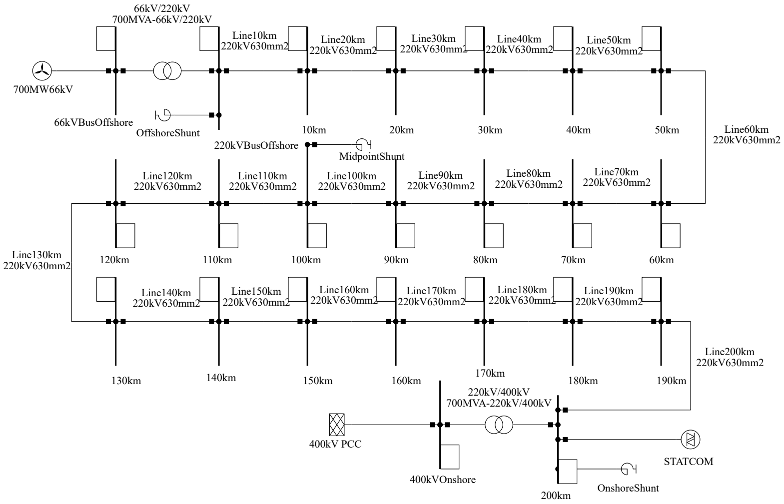

Figure 5.6: Complete model of the 700 MW 200 km HVAC transmission system in PowerFactory.

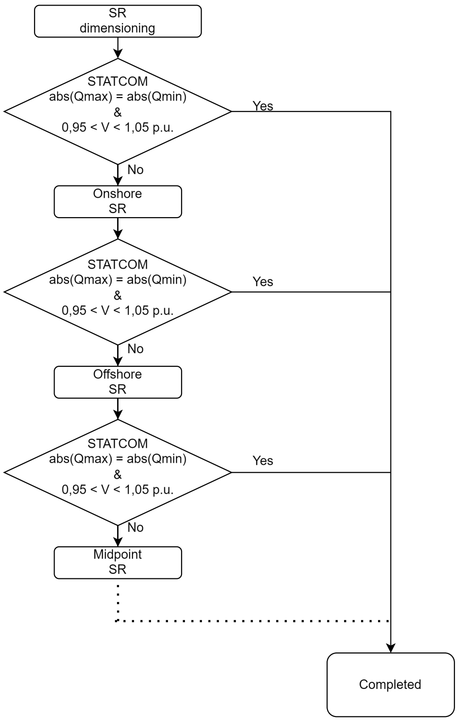

Figure 5.7: Flowchart showcasing the dimensioning of FSR.

5.3 LFAC models

The models for the LFAC were based on AC transmission with two different transmission frequencies. The export transmission frequency was $16\frac{2}{3}$ Hz which is then converted to 50 Hz by an onshore SFC. Similarly to the HVAC systems, the nominal voltage level was assumed to be 220 kV for power levels less or equal to 800 MW as seen in Figure 5.8. For power levels greater than 800 MW, 275 kV were used as seen in Figure 5.9.

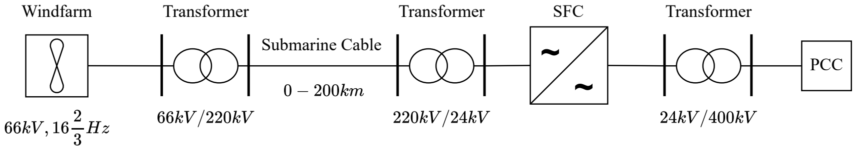

Figure 5.8: LFAC model for an installed active power ranging from 300 MW to 800 MW.

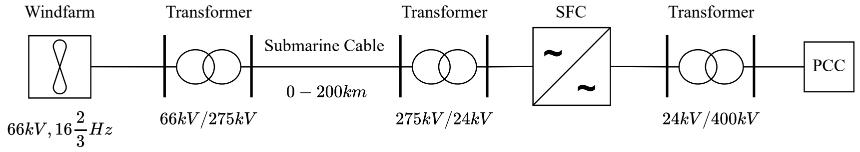

Figure 5.9: LFAC model for an installed active power ranging from 800 MW to 1400 MW.

The setup for the LFAC export system was modeled similarly to the HVAC system with two differences. As the turbines were assumed to be producing at $16\frac{2}{3}$ Hz, there was no need for a frequency conversion at the offshore platform. The second difference compared to the HVAC system was the AC-AC frequency conversion that takes place at the onshore substation.

Firstly the voltage was stepped up from 66 kV to 220/275 kV through an equivalent step-up transformer located on the offshore platform. The power was then transmitted over one or multiple parallel copper subsea cables. As the SFC modules are rated at 24 kV AC, the voltage was first stepped down from 220/275 kV to 24 kV through a step-down transformer connected to the SFC [44]. As the frequency was converted by the SFC, the voltage was then stepped up again from 24 kV to 400 kV before the connection to the PCC. For load-flow calculations, the SFC was modeled as a BtB converter with the converter towards the PCC controlling the reactive power exchange to zero, and the converter towards the export cable controlling the voltage at the onshore 220/275 kV bus to 1 p.u. However, note that the SFC is not a BtB converter, but it can be modeled as such in load-flow simulations. The losses of the SFC were set to 1%. The structure of the LFAC system model is seen in Figure 5.10.

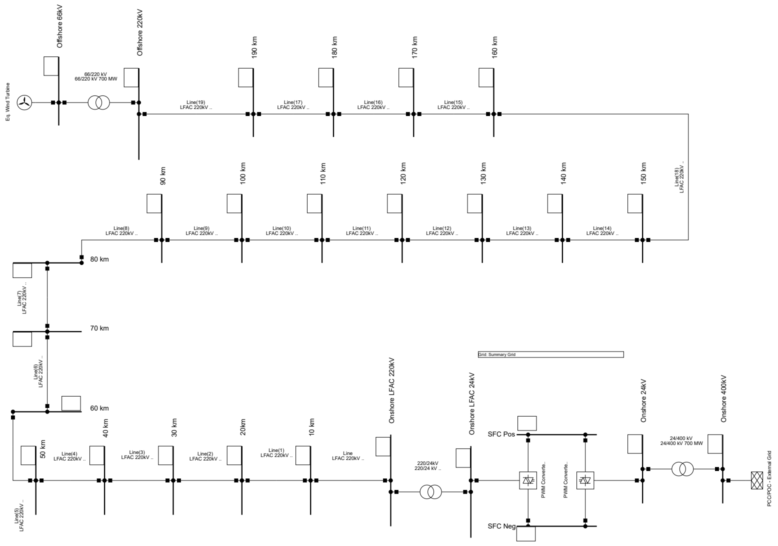

Figure 5.10: Complete model of the 700 MW 200 km LFAC transmission system in PowerFactory.

The cables used for LFAC transmissions were the same as for the HVAC case.

However, there were some differences in the cable ratings. As the transmission frequency was reduced, more current would flow closer to the center of the conductor as the skin effect was reduced. In other words, the effective utilized area is increased which decreases the AC resistance of the cable. Hence, if the same cable is used, the ampacity rating of the cable will be higher compared to the HVAC case. As the documentation found for export cables with a transmission frequency of $16\frac{2}{3}$ Hz was limited, some estimations had to be computed. The ampacity for $16\frac{2}{3}$ Hz and 50 Hz for cables up to 1000 mm^2 were compared. As seen in Figure 5.11, it was found that the average increase in ampacity was roughly 21%. Hence the ampacity for LFAC with a cross-sectional area greater than 1000 mm^2 was estimated by multiplying the HVAC ampacity by the average increase in ampacity. The cable parameters used can be found in Table 5.4.

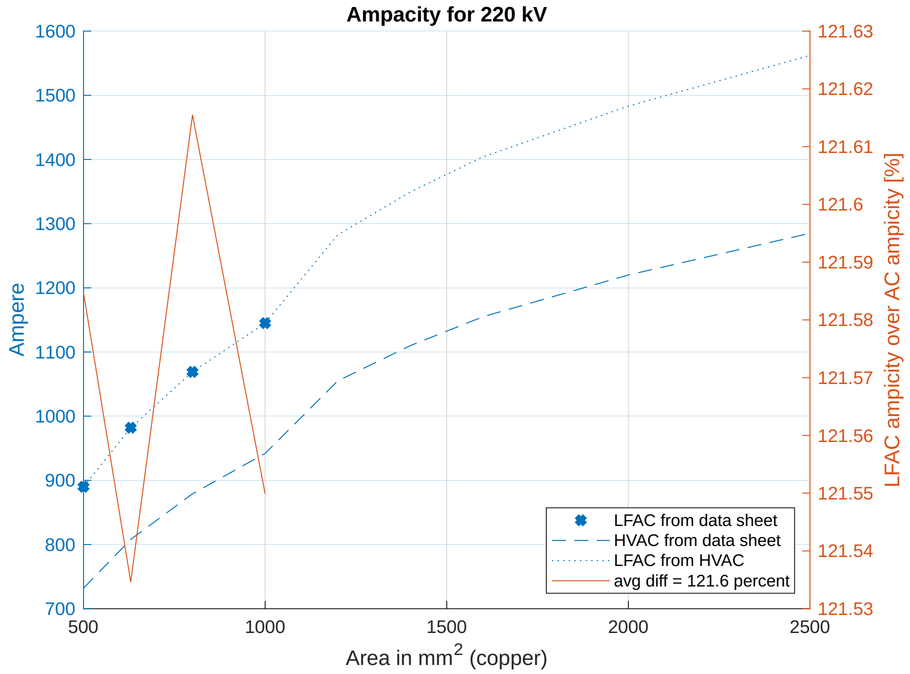

Figure 5.11: Plot showcasing ampacity estimation for LFAC export cables as a function of the cross-sectional area.

Table 5.4: Parameters for LFAC submarine copper cables in moderate climate.

Voltage $[kV]$	**Area** $[mm^2]$	**Ampacity** $[A]$	**Resistance at 20°C** $[\Omega/km]$	**Inductance** $[mH/km]$	**Capacitance** $[\mu F/km]$
220	500	890	0.0324	0.43	0.14
220	630	982	0.0270	0.41	0.17
220	800	1069	0.0211	0.41	0.17
220	1000	1145	0.0179	0.39	0.19
220	1200	1283	0.0146	0.38	0.21
220	1400	1349	0.0125	0.37	0.22
220	1600	1404	0.0110	0.36	0.23
220	2000	1483	0.0087	0.35	0.24
275	500	890	0.0324	0.43	0.14
275	630	982	0.0270	0.42	0.16
275	800	1069	0.0211	0.41	0.17
275	1000	1145	0.0179	0.40	0.18
275	1200	1283	0.0146	0.38	0.20
275	1400	1349	0.0125	0.37	0.21
275	1600	1404	0.0110	0.37	0.22
275	2000	1483	0.0087	0.36	0.23

6

Economic modeling

This chapter presents the CAPEX and OPEX costs associated with each transmission configuration as well as the economical modeling approach that was performed in Python.

6.1 HVDC costs

All the costs associated with the HVDC export cables were gathered from [38] and its costs are showcased in Table 6.1.

Table 6.1: CAPEX and OPEX costs for the HVDC export cables including burying.

Export cables	CAPEX [$/km]	OPEX [% of CAPEX]	Source
630mm^2 ±150 kV	363 250	2.50	[38][47]
1000mm^2 ±150 kV	431 000	2.50	[38][47]
1600mm^2 ±150 kV	541 500	2.50	[38][47]
630mm^2 ±320 kV	533 750	2.50	[38][47]
800mm^2 ±320 kV	565 000	2.50	[38][47]
1000mm^2 ±320 kV	601 500	2.50	[38][47]
1200mm^2 ±320 kV	638 500	2.50	[38][47]
1400mm^2 ±320 kV	644 525	2.50	[38][47]
1600mm^2 ±320 kV	712 000	2.50	[38][47]
2000mm^2 ±320 kV	785 500	2.50	[38][47]
2200mm^2 ±320 kV	823 850	2.50	[38][47]
2400mm^2 ±320 kV	859 100	2.50	[38][47]

The simulation contains cables rated for a voltage of ±150 kV and ±320 kV, which differ in cost due to a difference in the required insulation rating. The OPEX costs were estimated as a percentage of the CAPEX in accordance with the ten-year network development plan developed by ENTSO-E [47]. It is important to note that the HVDC transmission system was modeled as a symmetric monopole and these costs are given per km of cable. This means that these costs must be multiplied by a factor of two since this configuration has two export cables, one for each DC pole.

The CAPEX cost for the HVDC converter is expressed per installed MW and was gathered from the cost set data 2 in [47], which is an average cost developed by the German TSO TenneT and the European TSO ENTSO-E. Costs for the HVDC platform were estimated from [48] where the cost for the topside and jacket are specified depending on the installed active power. These costs were averaged in order to linearize the cost of the platform per installed megawatt. Costs for the transformers were gathered from [49], which is a network development plan for offshore wind approved by BNetzA. The cost for the transformer was then averaged in order to provide a generic cost for the transformers. The OPEX costs were estimated as a percentage of the CAPEX cost in accordance with [50], and their costs are specified in Table 6.2.

Table 6.2: CAPEX and OPEX cost for the HVDC transmission system.

Component	**CAPEX [$/MW]**	**OPEX [% of CAPEX]**	**Source**
OSS Converter	299 750	2	[47][50]
Transformer	19 620	0.15	[49][50]
Platform	484 290	2	[48][50]
OnSS Converter	299 750	0.7	[47][50]

6.2 HVAC costs

Costs associated with the HVAC export cables were gathered from [38] and are given per km. It is important to note these costs have to be multiplied by the number of parallel cables if parallel cables are needed to transmit the active power. OPEX of the cables was estimated as a percentage of the CAPEX in line with the ten-year network development plan for offshore wind developed by ENTSO-E [47]. The cost associated with the HVAC can be found in Table 6.3.

Table 6.3: CAPEX and OPEX costs for the HVAC export cables including burying.

Export cables	**CAPEX [$/km]**	**OPEX [% of CAPEX]**	**Source**
500mm^2 220/275kV	1 035 050	2.50	[38][47]
630mm^2 220/275kV	1 079 500	2.50	[38][47]
800mm^2 220/275kV	1 274 000	2.50	[38][47]
1000mm^2 220/275kV	1 437 000	2.50	[38][47]
1200mm^2 220/275kV	1 600 000	2.50	[38][47]
1400mm^2 220/275kV	1 763 000	2.50	[38][47]
1600mm^2 220/275kV	1 926 000	2.50	[38][47]
2000mm^2 220/275kV	2 251 000	2.50	[38][47]

Costs associated with the offshore platform were gathered from [24] and it includes switchgear, lightning protection, facilities, and the steel structure. Shunt reactors had to be implemented offshore at a certain distance which requires space on the offshore platform. The cost of the platform was then increased by the required MVAr of the shunt reactors in order to account for the required space needed on the platform. The cost for the onshore substation was collected from [24], which includes buildings, access, security, and monitoring systems. Numerous electrical components were similar in specification to the offshore substation but constraints such as weight and space are not as critical onshore. The cost of the STATCOM, the onshore shunt reactor, and the transformer was then added to the total cost of the onshore substation since space and weight are not as essential onshore. OPEX for the HVAC components was collected from [50] and is given as a percentage of CAPEX. Costs for the components associated with the HVAC configuration are showcased in Table 6.4.

Table 6.4: CAPEX and OPEX cost for the HVAC transmission system.

Component	**CAPEX [$/MW]**	**OPEX [% of CAPEX]**	**Source**
Platform	203 200	2	[24][50]
Midpoint Platform	203 200	2	[47][50]
Transformer	19 620	0.15	[49][50]
SR Offshore	28 340	0.15	[49][50]
SR Midpoint	28 340	0.15	[49][50]
SR Onshore	28 340	0.15	[49][50]
STATCOM	125 760	0.7	[51][50]
OnSS	38 100	0.7	[24][50]

6.3 LFAC costs

As costs for low-frequency components for high-power applications were not widely available, some estimations had to be made. Firstly, since the same cables were assumed to be used for LFAC and HVAC respectively, the costs are equal as well. Then the per unit cost of the SFC was assumed to be the same as that of an onshore VSC-HVDC converter. The size of the low-frequency transformer increases with a decreased frequency, which increases the materials used and subsequently the total cost. Based on the transformer materials percentage costs of the transformer's total cost, the cost of materials that depends on the frequency can be re-scaled such that the cost is adapted to the desired frequency. A transformer materials percentage cost of the transformer total cost is presented in Table 6.5.

Table 6.5: A transformer materials percentage cost of the total transformer cost [52].

Material	**Percentage of total cost [%]**
Carbon steel	16.4
Fabricated parts	15
Insulation	14.1
Magnetic steel	32.5
Windings	22

As the costs are known, the cost of a transformer for a given frequency can be estimated as in Equation (6.1)

$$C_{Tr} = \frac{0.325f_r + 0.22f_r + 0.164\sqrt[3]{f_r^2}}{0.325 + 0.22 + 0.164} \cdot C_{Tr50Hz} = 2.7872 \cdot C_{Tr50Hz} \tag{6.1}$$

where C_{Tr} is the cost of the transformer with the new frequency, C_{Tr50Hz} is the cost of a 50 Hz transformer, and f_r is the ratio between 50 Hz and the desired frequency, $f_r = \frac{f_{nominal}}{f_{new}}$. The equation essentially computes a ratio between the 50 Hz transformer and the transformer for the new frequency. Therefore if $16\frac{2}{3}$ Hz is analyzed, the cost of the transformer is 2.7872 times the 50 Hz transformer [52].

The same procedure can then be applied to the cost of the offshore platform. From [52], the weight of the transformer is assumed to be two-thirds of the capacity of the platform. Then the cost of the offshore platform can be estimated as in Equation (6.2)

$$C_{SS} = 2530 + 88.7P_{rated}\left(\frac{1}{3} + \frac{2}{3}f_r\right) \tag{6.2}$$

where C_{SS} is the cost of the LFAC platform in k€, and P_{rated} is the installed active power.

To estimate the cost ratio between the LFAC platform and the HVAC platform, Equation (6.3) was used. In the equation, the platform cost in \$ for each power level is calculated for both HVAC and LFAC and thereafter normalized with the installed active power such that a cost per MVA price is obtained. Then the average cost per MVA is averaged such that the average cost per MVA for all power levels is obtained. Lastly, the cost per MVA ratio between LFAC and HVAC is calculated

$$\text{Platform cost ratio} = \frac{\text{LFAC}}{\text{HVAC}} = \frac{\dfrac{\sum_{i=1}^{12} \dfrac{\left(2530 + 88.7P_{rated}(i)(\frac{1}{3} + \frac{2}{3}f_r)\right) \cdot C_{€\to\$}}{P_{rated}(i)}}{12}}{\dfrac{\sum_{i=1}^{12} \dfrac{\left(2530 + 88.7P_{rated}(i)(\frac{1}{3} + \frac{2}{3}f_{r,50Hz})\right) \cdot C_{€\to\$}}{P_{rated}(i)}}{12}}$$

$$\rightarrow \text{Platform cost ratio} = 2.28 \tag{6.3}$$

where $C_{€\to\$}$ is the conversion rate from € to \$, and $P_{rated}(i)$ is the installed active power which is equal to $i \cdot 100 + 200$ MW. As the transformer and platform cost ratios were determined, the rest of the costs were gathered. CAPEX and OPEX for the LFAC components are presented in Table 6.6.

Table 6.6: CAPEX and OPEX cost for the LFAC transmission system.

Component	**CAPEX [$/MW]**	**OPEX [% of CAPEX]**	**Source**
SFC	299 750	0.7	[50]
Transformer 16 2/3 Hz	54 685	0.15	[50]
Transformer 50 Hz	19 620	0.15	[50]
Platform	463 296	2	[50]
Substation	38 100	1.5	[50]

6.4 Economic modeling in Python

The total system losses from the load-flow analysis were used as input for the economic analysis and the ratings were used as input for the evaluation of CAPEX and OPEX. As the required data was gathered into two separate Excel files, the data was converted into CSV files for data processing. As Figure 6.1 indicates, a python *jupyter notebook* was used for the economic modeling. Firstly the CSV files containing electrical data and cost data were imported and converted into data frames. As the files were imported, the electrical data were matched with its corresponding costs such that the capital expenditures of the system could be retrieved. This part of the code also distributes the corresponding OPEX related to the electrical system and installation. As the expenditures were determined, the LCOE could be calculated for each configuration. For all cases, the life span was assumed to be 27 years, 100% availability, and the bond rate was set to 6% [24]. The LCOE was calculated in a for-loop where the annual energy produced is based on the installed active power and the losses from the electrical data. Estimation of the capacity factor was determined from historical data gathered from various countries around the world, the capacity factor averages between 39-43 % according to historical data [53]. A capacity factor of 40% was selected when determining the LCOE for each configuration.

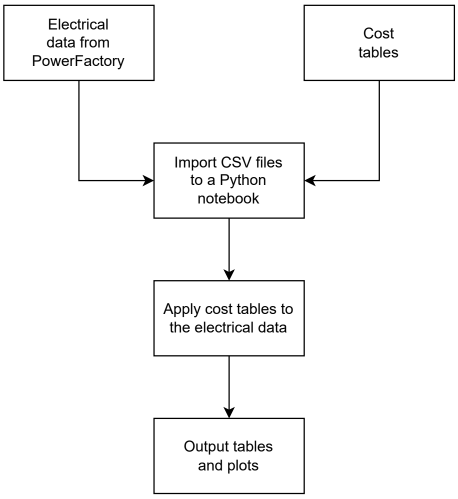

Figure 6.1: Principles of economic modeling in Python.

The initial resolution of the data was 12 power levels and 10 distances, every 100

MW and 20 km, resulting in 120 data points. To increase the resolution, and thereby be able to present a more accurate break-even point between the topologies, three-dimensional interpolation was implemented between neighboring data points. The new data frame contained data for every 10 MW and every other km. Hence the increased resolution based on the actual 120 data points became 111 power levels and 91 distances, resulting in 10101 data points.

7

Electrical results

This chapter presents the electrical findings from the dimensioning and the performed load-flow studies.

7.1 HVDC

Results from the load-flow simulations are showcased in Figure 7.1 where Figure 7.1a shows the losses in MW and Figure 7.1b shows the losses as a percentage of the installed active power.

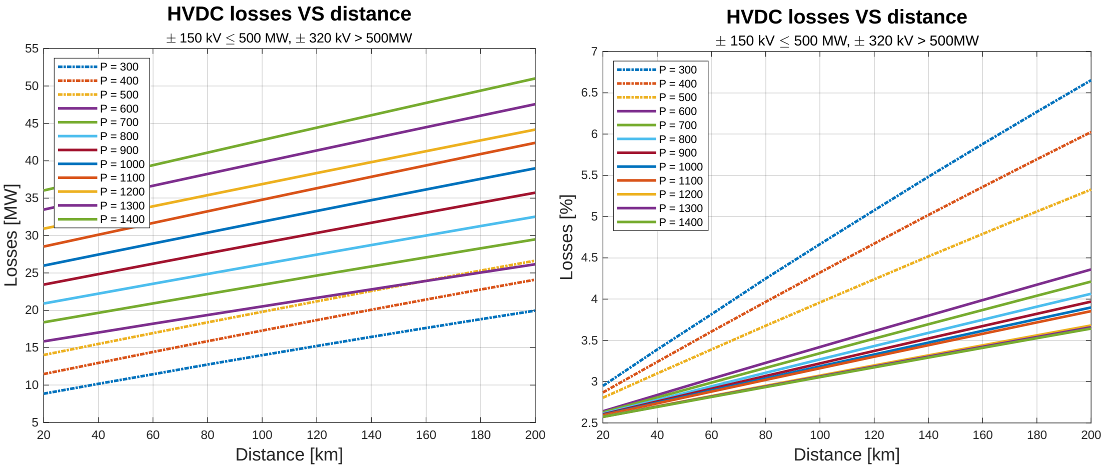

(a) Plot presenting active power losses in MW against distance for each power level.

(b) Plot presenting active power losses normalized by installed active power against distance for each power level.

Figure 7.1: Plots presenting active power losses vs. distance for each power level for HVDC.

The required size of the cable was dependent on the current flowing through each DC pole. Due to DC transmission, the magnitude of the current almost remains the same as no charging currents are present. Thus, the losses increase linearly with the distance for each power level respectively, as the cable resistance increases proportionally with the distance. This means that the same cross-sectional area of the cable can be used for all distances for each studied power level. The dashed lines in Figure 7.1 show the 300 MW, 400 MW, and 500 MW cases. The derivative for these three cases is vastly greater compared to the other cases. This is because the transmission voltage is ±150 kV while the other ones had a transmission voltage of ±320 kV. A lower transmission voltage results in a greater current and the losses are proportional to the current squared.

7.2 HVAC

The electrical results from the power system modeling of the HVAC export system will be presented in this section.

7.2.1 Losses

In Figure 7.2a the losses of the HVAC system are presented in MW, and in Figure 7.2b the losses are normalized by the installed active power.

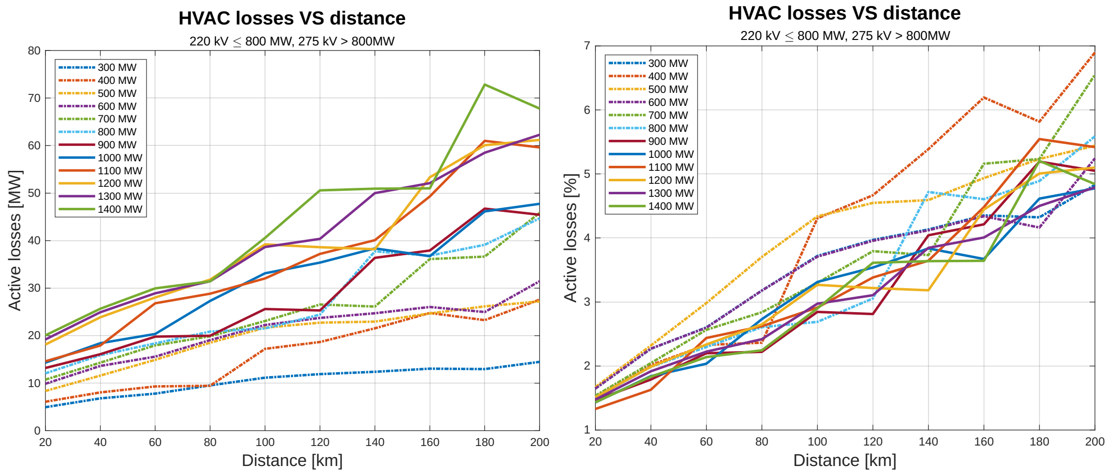

(a) Plot presenting active power losses in MW against distance for each power level.

(b) Plot presenting active power losses normalized by installed active power against distance for each power level.

Figure 7.2: Plots presenting active power losses vs. distance for each power level for HVAC.

As seen in Figure 7.2, as the distance increased the active power losses increased with the distance because the resistance of the cable increases with increased distance. The reason for the non-linear behavior is mainly related to the area and number of parallel export cables used. This is observed in the loss difference for 1400 MW between 140 km and 160 km. For 140 km there are four parallel cables with a cross-sectional area of 1200 mm^2, and for 160 km there are four parallel cables with a cross-sectional area of 2000 mm^2. In that case, the reduction of resistance due to the increased cross-sectional area is greater than the resistance added for the 20 additional km. Hence the losses are slightly reduced in this case. Also, the charging currents flowing through the cable contribute to active power losses. The first type of loss related to the charging currents was power factor and voltage correction. As the charging currents increased, the need for reactive power compensation increased which resulted in increased losses since the losses of the shunt reactors can be in the

MW range. Secondly, as the charging currents increase, the higher the active power losses become due to an increase in the apparent current flow through the cable.

7.2.2 Reactive power compensation

The total shunt reactor sizes required to minimize the STATCOM and maintain voltage levels across the cable within limits are presented in Figure 7.3. The dotted lines represent configurations with a nominal export system voltage of 220 kV, and the solid lines represent configurations with a nominal system voltage of 275 kV.

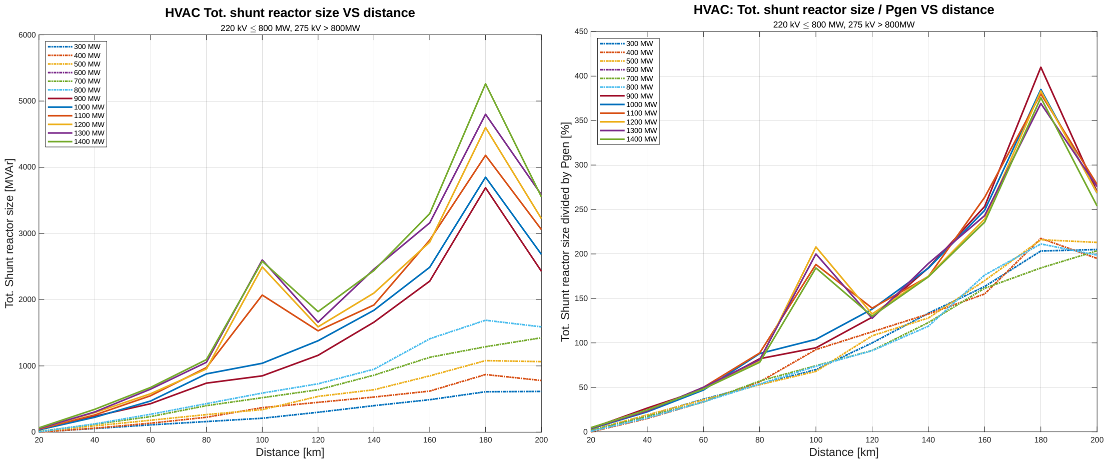

(a) Shunt reactor size in MVAr vs. distance.

(b) Shunt reactor size over installed active power vs. distance.

Figure 7.3: Combined shunt reactor size vs. distance.

Figure 7.3a presents the sum of Q_{shunt}, and Figure 7.3b presents the sum of Q_{shunt} in MVAr normalized with respect to the installed active power of the wind farm. As seen in the figure, for certain distances, the required installed shunt reactor capacity was upwards of 400 % of the installed active power. However, at distances below 80 - 100 km for 275 kV systems, the required installed shunt reactor capacity was below 100 % of the installed active power. For 220 kV, the distance at which the installed shunt reactor capacity was below 100 % was roughly 100 - 120 km. As the charging current in the cable is equal to the voltage multiplied by the admittance, the reactive power generated is equal to the admittance multiplied by the voltage squared. Therefore, an increased voltage leads to an increased need for compensation if the same cable is considered. This can also be seen in Figure 7.3 as the derivative of the 275 kV cases was slightly higher than compared to 220 kV. At 100 and 180 km, some outliers can be observed. At these points, the required size of the FSRs increased more than expected. This can be explained by the method used for the placement of the FSRs. For 100 km, the voltage limit was not violated for all models. Therefore, if the voltage level was not violated, only onshore reactive power compensation was installed. Otherwise, onshore and offshore compensation was installed.

In Figure 7.4, the size of the shunt reactor used at each location is presented for the minimum and maximum power levels.

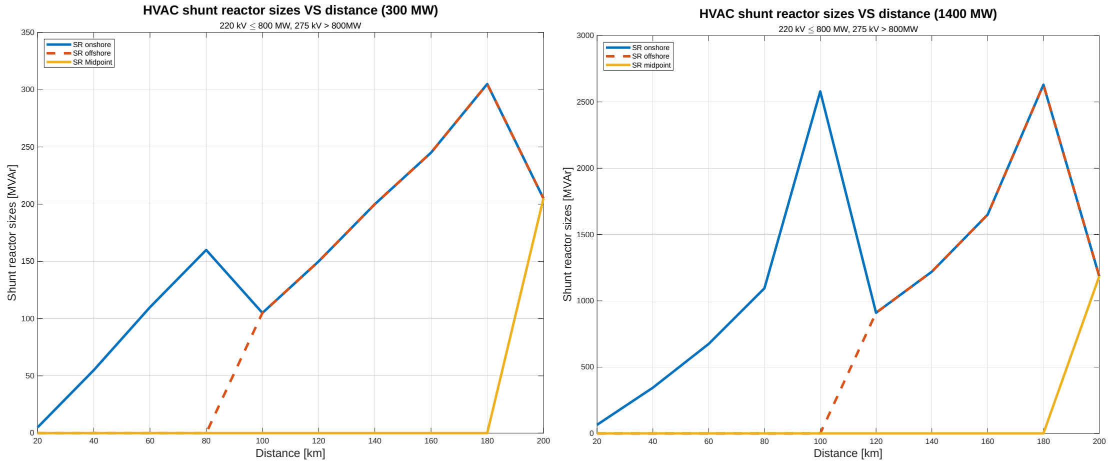

(a) P = 300 MW.

(b) P = 1400 MW.

Figure 7.4: Shunt reactor size distribution vs distance. P is the installed active power of the wind farm.

The results for all power levels can be found in Appendix A. From the figures, two points of interest can be found. The first point of interest is at 80 - 100 km. For export cables longer than 80 - 100 km, an onshore shunt reactor was not enough to maintain the voltage within its defined limits. Therefore, for export cables longer than 80 - 100 km, an offshore shunt reactor is needed. The next point of interest is located at 180 km. After 180 km, the voltage along the cable could not be maintained using only onshore and offshore compensation. Therefore, for cable lengths exceeding 180 km, midpoint compensation is required to maintain the voltage profile within its set limits.

7.2.3 Voltage profile and loading level

As seen in Figure 7.5, the voltage profile and the loading were highly dependent on the placement of the shunt reactors. The placement of the shunt reactor was crucial since a reactive current will be drawn at the point of its connection which affects the voltage at that point's vicinity.

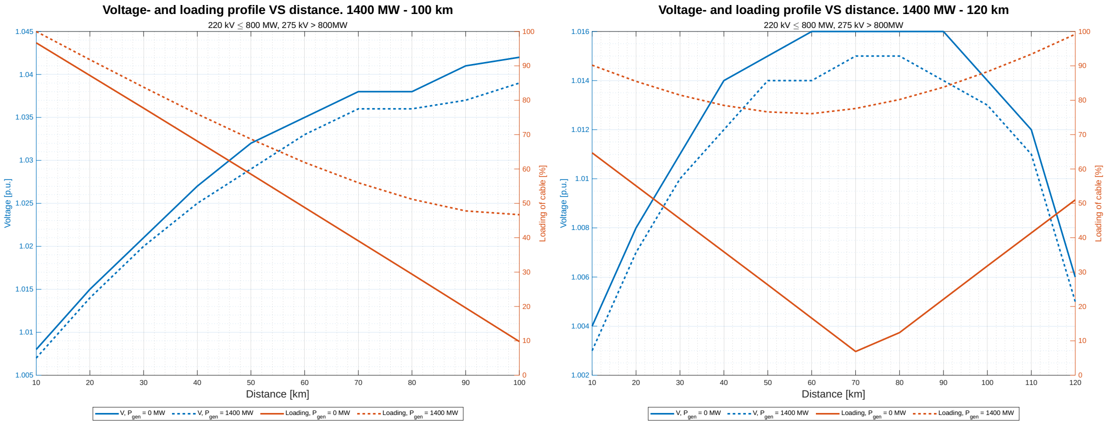

(a) 100 km: Onshore FSR. ***(b)*** 120 km: Onshore and offshore FSR.

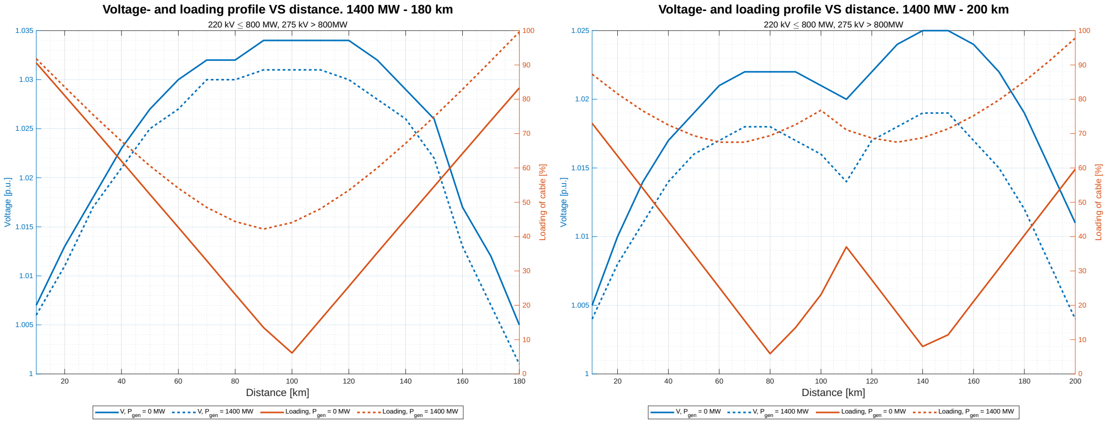

(c) 180 km: Onshore and offshore FSR. ***(d)*** 200km: Onshore, offshore, and midpoint FSR.

Figure 7.5: Voltage profile and loading level dependency on distance and placement of SR for the 1400 MW case. Dotted lines correspond to full production and solid lines correspond to zero production.

In Figure 7.5a the voltage and loading profile can be seen for a connection with a 100 km long export cable. By studying the no-production loading curve, it can be seen that the cable is only compensated by an onshore shunt reactor and a STATCOM due to the loading levels linear decrease from the onshore connection which would also be the case if compensation was not implemented. The reason for the decreased loading level along the cable is that the supplied inductive current is canceled more and more along the cable due to its capacitive nature. During full production, the loading was slightly increased along the cable, mainly towards its endpoint. This can be explained by the presence of the generated active power that flows through the cable. The behavior of the voltage profile along the cable is in that case the opposite of the loading, especially during no production. The reason is that the Ferranti effect becomes present. During no production and with the cable still energized, capacitive currents are produced. Therefore, the voltage of the capacitive effect is added to the onshore voltage.

In Figure 7.5b, the voltage and loading profile can be seen for a connection with a 120 km long export cable. For no-production conditions, it is observed that the loading reaches a minimum roughly towards the middle of the cable. This phenomenon can be explained due to the installation of offshore reactors, which was necessary to maintain the voltage profile within limits. As expected, both onshore and offshore reactors absorb the capacitive reactive power generated by the cable, which is why the maximum loading occurs at the endpoints of the cable. Due to the reduced apparent current close to the onshore bus compared to the case at 100 km with only an onshore FSR, the number of parallel cables and the cross-sectional area could be reduced. A direct impact of the placement of the shunt reactors was the magnitude of the voltage. Along the cable, the voltage could be kept close to 1 p.u, especially at the endpoints.

In Figures 7.5c and 7.5d, the distance of the export cable is 180 km and 200 km respectively. Since mid-compensation is not used for the 180 km case, the profile is similar to that of the 120 km case. For 200 km, the voltage could not be maintained with only onshore and offshore reactors, hence mid-compensation was installed. As seen in Figure 7.5d, the loading reached its local maximum at the point where the shunt reactors were installed due to the reactive currents. Vice versa, the voltage reached its local minimum at the location of the shunt reactors. The implementation of mid-compensation in this case allowed for an increase of the transmittable distance. At the same time, the number of parallel cables and their cross-sectional area could be reduced without any limits being violated compared to the 180 km case.

7.3 LFAC

Figure 7.6 presents the results computed from the load-flow computations. Figure 7.6a presents the total active power losses and Figure 7.6b presents the losses normalized by the installed active power as a percentage value. As seen in the figures, the losses increase linearly as the distance is increased. This is related to that reactive power compensation by shunt reactors was not required to keep the voltage within its limits. Hence, as the distance was increased, and the same cross-sectional area of the export cable was kept, the only added impedance was that of the increased cable length. Therefore the losses increased linearly as the distance increased. A difference in the derivative of the losses between the different power levels can be seen in Figure 7.6b. It was related to that for power levels over 800 MW, where the transmission voltage was increased to 275 kV. As the voltage was increased, the current decreased which led to a reduced derivative of the active power losses since it scales with the current squared.

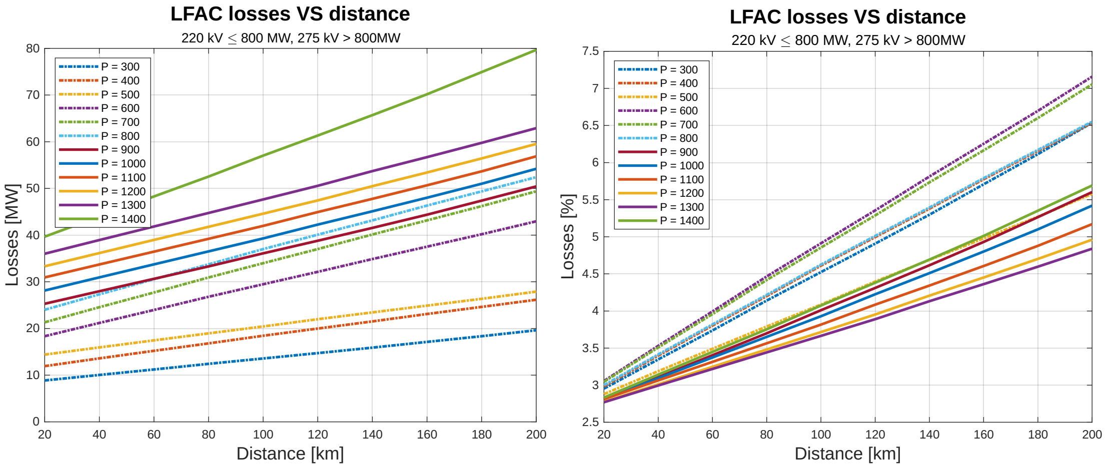

(a) Plot presenting active power losses in MW against distance for each power level.

(b) Plot presenting active power losses normalized by installed active power against distance for each power level.

Figure 7.6: Plots presenting active power losses vs. distance for each power level for LFAC.

For LFAC, the charging current could drastically be reduced due to the reduced transmission frequency. As previously mentioned, there was not any need for shunt reactors. However, since the SFC controls the voltage level of the onshore high voltage bus to 1 p.u, it did provide reactive support. Therefore the loading and voltage profile of the LFAC configurations behave similarly to the HVAC case with just onshore shunt reactors. By studying the loading in Figure 7.7, it can be seen that when the wind farm is not producing any active power, the charging currents were greatly reduced compared to the similar HVAC case. Therefore, the voltage increase along the cable at no production is not as noticeable due to the reduced charging current.

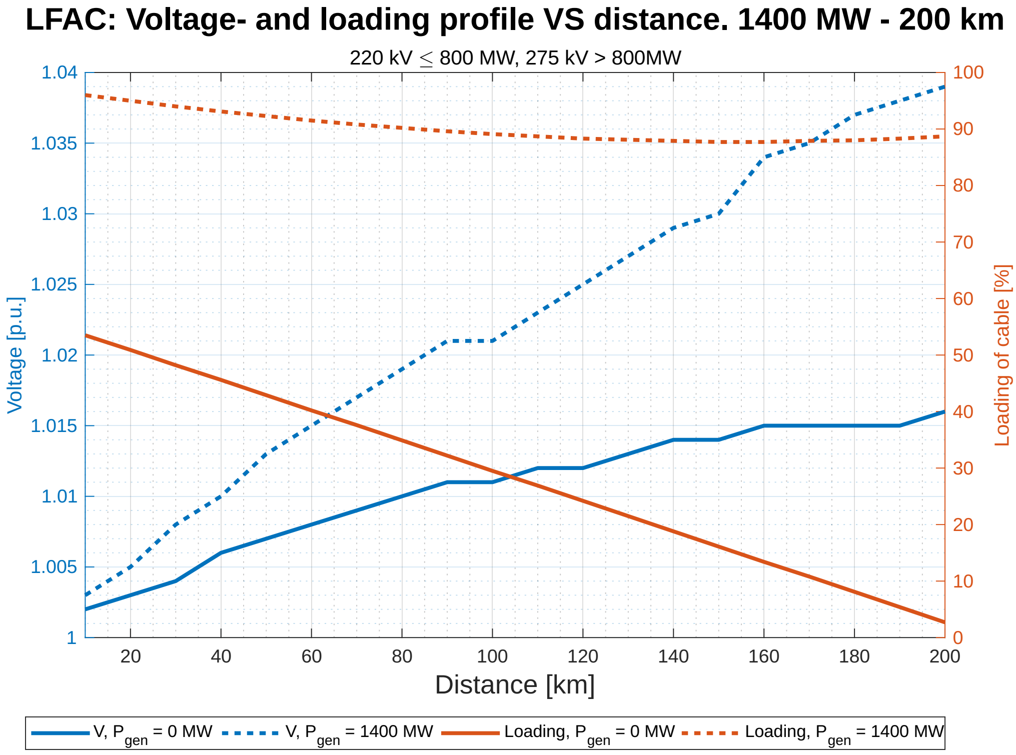

Figure 7.7: Voltage profile and loading dependency on distance and placement of SR for the 1400 MW case. Dotted lines correspond to full production and solid lines correspond to zero production.

8

Economic results

This chapter presents the performed CAPEX and LCOE analysis to determine the break-even distance between the export system topologies. This chapter lastly presents a sensitivity analysis of the cost of the SFC for the LFAC system and how that affects the break-even point.

8.1 CAPEX analysis

Firstly the investment costs of the systems were evaluated. The costs for the corresponding components and their sizes were applied to each system in the Python script. Figure 8.1 presents the CAPEX for each configuration with 300, 800, and 1400 MW of installed active power.

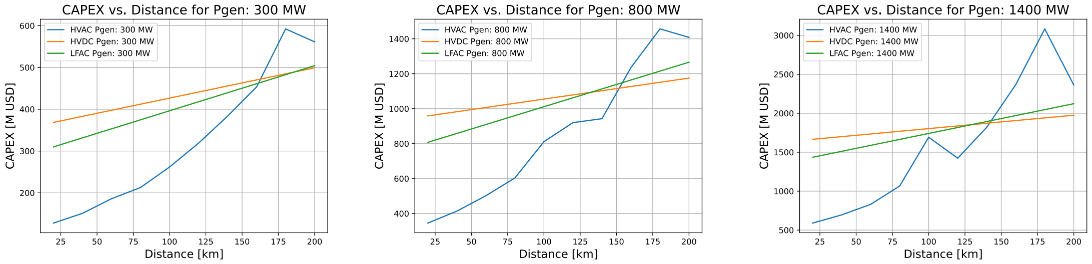

(a) Plot presenting the CAPEX for 300 MW installed active power.

(b) Plot presenting the CAPEX for 800 MW installed active power.

(c) Plot presenting the CAPEX for 1400 MW installed active power.

Figure 8.1: Plots presenting CAPEX vs. distance for 300, 800, 1400 MW of installed active power.

As seen in the plots, HVAC has by far the lowest cost for short distances while HVDC is the most expensive, and LFAC is somewhere in between. This was expected since the converters dominate the cost at shorter distances. As the distance increases, the charging current, and thereby the required compensation for HVAC mainly drives up the required number of parallel cables and their cross-sectional area. Subsequently, this results in an exponential growth of the cost as well.

For some HVAC systems, offshore shunt compensation was not required until 120 km resulting in a local maximum of the CAPEX which is not the cheapest alternative due to the choice of methodology. If offshore compensation were to be introduced at

100 km instead, the number of parallel cables could be reduced resulting in a lower cost even though offshore compensation is added. Hence the cost for these configurations must be in between the cost at 80 km where offshore fixed shunt reactors were not used, and 120 km where offshore compensation was used. Therefore the cost at 100 km if offshore compensation was implemented was estimated by interpolating between 80 and 120 km. An example of the performed interpolation can be seen in Figure 8.2. All the plots presenting the CAPEX analysis can be found in Appendix B.

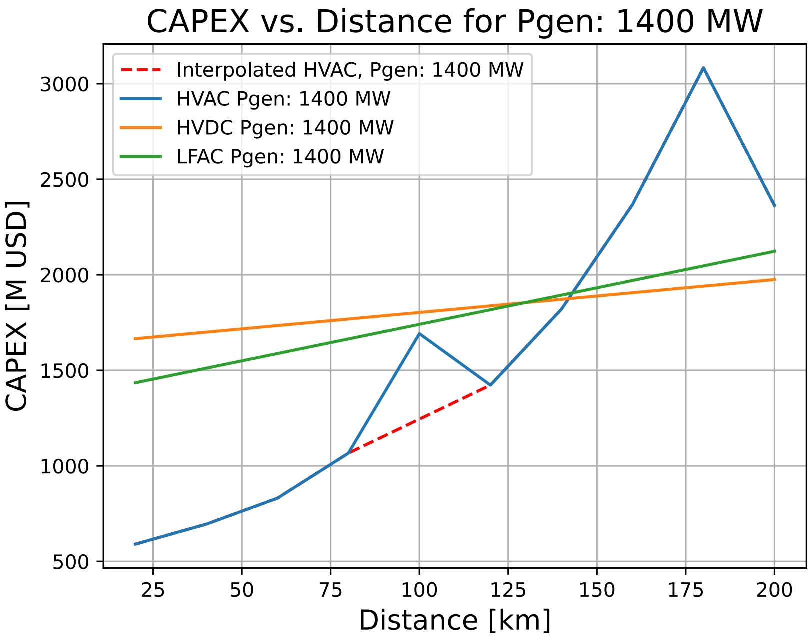

Figure 8.2: Plot presenting the performed interpolation between 80 - 120 km for some HVAC configurations.

As the CAPEX was calculated for all the configurations, the break-even point based on CAPEX was determined. Figures 8.3 and 8.4 presents the export system with the lowest cost based on power level and distance where each color represents an export system topology. Figure 8.3 presents the CAPEX analysis without interpolation, and Figure 8.4 presents the CAPEX analysis where some power levels for HVAC has been interpolated between 80 - 100 km.

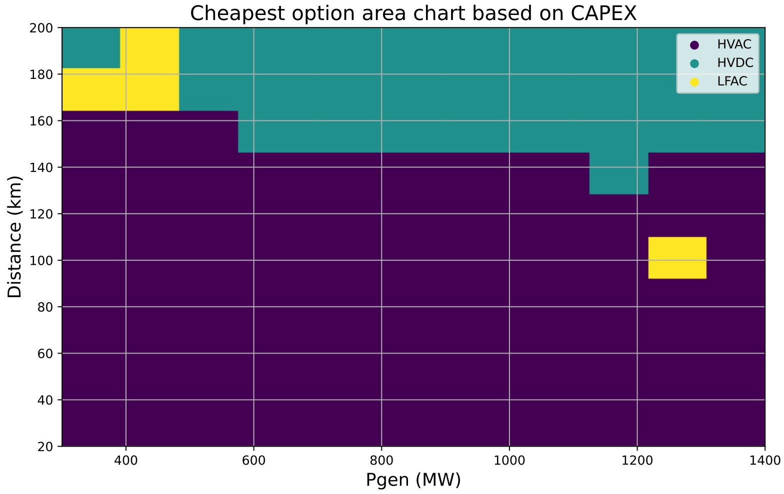

Figure 8.3: Area chart presenting the cheapest export system based on CAPEX.

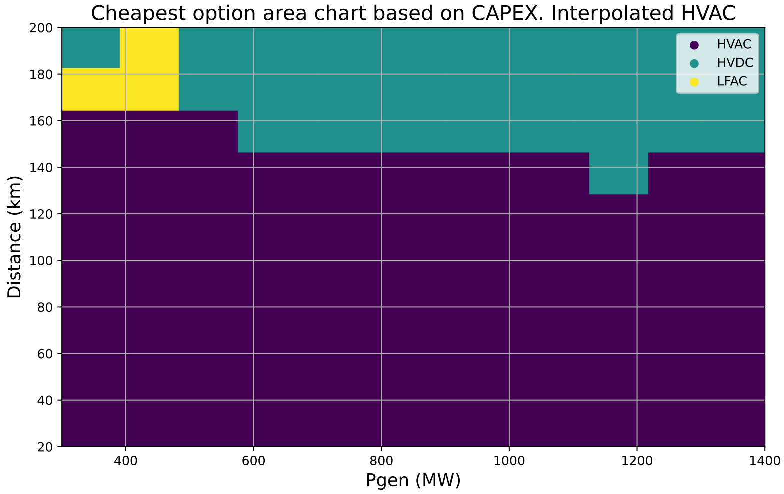

Figure 8.4: Area chart presenting the cheapest export system based on CAPEX with the HVAC cost interpolated at 100 km for some configurations.

8.1.1 Increased resolution of the CAPEX break-even distance

As seen in Figure 8.3 and Figure 8.4, the resolution of the plot is equal to the number of models per configuration. The nominal resolution for 12 power levels and 10 distances is therefore 120 points. To increase the accuracy of the break-even distance, interpolation in three dimensions was performed. The CAPEX was interpolated with respect to both distance and power level to increase the resolution for each topology from 120 points to 10101 points. The increased resolution results in the possibility of finding the break-even distance for every tenth MW of every other km. An area chart with the increased resolution presenting the cheapest option based on CAPEX for a given distance and power level can be found in Figure 8.5.

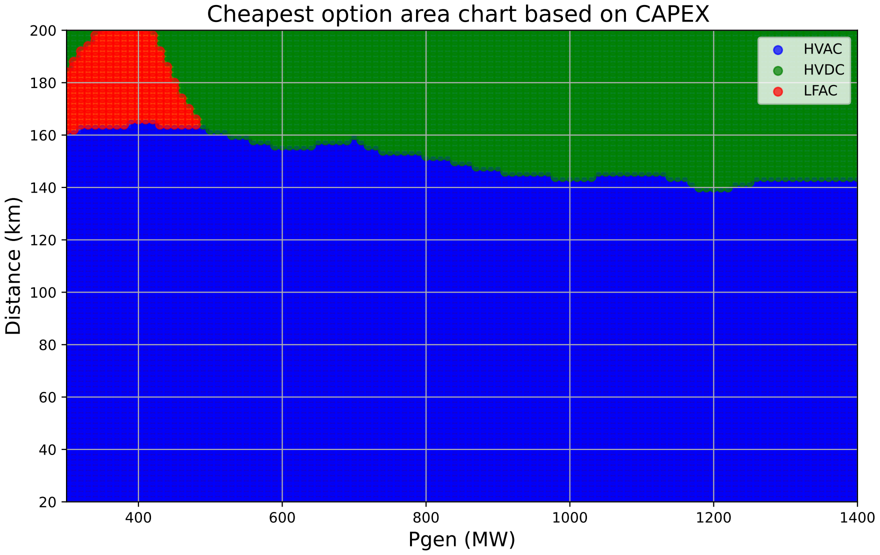

Figure 8.5: Area chart presenting the cheapest export system based on CAPEX with increased resolution.

8.2 LCOE analysis

As the CAPEX analysis was completed, the LCOE analysis could be performed. The results of the LCOE analysis were based on CAPEX and OPEX where some HVAC configurations were interpolated at 100 km. The LCOE analysis considers a discount rate of 6% and an economic lifetime of 27 years. Figure 8.6 presents the results of the LCOE analysis. All the plots presenting the LCOE analysis for every 100 MW can be found in Appendix C.

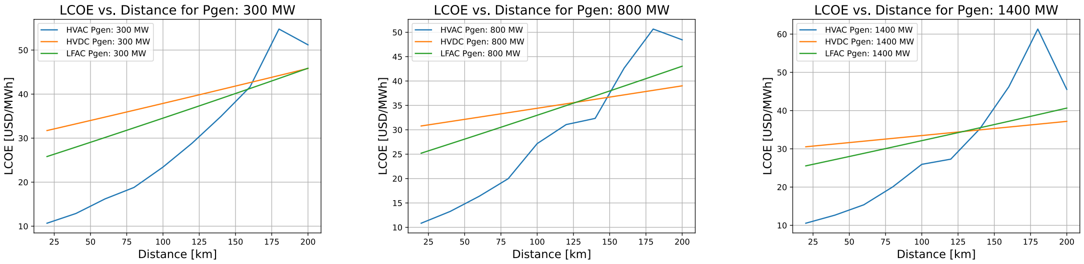

(a) Plot presenting the LCOE for 300 MW installed active power.

(b) Plot presenting the LCOE for 800 MW installed active power.

(c) Plot presenting the LCOE for 1400 MW installed active power.

Figure 8.6: Plots presenting LCOE vs. distance for 300, 800, 1400 MW of installed active power.

Then the break-even distance-based LCOE could be determined. The area chart in Figure 8.7 presents the configuration with the lowest LCOE for a given power level and distance where each color represents an export system.

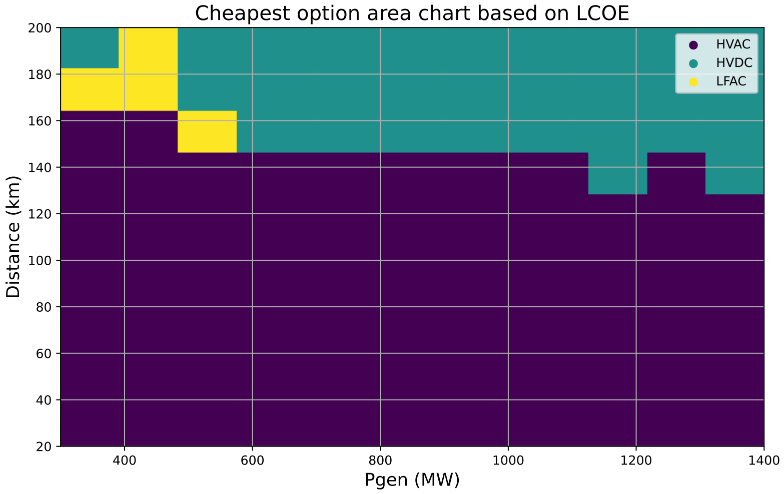

Figure 8.7: Area chart presenting the cheapest export system based on LCOE.

8.2.1 Increased resolution of the LCOE break-even distance

The resolution of the LCOE analysis was also increased based on three-dimensional interpolation. The difference compared to the CAPEX interpolation is that the losses and the OPEX were interpolated as well such that they could be integrated into the LCOE analysis. An area chart presenting the cheapest option for a given distance and power level can be found in Figure 8.8. In this case, the resolution was also increased from 120 to 10 101 data points.

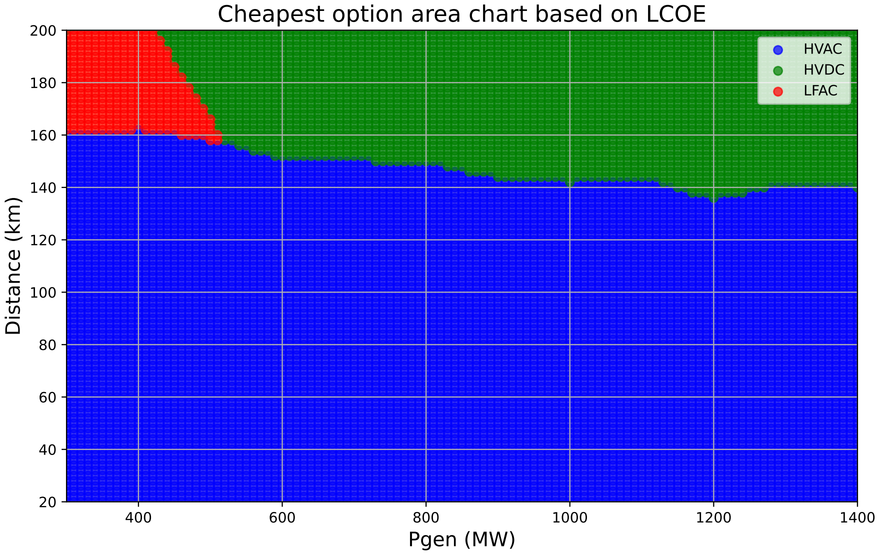

Figure 8.8: Area chart presenting the cheapest export system based on LCOE with increased resolution.

8.3 Sensitivity analysis on the cost of the SFC

As the SFC is not widely used among high-power applications, the cost of the SFC was highly uncertain. In previous sections, the nominal cost per MVA of the SFC was assumed to be equal to a single VSC-HVDC converter. However, this section presents the results of a sensitivity analysis performed on the cost of the SFC, which was varied between -25% to +15%. For each case, the CAPEX and the LCOE analysis area charts are presented.

In Figures 8.9 and 8.10 the cost of the SFC was decreased by 5 % from its nominal cost. The figures present the CAPEX and the LOCE analysis respectively.

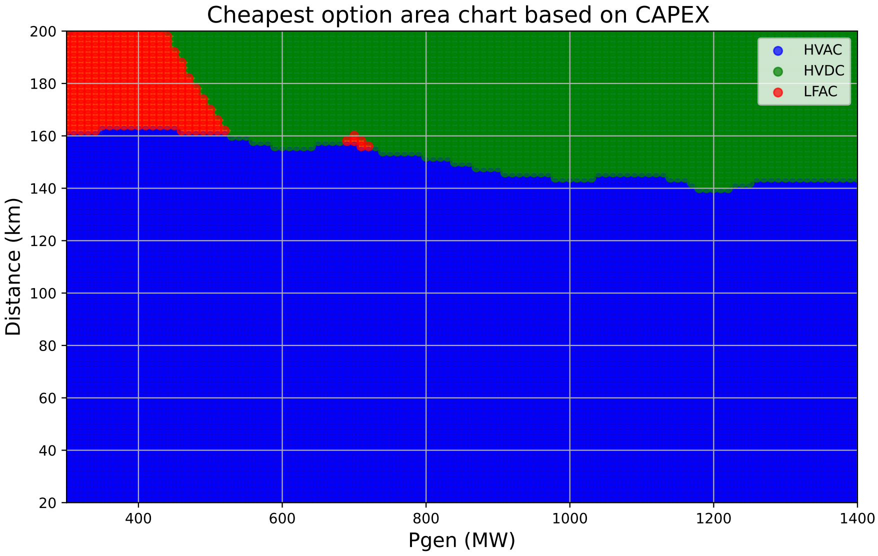

Figure 8.9: Area chart presenting the cheapest export system based on CAPEX with the SFC cost reduced by 5%.

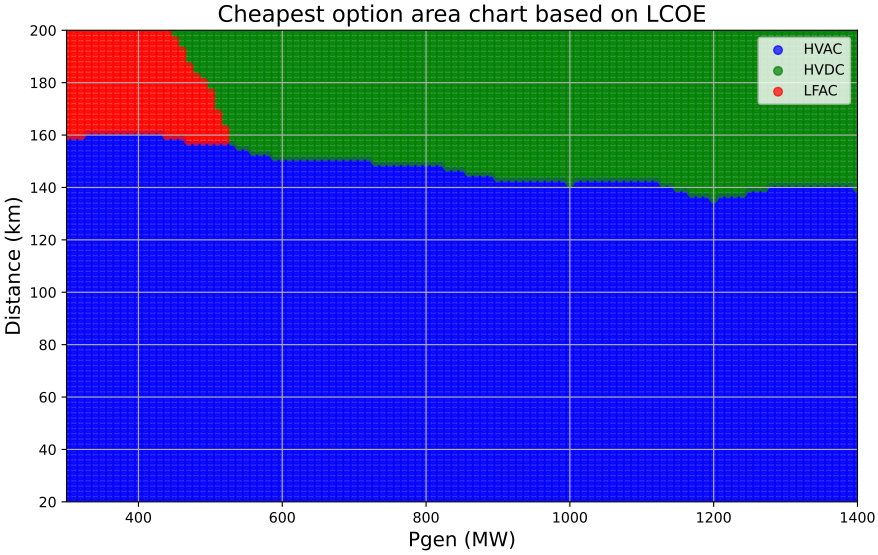

Figure 8.10: Area chart presenting the cheapest export system based on LCOE with the SFC cost reduced by 5%.

In Figures 8.11 and 8.12 the cost of the SFC was decreased by 15 % from its nominal cost. The figures present the CAPEX and the LOCE analysis respectively.

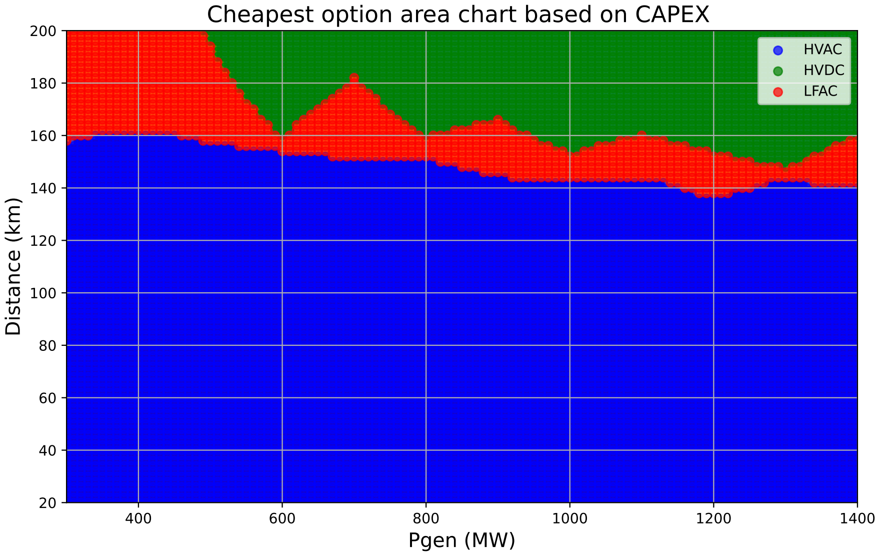

Figure 8.11: Area chart presenting the cheapest export system based on CAPEX with the SFC cost reduced by 15%.

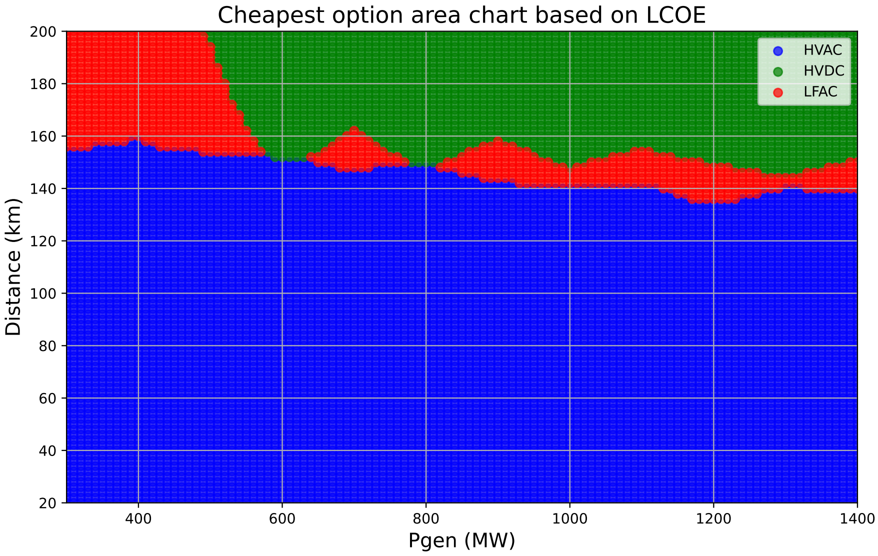

Figure 8.12: Area chart presenting the cheapest export system based on LCOE with the SFC cost reduced by 15%.

In Figures 8.13 and 8.14 the cost of the SFC was decreased by 25 % from its nominal cost. The figures present the CAPEX and the LOCE analysis respectively.

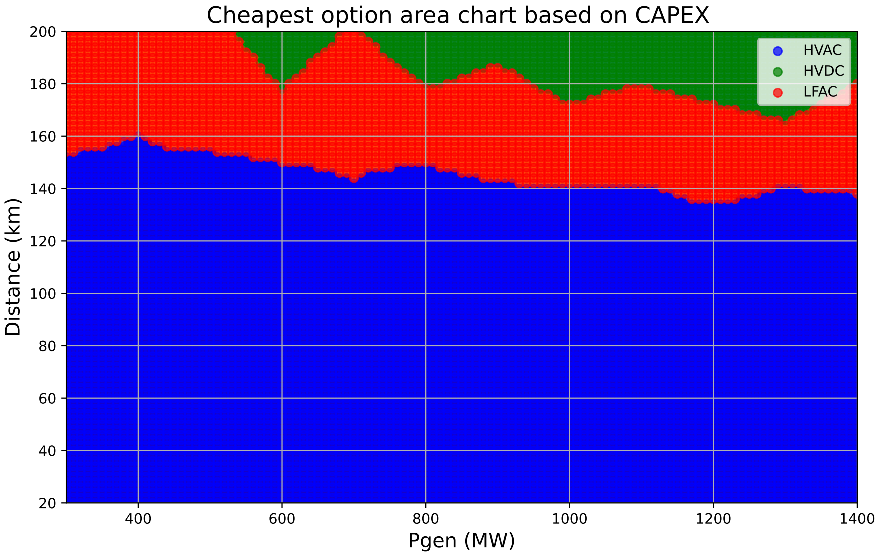

Figure 8.13: Area chart presenting the cheapest export system based on CAPEX with the SFC cost reduced by 25%.

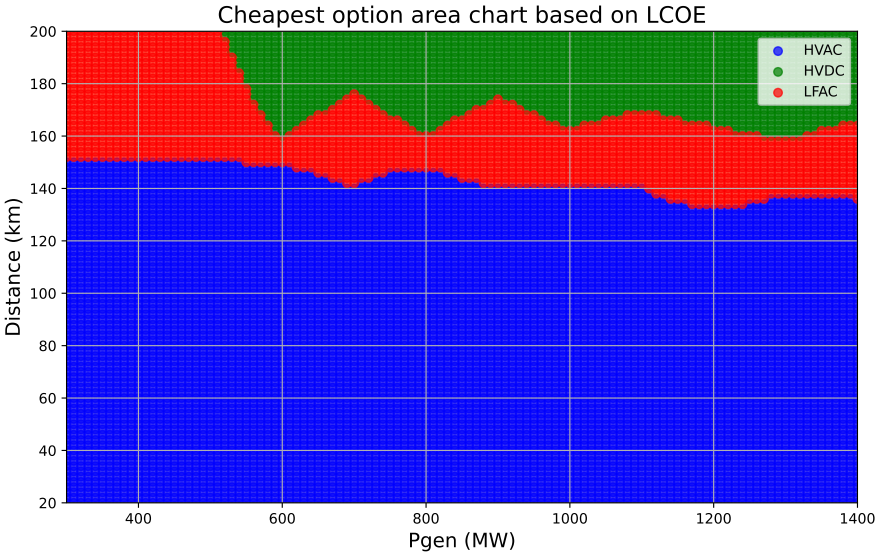

Figure 8.14: Area chart presenting the cheapest export system based on LCOE with the SFC cost reduced by 25%.

In Figures 8.15 and 8.16 the cost of the SFC was increased by 5 % from its nominal cost. The figures present the CAPEX and the LOCE analysis respectively.

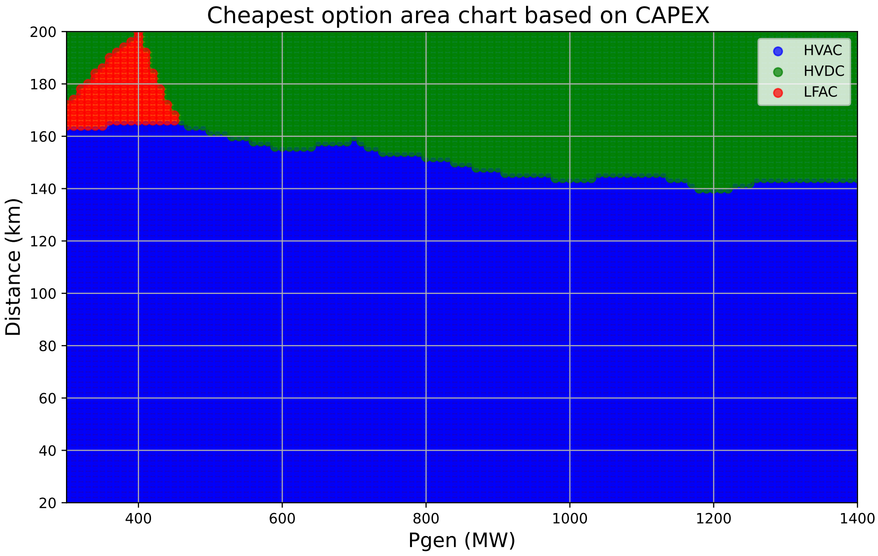

Figure 8.15: Area chart presenting the cheapest export system based on CAPEX with the SFC cost increased by 5%.

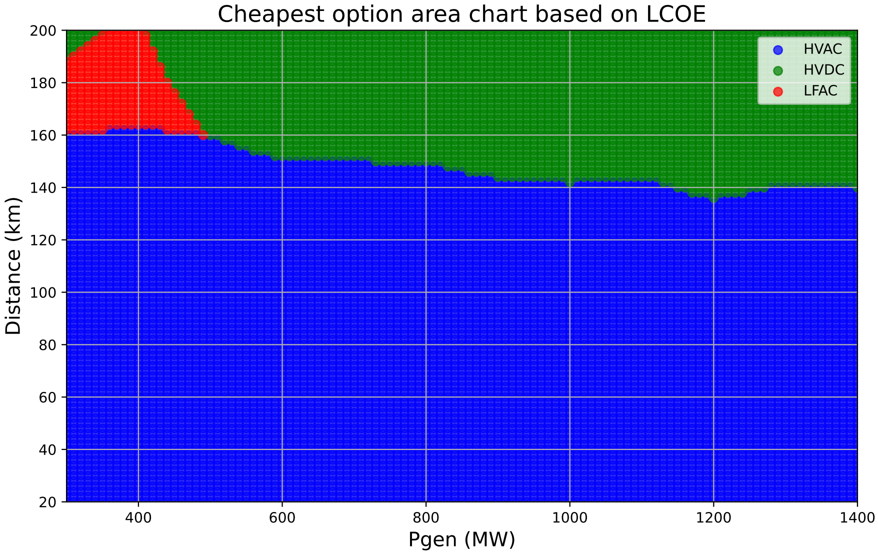

Figure 8.16: Area chart presenting the cheapest export system based on LCOE with the SFC cost increased by 5%.

In Figures 8.17 and 8.18 the cost of the SFC was increased by 15 % from its nominal cost. The figures present the CAPEX and the LCOE analysis respectively.

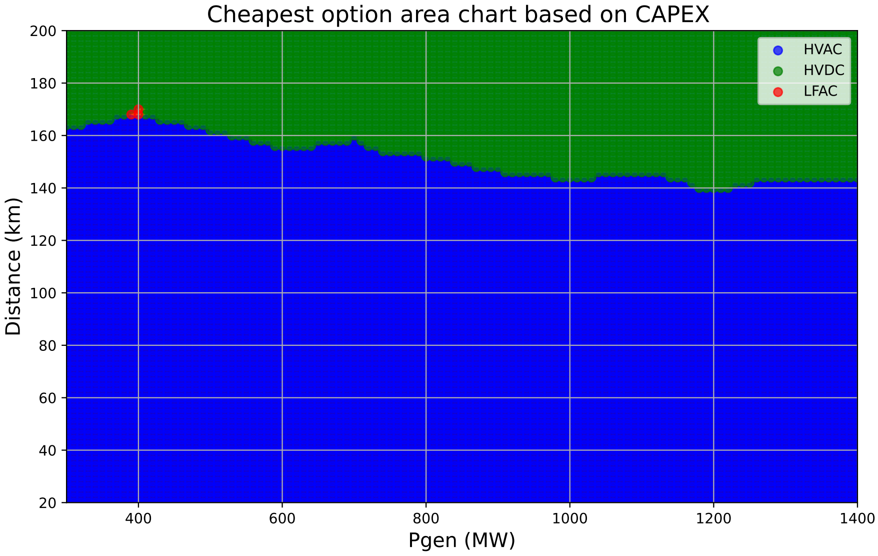

Figure 8.17: Area chart presenting the cheapest export system based on CAPEX with the SFC cost increased by 15%.

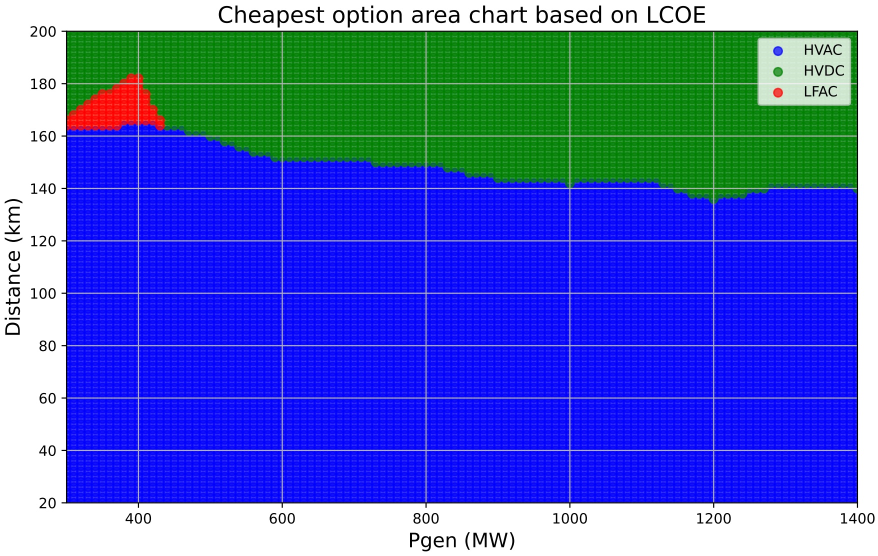

Figure 8.18: Area chart presenting the cheapest export system based on LCOE with the SFC cost increased by 15%.

9

Discussion

This chapter presents a discussion of the results, mainly related to the techno-economic break-even point.

9.1 CAPEX analysis

From the performed CAPEX analysis, it can be seen that the CAPEX break-even distance between HVAC and HVDC lies between 140 - 160 km depending on the power level. As the power level increases, the break-even distance decreases. This is to be expected since the major cost at longer distances and power levels is the cost of the export cables. As the power level and distance increases for HVAC, the required number of parallel cables and their cross-sectional area increases drastically due to the charging currents resulting in an exponential growth of the CAPEX for HVAC while the CAPEX for HVDC increases linearly.

For LFAC, the CAPEX business case is relatively small. The break-even distance is confined to low-power, long-distance applications. What enabled LFAC to win at low-power, long-distance applications were mainly related to that a single converter was used instead of two in the case of HVDC. As the power level increased, the cost of cables became the major driving force. It could be seen that the break-even point between LFAC and HVDC lies around 500 MW. As the export system voltage of the HVDC is increased from ±150 kV to ±320 kV above 500 MW, it results in even smaller cables for HVDC while the LFAC system keeps the export system voltage at 220 kV resulting in an increased size of the export cables. The break-even distance for LFAC compared to HVAC was 160 km. Since the CAPEX of both LFAC and HVDC increases linearly, but with different derivatives, LFAC just replaces some of the HVDC business cases for the low-power applications.

9.2 LCOE analysis

By studying LCOE instead, a fairer comparison between the export system topologies is achieved. The reason is that LCOE covers the expenditures attached to each topology throughout its lifetime. The LCOE also covers the lost revenue due to losses, and the OPEX of each system. The output of the LCOE analysis is to determine the minimum electricity price over the lifetime at which the energy must be sold at for the configurations to be profitable. By comparing HVAC and HVDC, a steady decline in the break-even distance can be seen as the power level increases and the break-even point can be found at around 140 - 160 km. The reason was that as power level and distance increased, the cables became the driving force of the cost. In the LCOE analysis, the losses and the OPEX were taken into consideration resulting in a slightly decreased break-even distance for LCOE compared to the CAPEX analysis.

By comparing the break-even distance of LFAC to HVDC, it could be seen that the economic range of LFAC was slightly increased in the direction of power level. As the difference in losses was small, it was most likely related to the OPEX. LFAC has an additional transformer but one less converter, hence the difference in OPEX of the additional converter gave LFAC a slightly greater economic range compared to the CAPEX analysis. The break-even point between LFAC and HVAC was relatively unchanged compared to the CAPEX analysis.

9.3 Sensitivity analysis

A sensitivity analysis was performed on the cost of the SFC to sbserve how the economic range of LFAC changed. Since the CAPEX was reduced, the sensitivity analysis could also be seen as a sensitivity analysis of any component of the LFAC system. However, in that case, with the fixed OPEX percentage of the SFC for the LCOE analysis.

From the sensitivity analysis, it could be seen that when the cost of the SFC was reduced, the break-even distance between LFAC and HVAC barely changed at all. The reason is the HVAC's exponential behavior. A slight decrease in cost did not drastically affect the break-even distance between LFAC and HVAC.

By instead comparing the break-even point between LFAC and HVDC, it could be seen that the variation in cost had a greater impact on the break-even point. For the decrease in cost, two things occurred. Firstly, the break-even point in the direction of power was relatively stable at 500 - 600 MW. This was related to the shift in voltage of the HVDC system which resulted in lower currents and thereby smaller and fewer cables. Secondly, the break-even distance in the distance direction increased due to the decreased non-distance dependent cost.

When the cost of the SFC was increased, the economic range of LFAC disappeared. The reason was that the break-even point between LFAC and HVDC occurred before any of them had intersected with the lower HVAC cost. Since the lowest studied power level was 300 MW, and the longest studied distance was 200 km, business cases most likely still exist below 300 MW, especially for low-power, long-distance applications.

9.4 Consideration of lost revenue until the project is operational

It should also be mentioned that the lead time, the time from decision to an installed system, is longer for HVDC compared to HVAC. An HVAC system will be able to generate revenue and start to cover the investment faster than HVDC. Therefore the lost revenue will also play a role in the decision of what export system to use. It might also affect the financing of the projects since the investors will start to see a return on the investment earlier in time for HVAC compared to HVDC which might decrease the uncertainties of the investment.

9.5 Validation of LCOE analysis by comparison to real-world projects

Since LCOE was determined as the best KPI to identify the techno-economic break-even point between the export systems, a comparison could be made to the already installed projects offshore wind farms and projects under construction to verify the results from the LCOE analysis. From previous chapters, Figure 3.6 presents installed and wind farms under construction, and Figure 8.8 presents the results from the LCOE analysis. These figures were combined such that the break-even point from this study can be compared to real-world projects as seen in Figure 9.1.

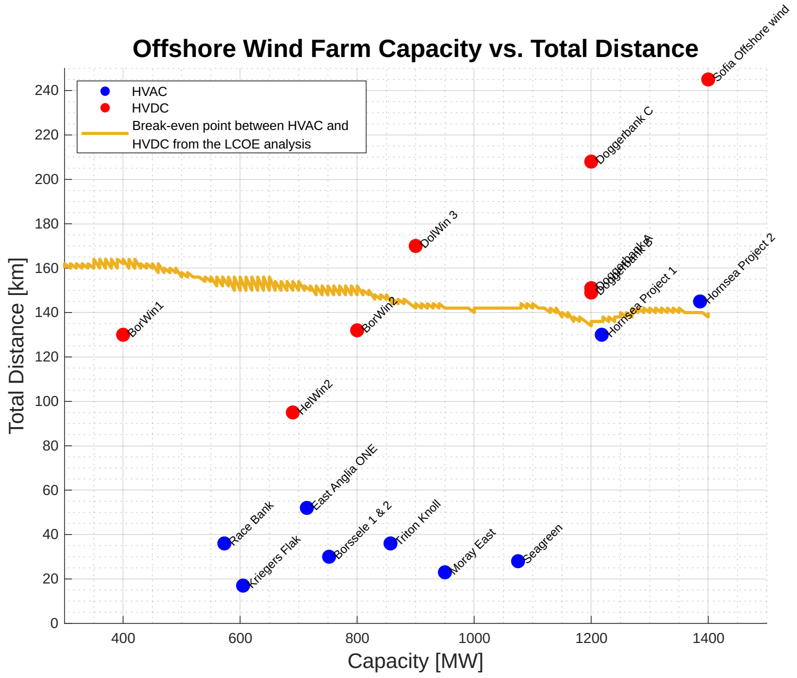

Figure 9.1: Plot comparing real world projects against the HVAC/HVDC break-even point from the LCOE analysis.

From the real-world projects, the plot indicated that the break-even distance between HVAC and HVDC seemed to lie at roughly 130 - 150 km if the outlier, HelWin2, was excluded. Then from the LCOE analysis, the indicated break-even point lay between 140 - 160 km depending on the power level. Since the simulated values were in agreement with the real-world parameters, the analysis could be seen as validated. However, it should be mentioned that for the real-world data other parameters play a role as well. The first is that the cost set of the projects might have changed since their commissioning which could affect the choice of the export system. Another parameter is the grid onshore where the strength of the onshore grid in the connection points might affect the choice of topology. Another parameter is politics which might prefer certain topologies by lobbying and subsidies. But, in conclusion, the LCOE analysis agrees with the real-world projects, and the model was therefore considered validated.

10

Conclusion

In summary, three export system topologies have been evaluated for offshore wind applications. Firstly 120 models for each topology were implemented and dimensioned in PowerFactory such that the considered grid codes were fulfilled. Load-flow studies were performed for distances ranging from 0 to 200 km, and the installed active power of the wind farm was varied from 300 to 1400 MW. As the electrical results were validated, the electrical data was imported into Python so that the economic evaluation could be performed. Firstly the techno-economic evaluation consisted of a CAPEX analysis. Then an LCOE analysis was performed to signify what export system topology is favorable at what distance, and power level.

The results showed that HVAC was the preferred topology for offshore wind when the distance from shore is shorter, with the break-even distance ranging from 0 to 160 km. As the installed capacity increased, the economic range for HVAC decreased to roughly 140 km mainly due to the immense cost of HVAC cables and the required size of reactive power compensation.

The LCOE analysis also concluded that HVDC was the preferred topology for long-distance transmission, and the break-even distance between HVDC and HVAC was roughly 140 - 160 km depending on the installed capacity. The break-even distance was mainly related to the investment cost for an HVDC transmission system, as it required a large platform and two HVDC converters which resulted in a large initial investment cost. As the cost of the export cables was considerably lower compared to HVAC, the exponential CAPEX behavior of the HVAC system intersects with the HVDC CAPEX due to the high CAPEX of the HVAC cables.

Furthermore, LFAC was found to be the preferred solution for a smaller wind farm located far from shore. LFAC had the same break-even distance as HVDC for lower installed active power capacities up to 500 MW compared to HVAC. Hence the distance break-even point was found to be located at a transmission distance of roughly 160 km. The other break-even point for LFAC, the installed capacity break-even point, was observed between 400 to 500 MW compared to HVDC. The reason that LFAC is suitable from an economic perspective at low power and long-distance was mainly related to the lower CAPEX compared to HVDC. Since the derivative of the LFACs LCOE is higher than the derivative of HVDC, for low power levels, the LFAC curve intersects with HVAC before it intersects with HVDC. When the transmission voltage for HVDC was increased from ±150 kV to ±320 kV above 500 MW, the size of the HVDC cables could be reduced such that the HVDC curve was the first one to intersect with the HVAC curve.

The sensitivity analysis concluded that a decreased cost of the SFC barely affected the break-even distance between LFAC and HVAC. However, a decreased cost does affect the relationship between LFAC and HVDC. As the cost was reduced, LFAC gained in the medium to long-distance segment for all power levels while remaining the technology of choice for low-power, long-distance applications. Then, as the cost was increased, the business case for LFAC vanished more and more as HVDC became the cheaper solution.

In reality, the break-even point depends on several parameters that vary between wind farm projects such as water depth, subsidies, politics, and more. This study has showcased a general trend as to which configuration is the most suitable given a certain power level and transmission distance, while in reality, it differs due to different circumstances from project to project. This study has investigated techno-economic parameters when it comes to the construction of an export system for a wind farm. The economic parameters consisted of investment and maintenance costs associated with the wind farm. However, parameters such as lead time, and availability were not considered when the economic analysis was performed. Additionally, the lost revenue due to the long lead time for components was not considered which in turn might affect the funding of the project. Nonetheless, as the discussion indicated, when the LCOE analysis performed in this study was compared to the real-world projects, the outcomes were similar which increases the trustworthiness of the LCOE analysis results.

In conclusion, for all distances below 140 to 160 km, HVAC is the given topology. For distances over 140 to 160 km and power levels over 500 MW, HVDC i the given topology. For the remaining low-power, long-distance applications, LFAC has an edge.

10.1 Future work

This thesis has investigated three different transmission configurations for offshore wind which is a hot topic at this moment in time. Hence, plenty of further research can be investigated following this thesis. This section presents suggestions for future work following this thesis.

10.1.1 Improvements of this study

Firstly, this study has only concluded load-flow analysis. As there are a lot more grid code requirements to fulfill, dynamic studies have to be performed to determine the final dimensioning of components. Therefore this study gives an indication of the dimensioning, but not the final design. Secondly, some optimization can be performed. In this study components were dimensioned after the voltage limits, therefore one way to minimize the shunt reactors needed could be to reduce the voltage setpoint of the WTGs such that the voltage limits are not violated. The relation between shunt reactors and cables could also be further studied to optimize the cost of the system. Lastly, since the rating of the SFC modules is relatively low, a BtB solution might be more viable for the LFAC system at higher power levels.

10.1.2 Integration of intermittent power by utilizing the E-STATCOM

In this study, the external grid has been assumed as infinitely strong, and the power output from the turbines was constant. However, that is not the case for real-world applications, therefore the E-STATCOM has been proposed as a solution to the problem. Since the injected active power at the PCC varies over time due to changes in wind speed, an E-STATCOM can either absorb or inject active power during excess- or deficit energy production respectively. The E-STATCOM will then calculate a setpoint for the active power, and if the injected active power at the PCC is too high, the E-STATCOM will charge its storage. If the injected active power at the PCC is below its setpoint, the E-STATCOM will inject active power. The result at the PCC is a constant, non-fluctuating injected active power by the offshore wind farm since the E-STATCOM can regulate the injected active power while still regulating the reactive power. The E-STATCOM has been proposed as a well-performing solution to integrate intermittent power plants into weak grids. The E-STATCOM improved low-voltage ride-through performance, power smoothening of the injected power to the PCC, frequency support, balancing of currents and voltages at the PCC, and harmonic performance. Therefore, to fulfill grid code requirements, the E-STATCOM is a viable option to be able to integrate intermittent power plants to the transmission grid [40], [54].

10.1.3 All DC export systems

In this report, the turbines were assumed to provide AC to the inter-array cables, but other solutions have also been suggested. One suggestion is an MVDC/HVDC grid. In this solution, there is firstly an AC/DC converter in the wind turbine and then a DC/DC converter to step up the DC voltage to a medium voltage for the collector grid. The MVDC collector grid is then routed to an offshore platform where the MVDC is stepped up to HVDC via a DC/DC converter. Another proposed solution is an all-MVDC grid. As in the previous solution, the collector grid operates at MVDC. The collector grid is then routed to an offshore substation that collects the power from all turbines which is then sent through an MVDC export cable from the offshore substation to the onshore substation [50].

Bibliography

[1] Enerdata. "“world power consumption: Electricity consumption”." (Aug. 2022), [Online]. Available: `https://yearbook.enerdata.net/electricity/electricity-domestic-consumption-data.html` (visited on 01/15/2024).

[2] H. Allamehzadeh. "Wind energy history, technology and control." (2016), [Online]. Available: `https://ieeexplore.ieee.org/stamp/stamp.jsp?arnumber=7897153` (visited on 01/23/2024).

[3] K. Johansen, "Wind energy in denmark: A short history [history]," *IEEE Power and Energy Magazine*, vol. 19, no. 3, pp. 94–102, 2021. DOI: `10.1109/MPE.2021.3057973`.

[4] T. Bookman, "Wind energy's promise, offshore," *IEEE Technology and Society Magazine*, vol. 24, no. 2, pp. 9–15, 2005. DOI: `10.1109/MTAS.2005.1442376`.

[5] M. D. Esteban, J. J. Diez, J. S. López, and V. Negro, "Why offshore wind energy?" *Renewable Energy*, vol. 36, no. 2, pp. 444–450, 2011, ISSN: 0960-1481. DOI: `https://doi.org/10.1016/j.renene.2010.07.009`. [Online]. Available: `https://www.sciencedirect.com/science/article/pii/S0960148110003332`.

[6] Ørsted. "1991-2001 the first offshore wind farms." (), [Online]. Available: `https://orsted.com/en/insights/white-papers/making-green-energy-affordable/1991-to-2001-the-first-offshore-wind-farms` (visited on 01/23/2024).

[7] G. Herzig. "Global Offshore Wind Report 2022." (), [Online]. Available: `https://wfo-global.org/wp-content/uploads/2023/03/WFO_Global-Offshore-Wind-Report-2022.pdf` (visited on 01/23/2024).

[8] A. Buljan. "Offshore Wind Turbines in 2023: 16 MW Model Installed Offshore, 18 MW WTGs Selected for New Project, 22 MW Turbine Announced." (), [Online]. Available: `https://www.offshorewind.biz/2024/01/02/offshore-wind-turbines-in-2023-16-mw-model-installed-offshore-18-mw-wtgs-selected-for-new-project-22-mw-turbine-announced/` (visited on 01/23/2024).

[9] J. Ruddy, R. Meere, and T. O'Donnell, "Low Frequency AC transmission for offshore wind power: A review," *Renewable and Sustainable Energy Reviews*, vol. 56, pp. 75–86, 2016, ISSN: 1364-0321. DOI: `https://doi.org/10.1016/j.rser.2015.11.033`. [Online]. Available: `https://www.sciencedirect.com/science/article/pii/S1364032115012988`.

[10] J. Ge, H. Yu, G. Zhao, Z. Deng, and C. Wang, "Research on low-frequency offshore wind power transmission and frequency conversion technology," in

2020 IEEE 4th Conference on Energy Internet and Energy System Integration (EI2), 2020, pp. 464–468. DOI: `10.1109/EI250167.2020.9347016`.

[11] “Svenska kraftnät. vägledning för anslutning till stamnätet; från ansökan till idrifttagning.” (Dec. 2023), [Online]. Available: `https://www.svk.se/siteassets/aktorsportalen/anslut-till-transmissionsnatet/vagledning-for-anslutning-till-stamnatet_231231.pdf` (visited on 01/16/2023).

[12] “United nations. goal 7: Affordable and clean energy.” (), [Online]. Available: `https://www.unep.org/explore-topics/sustainable-development-goals/why-do-sustainable-development-goals-matter/goal-7`.

[13] R. G. Sullivan, J. Cothren, S. L. Winters, C. Cooper, M. Williamson, and D. Ball, “An assessment of offshore wind turbine visibility in the united kingdom,” in *2012 Oceans*, 2012, pp. 1–9. DOI: `10.1109/OCEANS.2012.6405138`.

[14] D. Rowell, D. McMillan, and J. Carroll, “Offshore wind h&s: A review and analysis,” *Renewable and Sustainable Energy Reviews*, vol. 189, p. 113 928, Oct. 2023. DOI: `10.1016/j.rser.2023.113928`.

[15] S. C. Mangi, “The impact of offshore wind farms on marine ecosystems: A review taking an ecosystem services perspective,” *Proceedings of the IEEE*, vol. 101, no. 4, pp. 999–1009, 2013. DOI: `10.1109/JPROC.2012.2232251`.

[16] J. Sahlin. ““poseidon - mkb för etablering av havsbaserad vindkraft”.” (Dec. 2022), [Online]. Available: `https://mst.dk/media/5tfn5j0t/kn2023_00991-1-bilaga-d-miljoekonsekvensbeskrivning.pdf` (visited on 01/16/2024).

[17] E. Willén, E.-M. Arvidsson, and S. Loukkola. ““vindkraftpark erik segersäll”.” (Mar. 2022), [Online]. Available: `https://ym.fi/documents/1410903/0/Samr%C3%A5dsunderlag+Erik+Segers%C3%A4ll+sv.pdf/a739cd62-6132-7b95-e45c-f32717eceb45/Samr%C3%A5dsunderlag+Erik+Segers%C3%A4ll+sv.pdf?t=1654857021264` (visited on 01/17/2024).

[18] M. Papapetrou and G. Kosmadakis, “Chapter 9 - Resource, environmental, and economic aspects of SGHE,” in *Salinity Gradient Heat Engines*, ser. Woodhead Publishing Series in Energy, A. Tamburini, A. Cipollina, and G. Micale, Eds., Woodhead Publishing, 2022, pp. 319–353, ISBN: 978-0-08-102847-6. DOI: `https://doi.org/10.1016/B978-0-08-102847-6.00006-1`. [Online]. Available: `https://www.sciencedirect.com/science/article/pii/B9780081028476000061`.

[19] K. Adam, V. Hoolohan, J. Gooding, T. Knowland, C. S. Bale, and A. S. Tomlin, “Methodologies for city-scale assessment of renewable energy generation potential to inform strategic energy infrastructure investment,” *Cities*, vol. 54, pp. 45–56, 2016, Cities, Energy and Climate Change Mitigation, ISSN: 0264-2751. DOI: `https://doi.org/10.1016/j.cities.2015.10.015`. [Online]. Available: `https://www.sciencedirect.com/science/article/pii/S0264275115001687`.

[20] N. G. HINGORANI and G. LASZLO, “Voltage-Sourced Converters,” in *Understanding facts: Concepts and technology of flexible AC Transmission Systems*. John Wiley and Sons, 2000.

[21] Y. S. Qiuwei Wu, “Modeling and Modern Control of Wind Power,” in 2018. DOI: `10.1002/9781119236382.ch2`.

[22] J. Luo, K. Lin, J. Li, Y. Xue, and X.-P. Zhang, "Cost analysis and comparison between modular multilevel converter (MMC) and modular multilevel matrix converter (M3C) for offshore wind power transmission," in *15th IET International Conference on AC and DC Power Transmission (ACDC 2019)*, 2019, pp. 1–6. DOI: `10.1049/cp.2019.0063`.

[23] J. Ruddy, R. Meere, and T. O'Donnell, "Low Frequency AC transmission for offshore wind power: A review," *Renewable and Sustainable Energy Reviews*, vol. 56, pp. 75–86, 2016, ISSN: 1364-0321. DOI: `https://doi.org/10.1016/j.rser.2015.11.033`. [Online]. Available: `https://www.sciencedirect.com/science/article/pii/S1364032115012988`.

[24] *Guide to an offshore wind farm*, Jan. 2019. [Online]. Available: `https://www.thecrownestate.co.uk/media/2861/guide-to-offshore-wind-farm-2019.pdf`.

[25] H. Saadat, *Power System Analysis* (Electrical and Computer Engineering Series). WCB/McGraw-Hill, 1999, ISBN: 9780070122352.

[26] Chalmers tekniska högskola, *ELTEKNIK*, 1st ed. Institutionen för Energi och miljö, Mar. 2010.

[27] S. Karamitsos, "Design and Operation of Low Frequency AC (LFAC) Transmission System for Connecting Offshore Wind Farms," Ph.D. dissertation, Mar. 2020.

[28] C.-K. Kim, V. K. Sood, G.-S. Jang, S.-J. Lim, and S.-J. Lee, *HVDC transmission: Power conversion applications in power systems*. IEEE Press, 2009.

[29] *HVDC Classic*. [Online]. Available: `https://www.siemens-energy.com/global/en/home/products-services/product/hvdc-classic.html` (visited on 02/13/2024).

[30] V. K. Sood, *HVDC and facts controllers: Applications of static converters in power systems*. Kluwer Academic Publishers, 2004.

[31] M. H. Rashid, *Power Electronics Handbook*. Academic Press, 2001.

[32] E. Acha, P. Roncero-Sánchez, V. J. A. d. la, L. M. Castro, and B. Kazemtabrizi, *VSC-FACTS-HVDC: Analysis, modelling and simulation in power grids*. Wiley, 2019.

[33] K. Sharifabadi, L. Harnefors, H. P. Nee, S. Norrga, and R. Teodorescu, *Design, control, and application of modular multilevel converters for HVDC transmission systems*. IEEE Press, Wiley, 2016.

[34] X. Gao, D. Zhou, A. Anvari-Moghaddam, and F. Blaabjerg, "Grid-following and grid-forming control in power electronic based power systems: A comparative study," in *IECON 2021 – 47th Annual Conference of the IEEE Industrial Electronics Society*, 2021, pp. 1–6. DOI: `10.1109/IECON48115.2021.9589432`.

[35] R. L. Sellick and M. Åkerberg, *Comparison of HVDC Light (VSC) and HVDC Classic (LCC) Site Aspects, for a 500MW 400kV HVDC Transmission Scheme*, Dec. 2012. [Online]. Available: `https://library.e.abb.com/public/470ded7bf19bd869c1257af4003999a4/Comparison%20of%20HVDC%20Light%20and%20HVDC%20Classic%20Site%20Aspects.pdf`.

[36] A. Reichenbach, *Electrosmog in the environment*. Swiss Agency for the Environment, Forests and Landscape SAEFL, 2005.

[37] N. Qin, S. You, Z. Xu, and V. Akhmatov, "Offshore wind farm connection with low frequency AC transmission technology," in *2009 IEEE Power & Energy Society General Meeting*, 2009, pp. 1–8. DOI: `10.1109/PES.2009.5275262`.

[38] Y. Meng, S. Yan, K. Wu, *et al.*, "Comparative economic analysis of low frequency AC transmission system for the integration of large offshore wind farms," *Renewable Energy*, vol. 179, pp. 1955–1968, 2021, ISSN: 0960-1481. DOI: `https://doi.org/10.1016/j.renene.2021.07.137`. [Online]. Available: `https://www.sciencedirect.com/science/article/pii/S0960148121011484`.

[39] P. Kundur, *Power System Stability and control*, 1st ed. McGraw Hill, 1994.

[40] A. Bharadwaj, S. Maiti, N. Dhal, S. Chakraborty, and S. K. Pillai, "Chapter 10 - E-STATCOM (energy storage+STATCOM): a solution to integrate large-scale wind farms into the grid at medium and high power levels," in *Power Quality in Modern Power Systems*, P. Sanjeevikumar, C. Sharmeela, J. B. Holm-Nielsen, and P. Sivaraman, Eds., Academic Press, 2021, pp. 283–310, ISBN: 978-0-12-823346-7. DOI: `https://doi.org/10.1016/B978-0-12-823346-7.00007-4`. [Online]. Available: `https://www.sciencedirect.com/science/article/pii/B9780128233467000074`.

[41] E. Haghi, "Chapter Six - Techno-economic analysis of renewable power systems," in *Modeling and Control Dynamics in Microgrid Systems with Renewable Energy Resources*, R. C. Bansal, J. J. Justo, and F. A. Mwasilu, Eds., Academic Press, 2024, pp. 113–136, ISBN: 978-0-323-90989-1. DOI: `https://doi.org/10.1016/B978-0-323-90989-1.00006-3`. [Online]. Available: `https://www.sciencedirect.com/science/article/pii/B9780323909891000063`.

[42] "Levelized Cost of Electricity (LCoE)." (2020), [Online]. Available: `https://noviocean.energy/wp-content/uploads/2022/08/NoviOcean-LCOE-NO500.pdf` (visited on 04/22/2024).

[43] M. A. Cardiel-Alvarez, S. Arnaltes, J. L. Rodriguez-Amenedo, and A. Nami, "Decentralized control of offshore wind farms connected to diode-based hvdc links," *IEEE Transactions on Energy Conversion*, vol. 33, no. 3, pp. 1233–1241, Sep. 2018. DOI: `10.1109/tec.2018.2804662`.

[44] *Interview at Hitachi Energy*, Mar. 2024.

[45] "It's time to connect - technical description of hvdc light® technology$_2$008," *It's time to connect - Technical description of HVDC Light® technology*, 2008. [Online]. Available: `http://www.tdproducts.com/files/36371732.pdf`.

[46] P. I. Nyombi, Z. Zhang, and P. G. Mysore, "Implementation of a New Algorithm to Detect Turn-to-Turn Faults in Shunt Reactors and Identify the Faulted Phase," in *2021 74th Conference for Protective Relay Engineers (CPRE)*, 2021, pp. 1–12. DOI: `10.1109/CPRE48231.2021.9429830`.

[47] "ENTSO-E TYNDP 2024 Offshore Network Development Plans - Methodology." (2024), [Online]. Available: `https://eepublicdownloads.blob.core.windows.net/public-cdn-container/tyndp-documents/ONDP2024/ONDP2024-methodology.pdf` (visited on 04/22/2024).

[48] "Electricity Ten Year Statement 2015 - Appendix E." (2015), [Online]. Available: `https://www.nationalgrid.com/sites/default/files/documents/43742-ETYS15%20AppE%20techonology.pdf`.

[49] "NETZENTWICKLUNGSPLAN STROM 2037/2045, VERSION 2023, 1. ENTWURF." (2023), [Online]. Available: `https://www.netzentwicklungsplan.de/sites/default/files/2023-03/230321_NEP_Kostenschaetzung_NEP2037_2045_V2023_1.Entwurf.pdf`.

[50] V. Timmers, A. Egea-Àlvarez, A. Gkountaras, R. Li, and L. Xu, "All-DC Offshore Wind Farms: When are they more cost-effective than AC designs?" *IET Renewable Power Generation*, vol. 17, no. 10, pp. 2458–2470, Jul. 2022. DOI: `10.1049/rpg2.12550`.

[51] *Investerings- och finansieringsplan för åren 2019–2022*, 2017. [Online]. Available: `https://www.svk.se/siteassets/om-oss/rapporter/2019/investerings--och-finansieringsplan-for-svenska-kraftnat.pdf`.

[52] J. L. Domínguez-García, D. J. Rogers, C. E. Ugalde-Loo, J. Liang, and O. Gomis-Bellmunt, "Effect of non-standard operating frequencies on the economic cost of offshore AC networks," *Renewable Energy*, vol. 44, pp. 267–280, 2012, ISSN: 0960-1481. DOI: `https://doi.org/10.1016/j.renene.2012.01.093`. [Online]. Available: `https://www.sciencedirect.com/science/article/pii/S0960148112001048`.

[53] *Renewable power generation costs in 2022, International Renewable Energy Agency*. Abu Dhabi, 2023.

[54] A. B. Chivukula and S. Maiti, "Analysis and control of modular multilevel converter-based E-STATCOM to integrate large wind farms with the grid," *IET Generation, Transmission & Distribution*, vol. 13, no. 20, pp. 4604–4616, 2019. DOI: `https://doi.org/10.1049/iet-gtd.2018.5928`. eprint: `https://ietresearch.onlinelibrary.wiley.com/doi/pdf/10.1049/iet-gtd.2018.5928`. [Online]. Available: `https://ietresearch.onlinelibrary.wiley.com/doi/abs/10.1049/iet-gtd.2018.5928`.

A

Appendix 1

Figures A.1, A.2, and A.3 presents the size distribution of the shunt reactors for all studied power levels and distances of the HVAC system. The blue curve is the size of the onshore shunt reactor, the dotted red line is the size of the offshore shunt reactor, and the yellow line is the size of the midpoint shunt reactor.

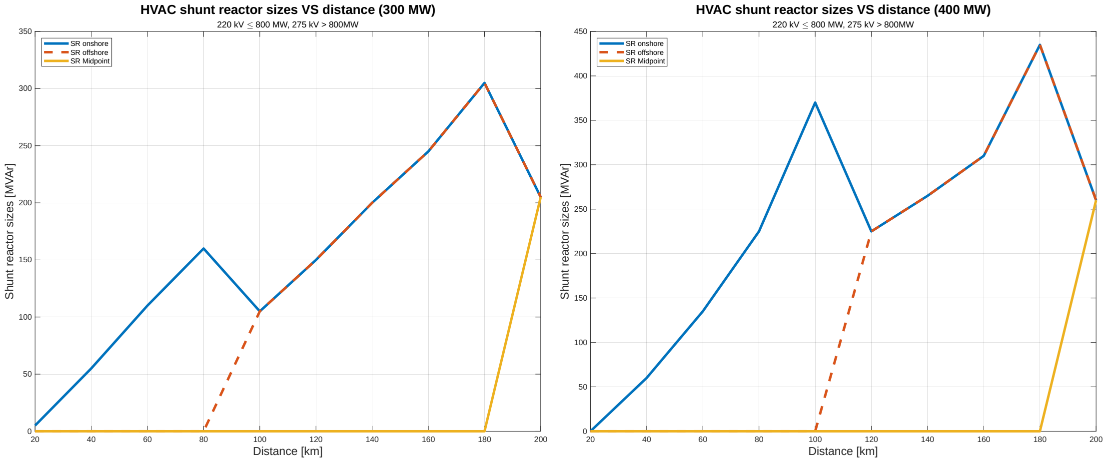

(a) P = 300 MW. *(b)* P = 400 MW.

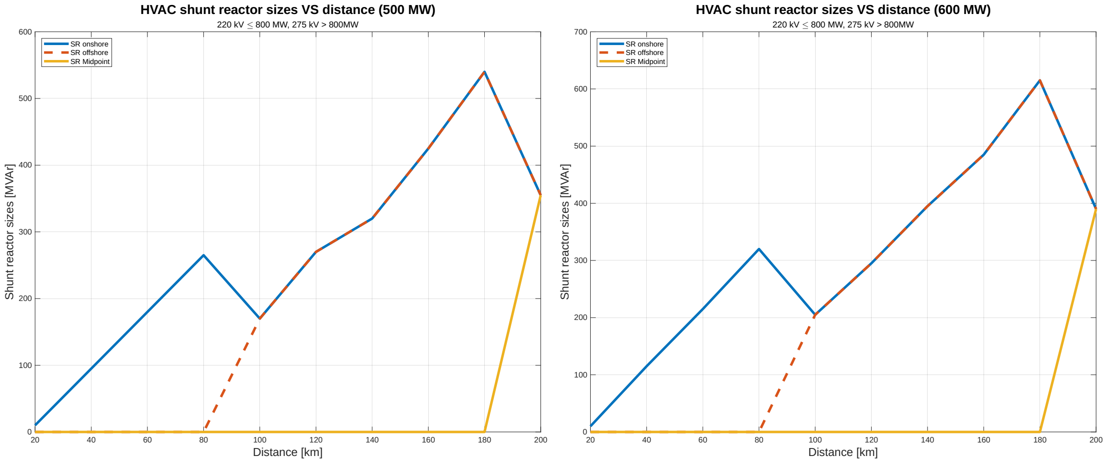

(c) P = 500 MW. *(d)* P = 600 MW.

Figure A.1: Shunt reactor size distribution vs distance. P is the installed active power of the wind farm.

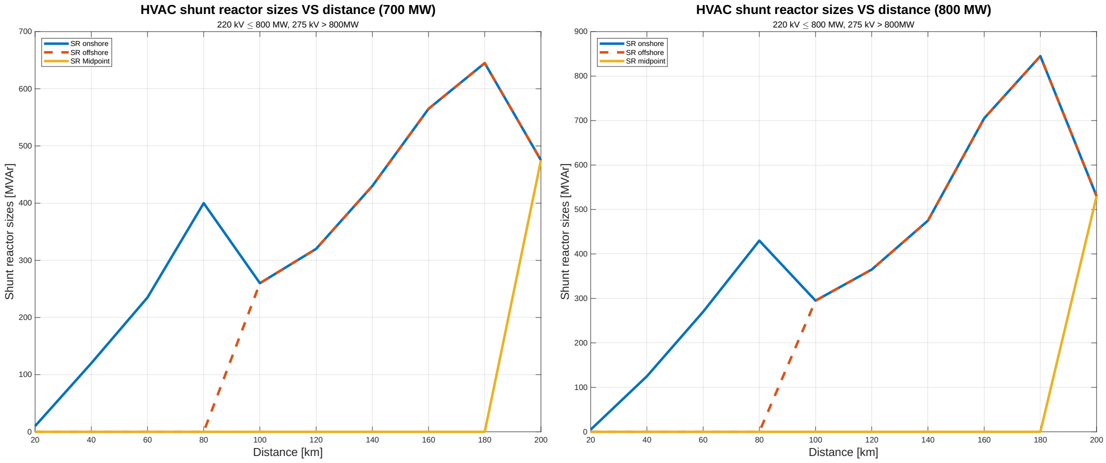

(a) P = 700 MW. *(b)* P = 800 MW.

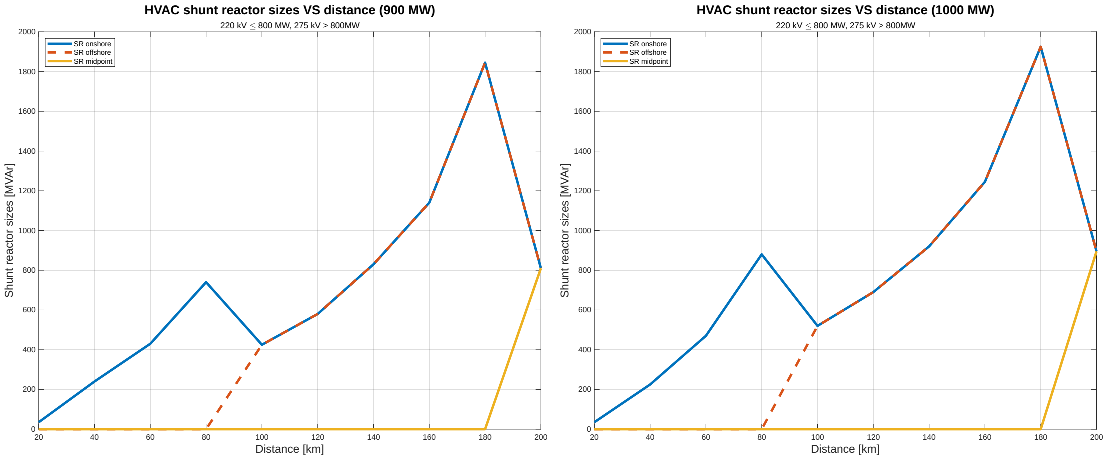

(c) P = 900 MW. *(d)* P = 1000 MW.

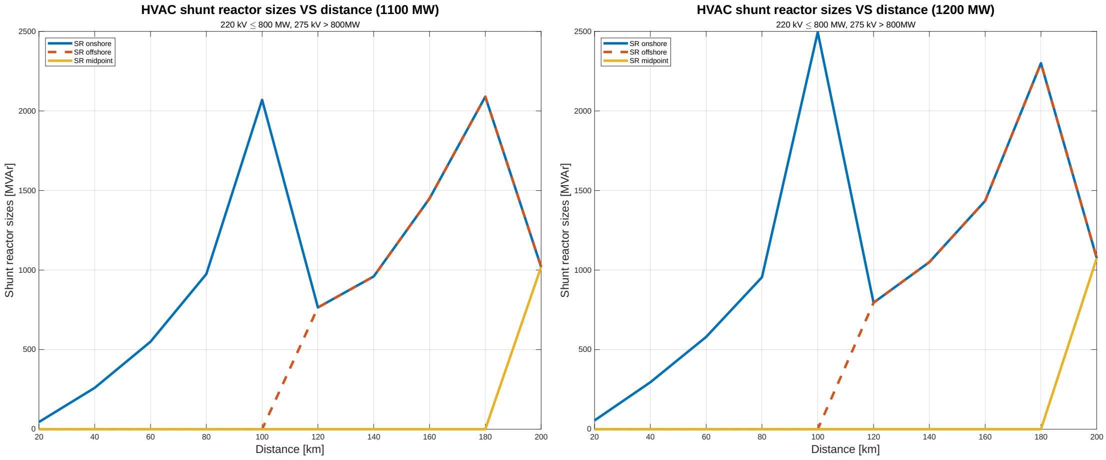

(e) P = 1100 MW. *(f)* P = 1200 MW.

Figure A.2: Shunt reactor size distribution vs distance. P is the installed active power of the wind farm.

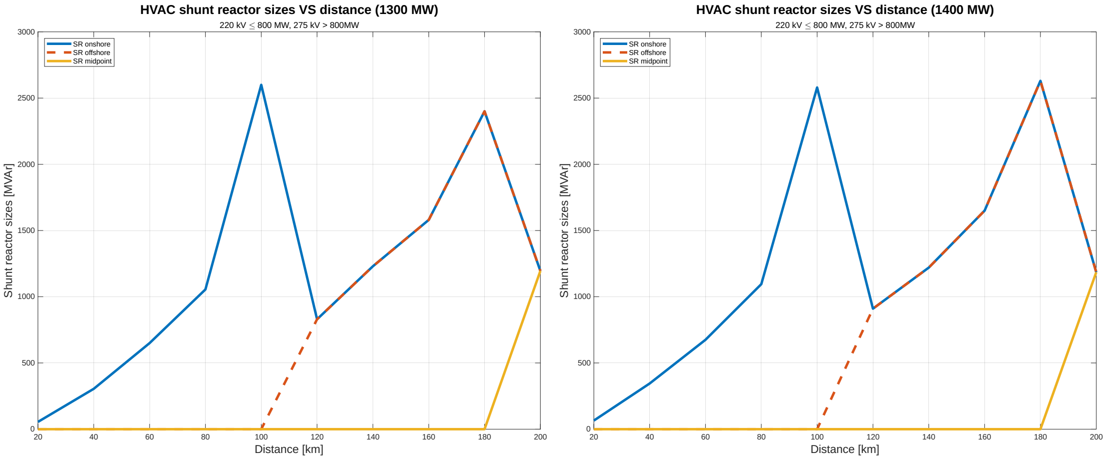

(a) P = 1300 MW.

(b) P = 1400 MW.

Figure A.3: Shunt reactor size distribution vs distance. P is the installed active power of the wind farm.

B

Appendix 2

Figures B.1, B.2, and B.3 presents the CAPEX analysis for all studied power levels and distances of the three topologies. Due to the used method in the electrical dimensioning, HVAC was interpolated between 80 - 120 km for power levels above 1000 MW. The blue line represents the CAPEX of HVAC, the dotted red line represents the interpolated HVAC, the green line represents LFAC, and the orange line represents HVDC.

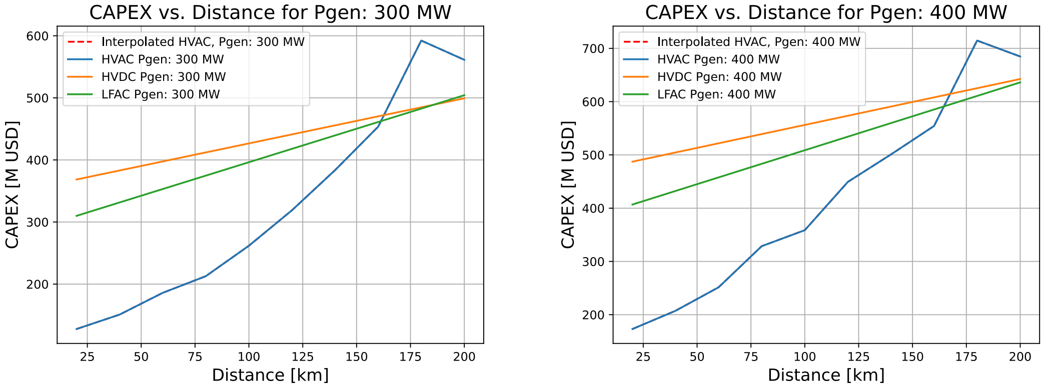

(a) P = 300 MW.

(b) P = 400 MW.

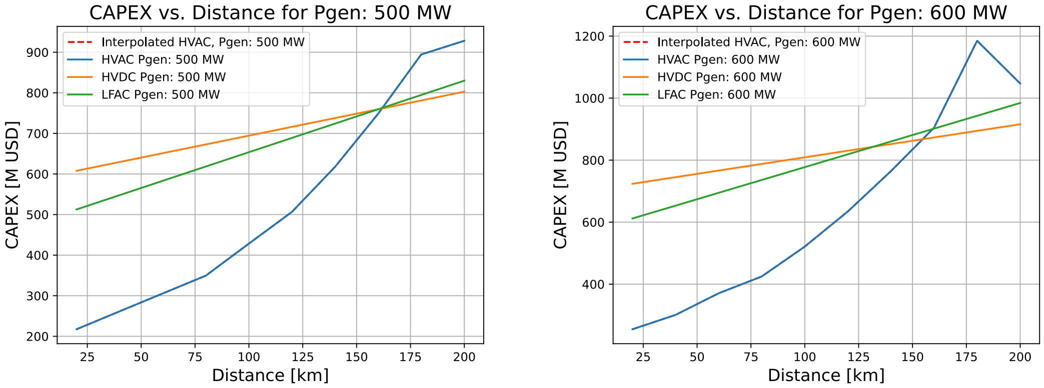

(c) P = 500 MW.

(d) P = 600 MW.

Figure B.1: Plots presenting the CAPEX analysis with the HVAC CAPEX interpolated between 80 - 120 km for some configurations. P is the installed active power of the wind farm.

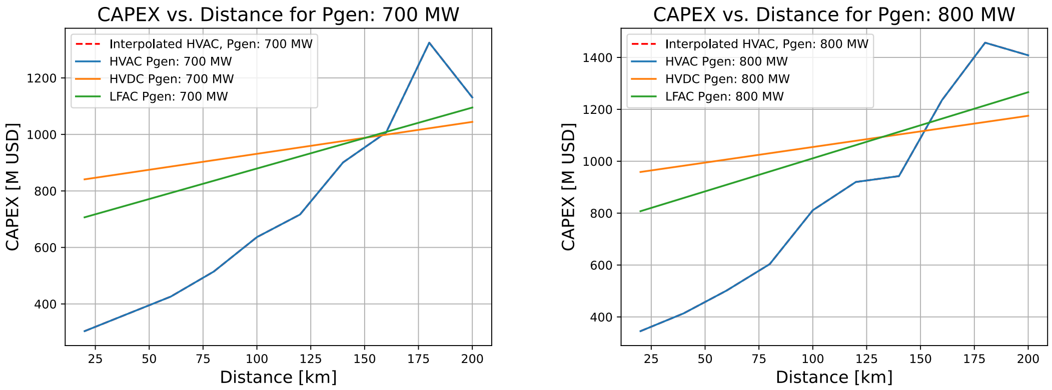

(a) P = 700 MW.

(b) P = 800 MW.

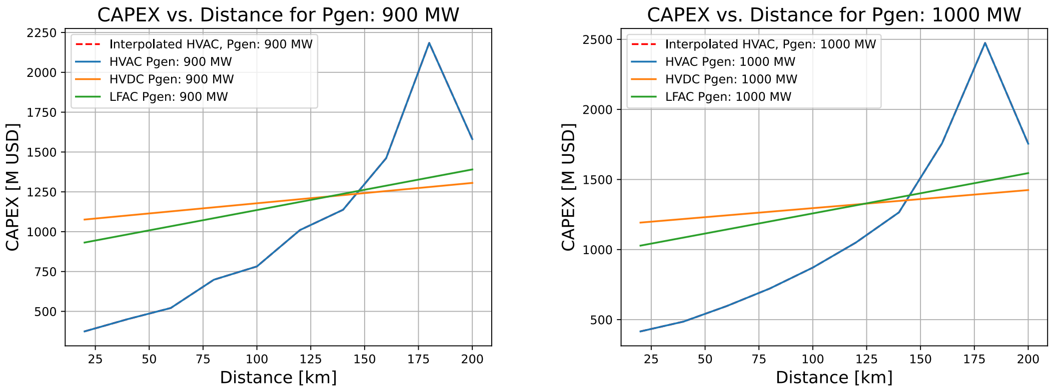

(c) P = 900 MW.

(d) P = 1000 MW.

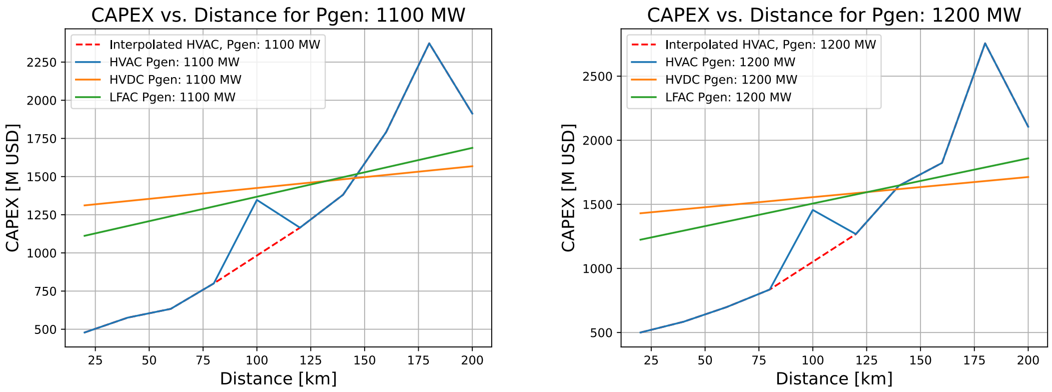

(e) P = 1100 MW.

(f) P = 1200 MW.

Figure B.2: Plots presenting the CAPEX analysis with the HVAC CAPEX interpolated between 80 - 120 km for some configurations. P is the installed active power of the wind farm.

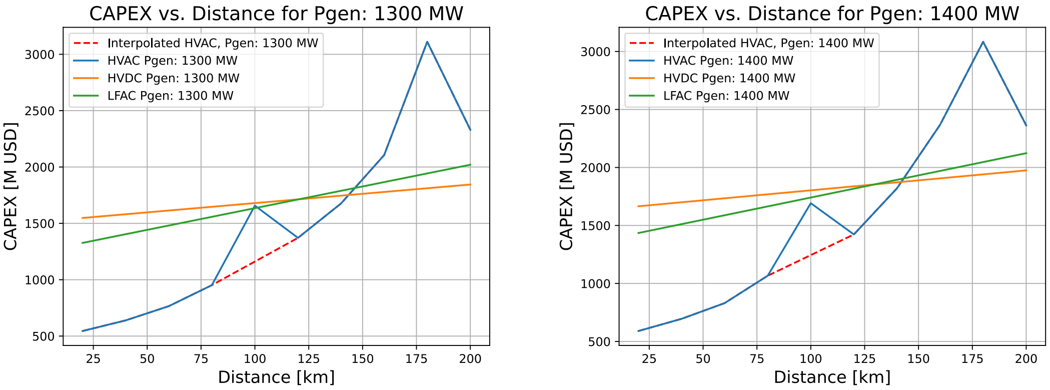

(a) P = 1300 MW. ***(b)*** P = 1400 MW.

Figure B.3: Plots presenting the CAPEX analysis with the HVAC CAPEX interpolated between 80 - 120 km for some configurations. P is the installed active power of the wind farm.

C

Appendix 3

Figures C.1, C.2, and C.3 presents the LCOE analysis based on the interpolated CAPEX for HVAC for all studied power levels and distances of the three topologies. The blue line represents the LCOE of HVAC, the green line is LFAC, and the orange line represents HVDC.

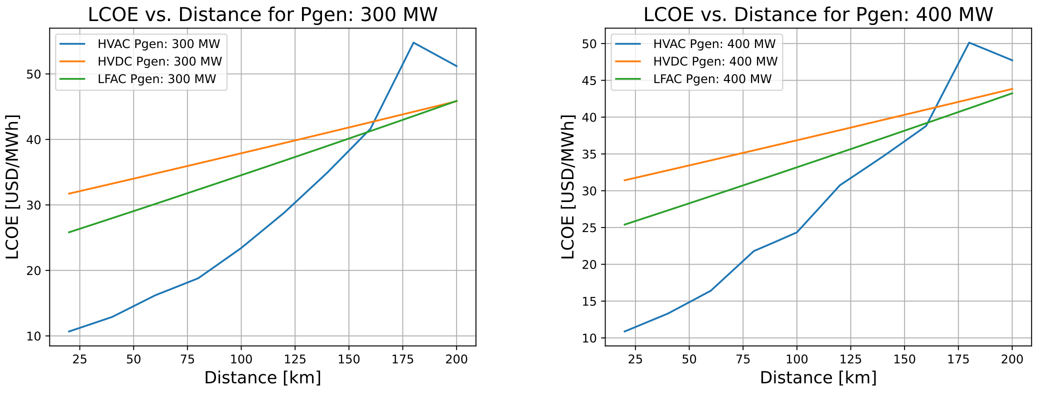

(a) P = 300 MW. *(b)* P = 400 MW.

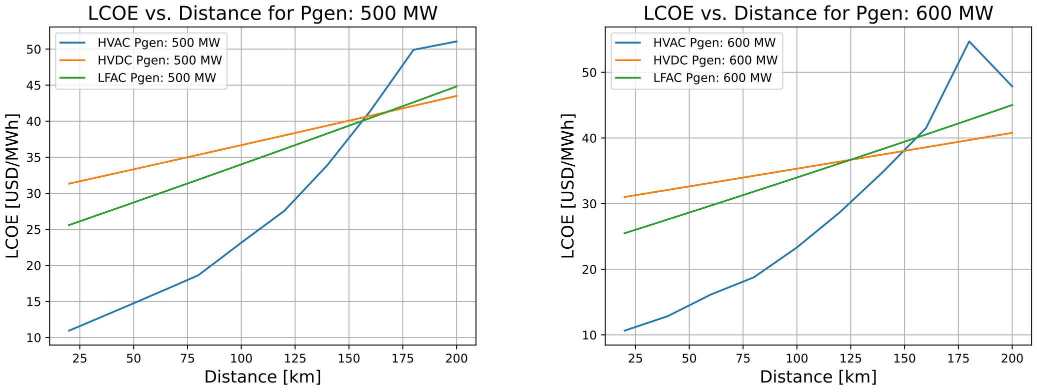

(c) P = 500 MW. *(d)* P = 600 MW.

Figure C.1: Plots presenting the LCOE analysis based on the interpolated HVAC cost. P is the installed active power of the wind farm.

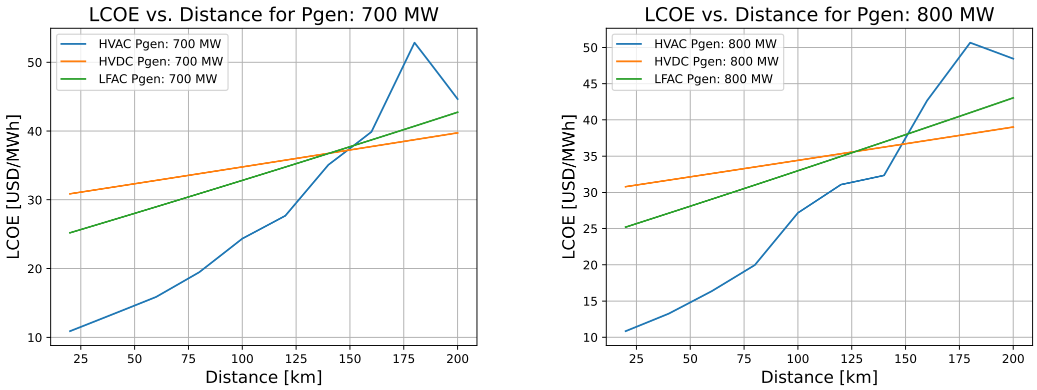

(a) P = 700 MW. ***(b)*** P = 800 MW.

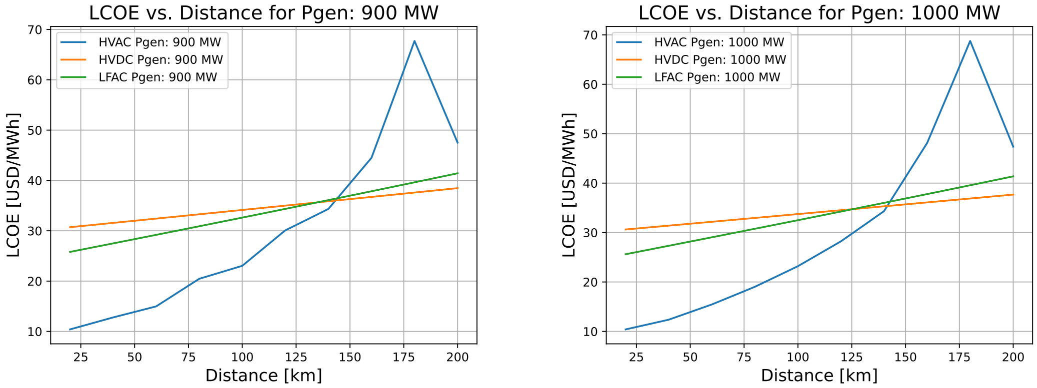

(c) P = 900 MW. ***(d)*** P = 1000 MW.

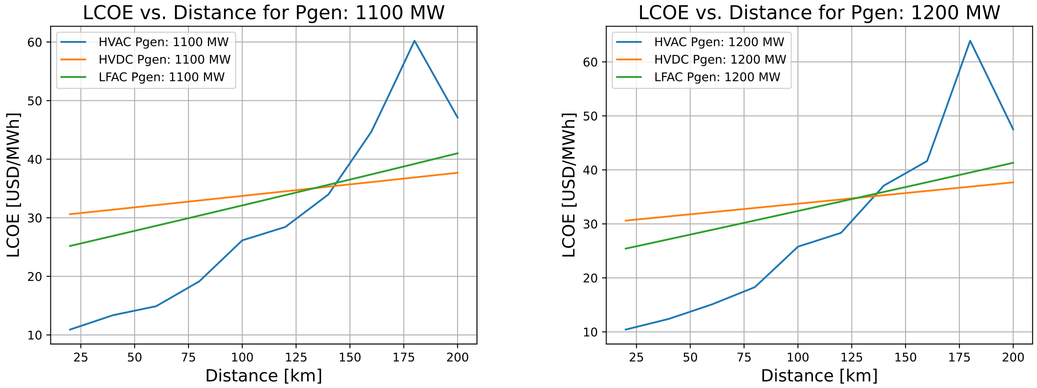

(e) P = 1100 MW. ***(f)*** P = 1200 MW.

Figure C.2: Plots presenting the LCOE analysis based on the interpolated HVAC cost. P is the installed active power of the wind farm.

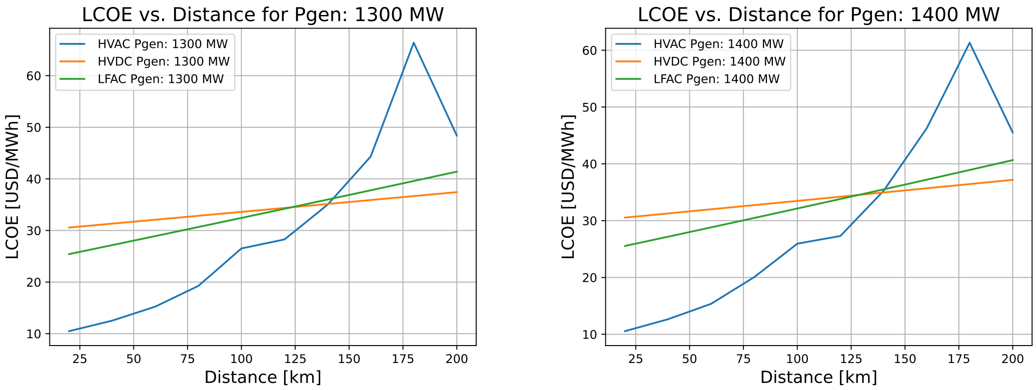

(a) P = 1300 MW.

(b) P = 1400 MW.

Figure C.3: Plots presenting the LCOE analysis based on the interpolated HVAC cost. P is the installed active power of the wind farm.

DEPARTMENT OF ELECTRICAL ENGINEERING
CHALMERS UNIVERSITY OF TECHNOLOGY
Gothenburg, Sweden
www.chalmers.se

CHALMERS
UNIVERSITY OF TECHNOLOGY